공학박사학위논문

Preparation of Functional Microporous Organic Polymers and Their Applications for Heterogeneous Catalysis and Dye Adsorption

기능성 마이크로기공성 유기고분자의 합성과 이의 불균질 촉매반응과 염료 흡착에의 활용

2017년 8월

서울대학교 대학원

재료공학부

김 종 길

Abstract

Preparation of functional microporous organic polymers and their applications for heterogeneous catalysis and dye adsorption

Jong Gil Kim

Department of Materials Science and Engineering

Seoul National University

Microporous organic polymers (MOPs) have many remarkable properties such as high surface area, low density, microporosity, and physicochemical stability. Various functional groups can be introduced to MOPs by the selection of reactants and post-modification, which facilitates practical uses of MOPs in various fields. However, most MOPs are obtained by insoluble powders because of their highly crosslinked structures, which causes poor processability of MOPs. In this study, various functional MOPs having shape-controlled structures were prepared and used for heterogeneous catalysis and dye adsorption.

Firstly, a MOP sponge was prepared using a homogenized electrospun

nanofiber as the reinforcement. The Sonogashira-Hagihara coupling reaction of 2,5-dibromoaniline and 1,3,5-triethynylbenzene in a dispersion of homogenized electrospun nanofibers (PVASi) produced the compressible MOP composite with a core-shell structure (PVASi@TEDB-NH_2). The polymer was uniformly grown on the surface of the nanofibers because TEDB-NH_2 had primary amino groups that could form hydrogen bonds with the hydroxyl groups on the surface of PVASi. PVASi@TEDB-NH_2 showed an average density and a BET surface area of 30.4 mg cm^{-3} and 447 m^2g^{-1}, respectively. The composite sponge was used for the removal of an organic dye dissolved in water. When PVASi@TEDB-NH_2 was manually compressed and released in an aqueous methylene blue (MB) solution, the dye adsorption occurred rapidly.

Secondly, a microporous catalytic membrane based on a hypercrosslinked polymer (HCP) was prepared. A HCP-based nanofibrous membrane was synthesized via Friedel-Crafts reaction of 1,1'-bi-2-naphthol in the presence of an aminated polyacrylonitrile (APAN) nanofibrous membrane as a substrate. The HCP was uniformly grown on the surface of the APAN nanofiber, which conferred a hierarchical porosity to the membrane. The HCP-based nanofibrous membrane showed a good mechanical strength and microporosity with a Brunaure-Emmett-Teller (BET) surface area of 375 m^2 g^{-1}. The HCP-based nanofibrous catalytic membrane (APAN-HCP-Pd) was prepared via the in-situ

growth of palladium nanoparticles inside the membrane. The application of APAN-HCP-Pd as a catalytic membrane was investigated for the reduction of 4-nitrophenol.

Thirdly, a compressible monolithic catalyst based on a MOP nanotube sponge was prepared. The monolithic MOP sponge was synthesized via Sonogashira-Hagihara coupling reaction between 1,4-diiodotetrafluorobenzene and 1,3,5-triethynylbenzene in a co-solvent of toluene and TEA (2:1, v/v) without stirring. The MOP sponge had an intriguing microstructure, where tubular polymer fibers having a diameter of hundreds of nanometers were entangled. It showed hierarchical porosity with a Brunauer-Emmett-Teller (BET) surface area of 512 m^2 g^{-1}. The MOP sponge was functionalized with sulfur groups by the thiol-yne reaction. The functionalized MOP sponge exhibited a higher BET surface area than the MOP sponge by 13 % due to the increase in the total pore and micropore volumes. A MOP sponge-Ag heterogeneous catalyst (S-MOPS-Ag) was prepared by in-situ growth of silver nanoparticles inside the sulfur-functionalized MOP sponge by the reduction of Ag^+ ions. The catalytic activity of S-MOPS-Ag was investigated for the reduction reaction of 4-nitrophenol in an aqueous condition. When S-MOPS-Ag was compressed and released during the reaction, the rate of the reaction was considerably increased. S-MOPS-Ag was easily removed from the reaction

mixture owing to its monolithic character and was reused after washing and drying.

Lastly, compressible polyimide composite having metal binding sites was prepared by in situ polymerization inside a melamine sponge. 1,3,5-Tris(4-aminophenyl)benzene and pyromellitic dianhydride were used as a triamine and a dianhydride monomer, respectively, to construct the microporous framework, and 5-amino-1,10-phenanthroline was used as a functional monomer. The microporous polyimide containing phenanthroline groups (MPI-Phen) was obtained as insoluble powders. However, when the polymerization was carried out in the melamine sponge, MPI-Phen formed a coating layer on the sponge skeletons. The melamine sponge/microporous polyimide composite (MS/MPI-Phen) had an open cellular structure with a hierarchical porosity composed of macropores between the sponge skeletons and meso- and micropores of the MPI-Phen coating. It showed the higher compressive strength than the melamine sponge, indicating the reinforcement by the microporous polymer. The BET surface areas of MPI-Phen and MS/MPI-Phen were 723 m^2g^{-1} and 524 m^2g^{-1}, respectively. Pd(II) ions were coordinated with the phenanthroline groups of MS/MPI-Phen for heterogeneous catalysis (MS/MPI-Phen-Pd). The catalytic activity of MS/MPI-Phen-Pd was evaluated for the Suzuki coupling reaction between bromobenzene and phenylboronic acid.

Keywords: microporous polymer, electrospinning, sponge, membrane, heterogeneous catalysis, dye adsorption.

Student Number: 2011-20631

Contents

List of Schemes

List of Tables

List of Figures

Figure II-3. Photographs of (a) pieces of a PVASi mat in toluene and (b) a dispersion of homogenized PVASi in toluene. (c) SEM image of individual homogenized PVASi nanofibers at low magnification.

Figure II-4. (a), (b) SEM and (c), (d) TEM images of PVASi@TEDB-NH_2. (e) The diameter distribution of PVASi@TEDB-NH_2 nanofibers.

Figure II-5. (a) EDS elemental analysis and (b) mapping of nitrogen for PVASi@TEDB-NH_2.

Figure II-6. (a) SEM and (b) TEM images of PVASi@TEDB.

Figure II-7. (a) Images of PVASi@TEDB-NH_2 under loaded and unloaded conditions (strain = 40%). (b) Compressive stress-strain curves (maximum stress = 20, 40 and 60%) and (c) 10 cycles of loading-unloading test results of PVASi@TEDB-NH_2 (maximum strain = 40%).

Figure II-8. (a) Solid state ^{13}C CP/MAS NMR spectra, (b) FT-IR spectra, and (c) PXRD patterns of TEDB-NH_2 and PVASi@TEDB-NH_2. (d) TGA thermograms of PVASi, TEDB-NH_2, and PVASi@TEDB-NH_2.

Figure II-9. (a) N_2 adsorption-desorption isotherms measured at 77 K and (b) NLDFT pore size distributions of PVASi@TEDB-NH_2 and TEDB-NH_2.

Figure II-10. CO_2 uptakes at 273 K of PVASi@TEDB-NH_2 and TEDB-NH_2.

Figure II-11. UV–vis spectra of the aqueous MB solution (initial concentration = 5 x 10^{-5} M) measured after removing the dye by (a) compression and release

sulfur for S-MOPS.

Figure IV-5. (a) Compressive stress-strain curves (maximum strain = 20 and 40 %) and (b) 10 cycles of the loading-unloading test results of S-MOPS (maximum strain = 40 %). (c) Comparison of hysteresis curves of the MOP sponge and S-MOPS at 40 %.

Figure IV-6. (a) FT-IR spectra, (b) Solid state ^{13}C CP/MAS NMR spectra, (c) PXRD patterns and (d) TGA thermograms of the MOP sponge and S-MOPS.

Figure IV-7. (a) N_2 adsorption-desorption isotherms measured at 77 K and (b) NLDFT pore size distributions of the MOP sponge and S-MOPS.

Figure IV-8. (a) SEM image and the photograph (inset) of S-MOPS-Ag. (b) TEM image and (c) EDS mapping of silver atoms for S-MOPS-Ag. (d) Diameter distribution of Ag nanoparticles inside S-MOPS-Ag.

Figure IV-9. (a) PXRD pattern of S-MOPS-Ag. (b) High-resolution XPS spectrum of Ag3d region of S-MOPS-Ag.

Figure IV-10. (a) Compressive stress-strain curves (maximum strain = 40%) and (b) N_2 adsorption-desorption isotherms measured at 77 K of S-MOPS and S-MOPS-Ag.

Figure IV-11. (a) UV-Vis spectra of the aqueous 4-NP solution (initial concentration = 1×10^{-4} M) measured during the reaction with the compression and release process. (b) Photographs of the 4-NP solution taken before and after

160 cycles of compression and release. UV-Vis spectra of the aqueous 4-NP solution (initial concentration = 1 x 10^{-4} M) measured without the compression and release process; (c) the reaction solution was not stirred and (d) the reaction solution was stirred.

Figure IV-12. UV-Vis spectra of the aqueous 4-NP solution (initial concentration = 1 x 10^{-4} M) measured during the reaction with the repeated compression and release of S-MOPS.

Figure IV-13. Plots of - $\ln(C_t / C_0)$ versus time during the catalytic reduction of 4-NP by S-MOPS-Ag under different reaction conditions. With the compression-release process, the apparent rates constant (k) for the reaction = 7.61 x 10^{-3} s^{-1}. Without the compression and release process, k = 2.84 x 10^{-4} s^{-1} when the reaction solution was not stirred and k = 6.64 x 10^{-4} s^{-1} when the reaction solution was stirred.

Figure IV-14. Change in the catalytic activity of S-MOPS-Ag during recycling.

Figure V-1. (a) FT-IR spectra, (b) Solid state ^{13}C CP/MAS NMR spectra and (c) PXRD pattern of MPI-Phen. (d) High-resolution XPS spectra of N 1s from MPI-Phen.

Figure V-2. N_2 adsorption-desorption isotherms of MPI-Phen.

Figure V-3. (a) Images of the melamine sponge (left) and MS/MPI-Phen (right). (b) Cross-sections of MS/MPI-Phen.

Chapter I.

Introduction

I-1. Microporous Organic Polymers (MOPs)

I-1-1. Introduction to MOPs

Porous materials are substances containing inner pores. According to the IUPAC classification, pores are identified by their size.[1] Macropores are pores with diameters exceeding 50 nm, mesopores have diameters between 2 and 50 nm, and micropores have diameters of less than 2 nm. Among these, the presence of micropores inside materials is known to contribute to a high internal surface area and to allow the adsorption of minute materials.[2,3] This feature can be used in applications such as gas storage and separation, the adsorption of small molecules, catalysis, and sensors. [2,4,5]

Generally, the adsorption of gases such as nitrogen, argon and carbon dioxide at a specific temperature is used to measure the porosity of porous materials.[6] At a low gas pressure, gas molecules initially fill the inside of the micropores. Subsequently, when the pressure increases, multilayer adsorption and capillary condensation of the gas molecules occurs at the mesopores and macropores.[1,7,8] Surface areas measured by the adsorption of gasses are commonly calculated by a Brunauer-Emmitt-Teller (BET) analysis, which is based on the monolayer capacity of porous materials.[1]

Various types of materials containing micropores have been explored such as carbon materials,[9,10] zeolites,[11] metal-organic frameworks (MOFs),[12,13] and microporous organic polymers (MOPs) for specific applications. Specifically, MOPs have attracted considerable attention due to their remarkable properties. In general, MOPs are synthesized through the covalent crosslinking between selected building blocks. They have highly interconnected three-dimensional (3D) rigid networks, which imparts a high surface area, microporosity, and chemical and thermal stability to the polymers.[2,5,14] Various types of chemical reactions and building blocks can be used to construct porous polymer networks, increasing the flexibility of structural designs and allowing the realization of desirable pore properties. Moreover, MOPs are easily functionalized by the choice of building blocks and by post-modifications.[5,15] To fabricate MOPs with desired properties, various chemical reactions have been researched.

I-1-2. Preparation Methods of MOPs

MOPs can be prepared using various chemical reactions including metal-catalyzed reactions and condensation reactions.

Metal-catalyzed coupling reactions are widely used to prepare hyper-crosslinked polymers with conjugated structures.[2,5] Since Cooper's group synthesized the first conjugated microporous polymers (CMPs) in 2007, various types of coupling reactions have been used to fabricate MOPs with controlled molecular structures.

The Sonogashira-Hagihara reaction is a typical coupling reaction for the synthesis of MOPs. Figure I-1 shows several MOPs synthesized by the Sonogashira-Hagihara reaction.[16,17]

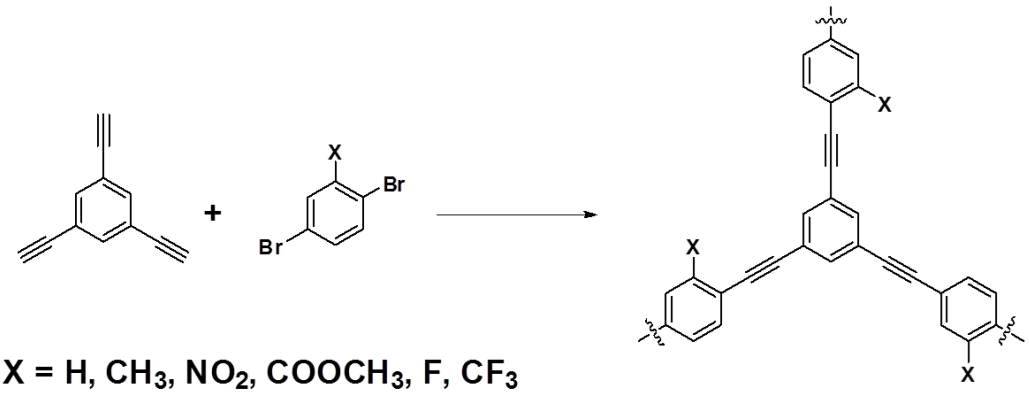

Figure I-1. Examples of MOPs prepared by the Sonogashira-Hagihara reaction.

The Yamamoto coupling reaction is another coupling reaction that has been used for the synthesis of MOPs with a high surface area. Zhou's group prepared tetrahedral monomers-based MOPs using the Yamamoto coupling reaction

(Figure I-2).[18] The polymer showed a very high BET surface area above 5000 m^2g^{-1} and had strong CO_2, H_2 and CH_4 uptake properties.

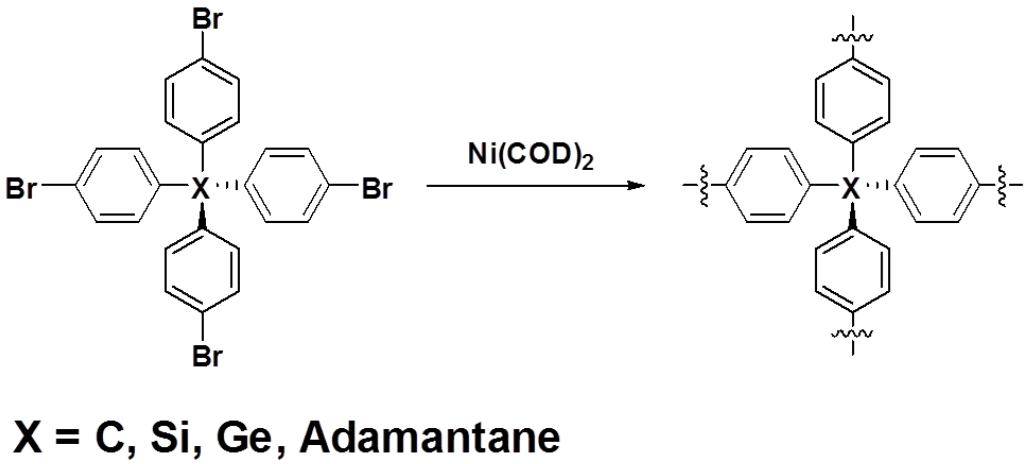

Figure I-2. Examples of MOPs prepared by the Yamamoto coupling reaction.

Jiang's group prepared a polyphenylene-based MOP (MOP-1) by the Suzuki coupling reaction (Figure I-3).[19] Owing to its conjugated structure and high surface area, MOP-1 showed rapid and efficient light energy flow properties.

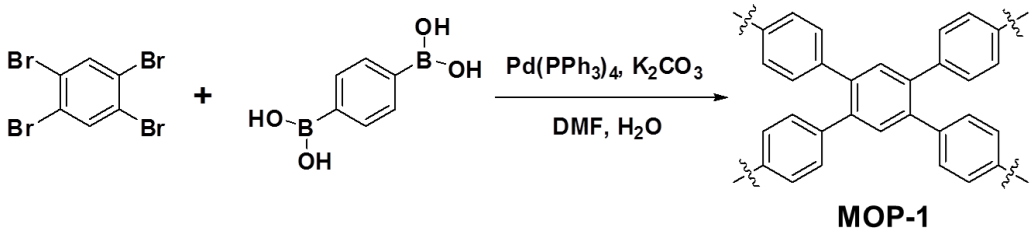

Figure I-3. Synthesis of MOP-1 by the Suzuki coupling reaction.

Several groups synthesized MOPs by an oxidative coupling reaction. Given that the oxidative coupling reaction requires relatively inexpensive catalysts such as $FeCl_3$, it is a cost-effective reaction compared to other coupling reactions which require novel metal catalysts such as palladium. Han's group reported various types of MOPs using the oxidative coupling reaction.[20,21] A carbazole-based MOP (MOP-2) showed a high BET surface area above 2000 m^2g^{-1} and high gas selectivity toward CO_2 over N_2 (Figure I-4).

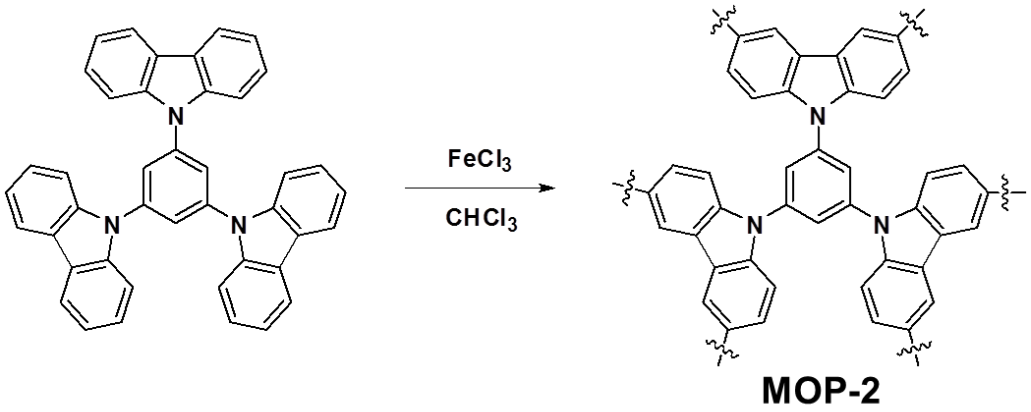

Figure I-4. Synthesis of MOP-2 by the oxidative coupling reaction

MOP-3 was synthesized by azide-alkyne cycloaddition, also known as a "Click reaction" (Figure I-5).[22] Click chemistry is suitable for the preparation of nitrogen-rich MOPs due to the presence of triazole units.

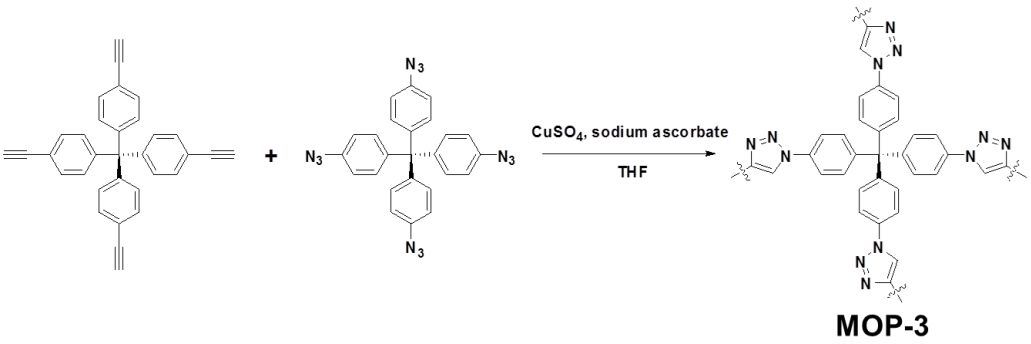

Figure I-5. Synthesis of MOP-3 by azide-alkyne cycloaddition.

The Friedel-Crafts reaction is an efficient way to fabricate hypercrosslinked microporous polymers. Diverse types of aromatic group-containing monomers and polymers can be used for the Friedel-Crafts reaction (Figure I-6).[14,23]

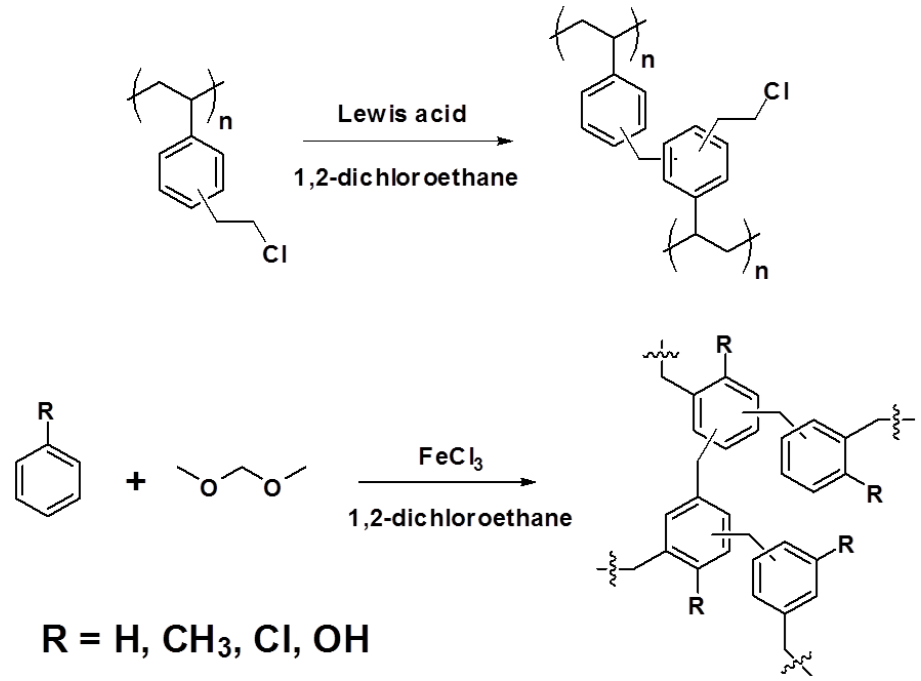

Figure I-6. Examples of MOPs prepared by the Friedel-Crafts reaction.

Condensation reactions have been also widely used to synthesize microporous polymers. Unlike metal-catalyzed reactions, most condensation reactions are conducted without a metallic catalyst, providing cost and environment advantages.

Imide condensation is a representative reaction which can be used to prepare thermosetting resins. Microporous polyimides have attracted much research interest because of their rigid heteroaromatic frameworks and high thermal and chemical stability levels. Moreover, they have numerous nitrogen and oxygen atoms, making them beneficial for many applications, such as CO_2 adsorption and metal ion capturing.[24,25] Figure I-7 shows an example of microporous polyimide (MOP-4), which exhibited a BET surface area of 1454 m^2g^{-1}.[24]

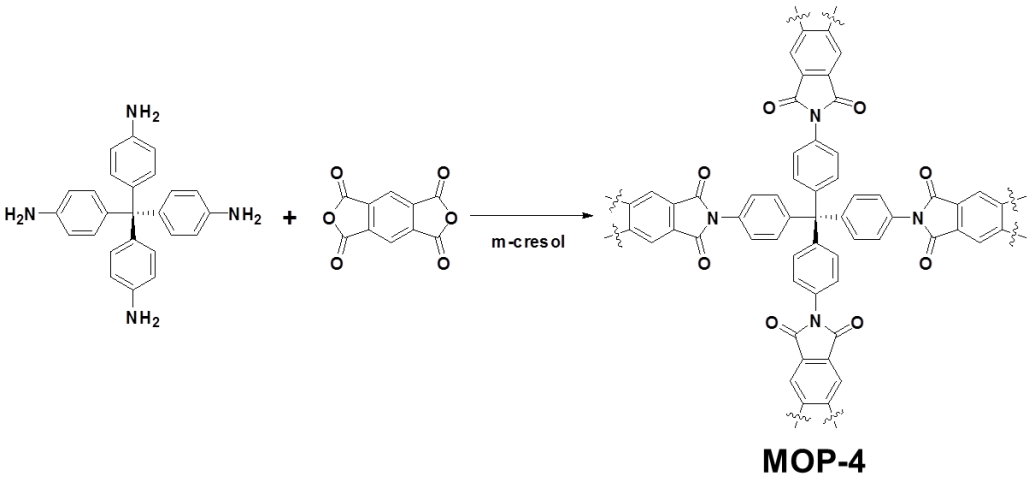

Figure I-7. Synthesis of MOP-4 by the imide condensation reaction.

Imine condensation between aldehyde and amine groups is also used to create rigid microporous networks without a catalyst. Several groups have

investigated imine-linked MOPs (Figure I-8a).[26,27] MOP-5 showed good CO_2 capture capacity because of the presence of many nitrogen atoms. Müllen's group prepared a melamine-based MOP (MOP-6) via Schiff-base chemistry (Figure I-8b).[28] MOP-6 showed a BET surface area of 1377 m^2g^{-1}. MOPs based on benzimidazole were synthesized using aldehyde and ortho-diamine monomers. El-Kaderi's group reported MOP-7, which had a BET surface area of 1172 m^2g^{-1} (Figure I-8c).[29]

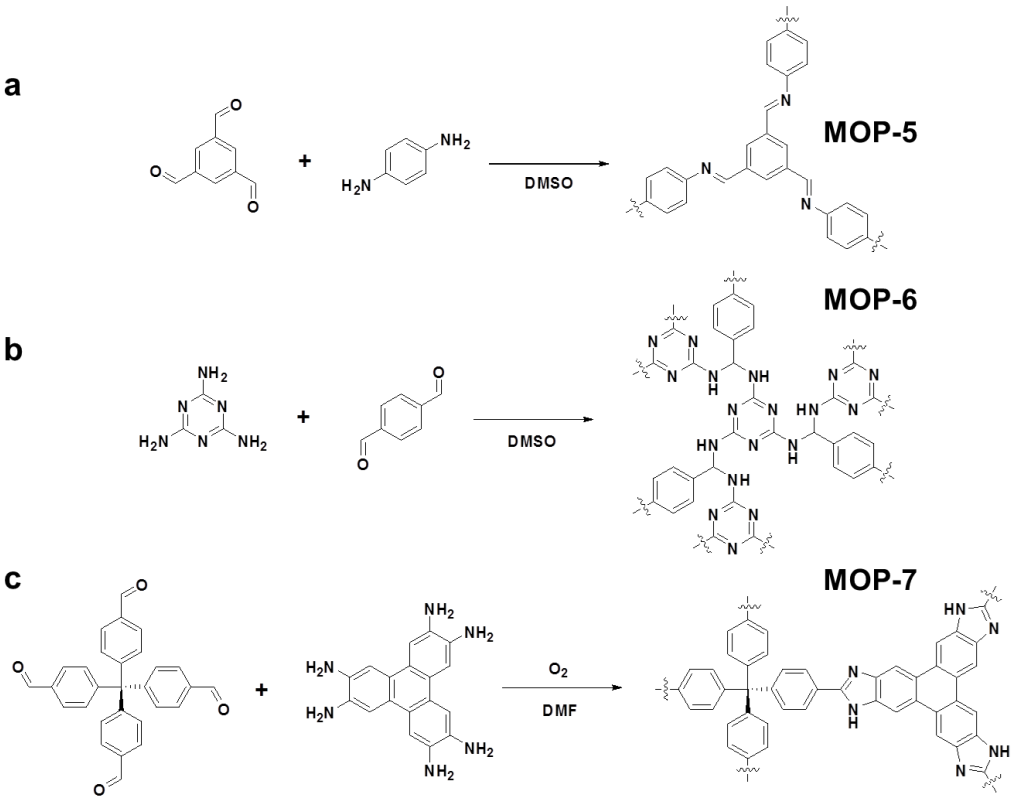

Figure I-8. Synthesis of (a) MOP-5, (b) MOP-6, and (c) MOP-7.

Kanatzidis's group synthesized MOP aerogels using various types of phenolic molecules and aldehydes (Figure I-9).[30] The BET surface area of MOP-8 was nearly 1230 m^2g^{-1}. Due to their abundant hydroxyl functional groups, phenolic-resin based MOPs showed strong potential for CO_2 uptake and metal ion chelating applications.[30,31]

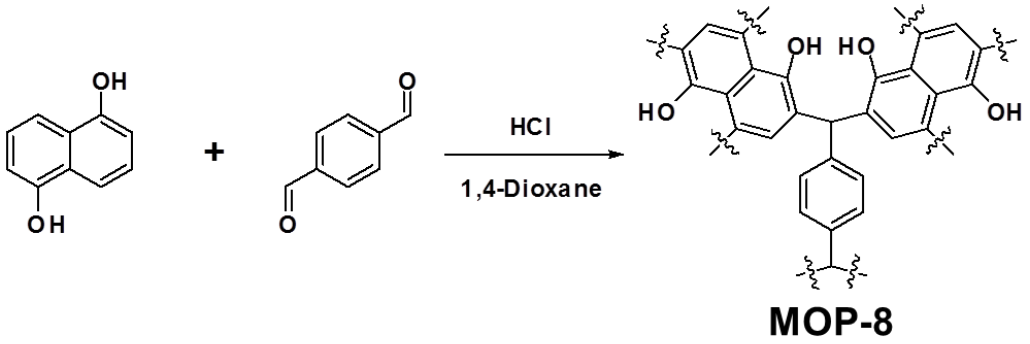

Figure I-9. Synthesis of MOP-8.

MOP-9 was synthesized by the thiol-yne reaction with an aid of a thermal initiator (Figure I-10a).[32] MOP-9 showed a BET surface area of 576 m^2g^{-1} and could support gold nanoparticles for catalysis.

A catalyst-free pericyclic reaction such as Diels-Alder reaction has been used to synthesize reversibly-crosslinked porous polymers (Figure I-10b).[33] MOP-10 was structurally reconstructed by heating and showed a BET surface area of 1038 m^2g^{-1}.

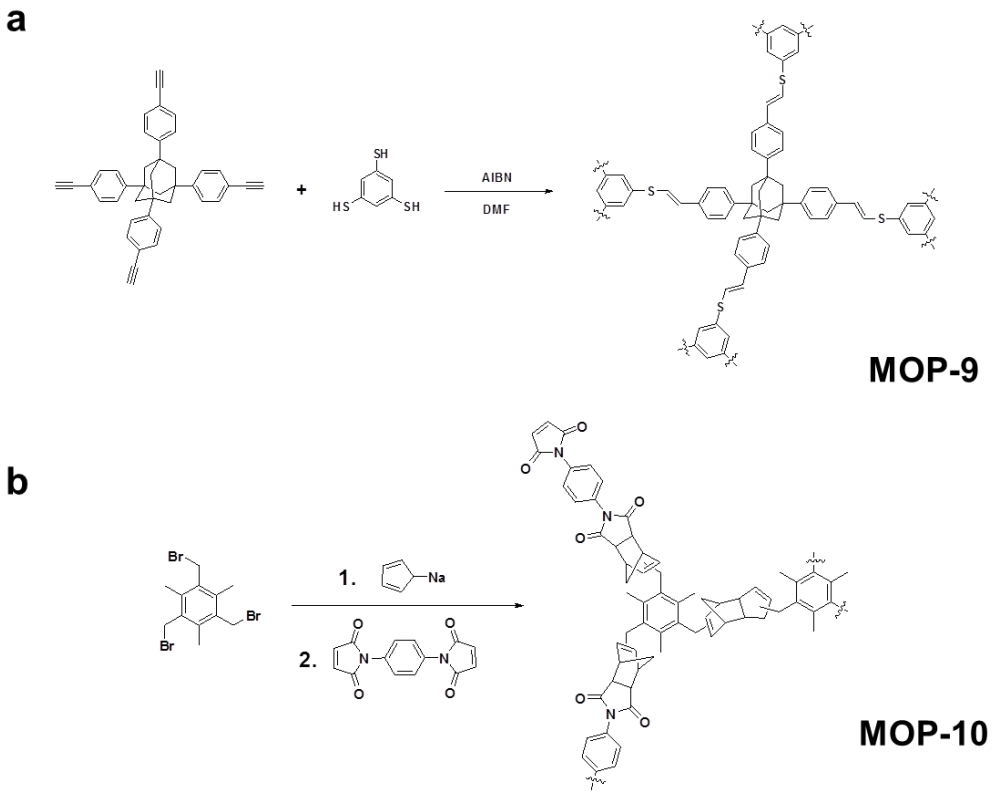

Figure I-10. Synthesis of (a) MOP-9 and (b) MOP-10.

I-1-3. Potential Applications of MOPs

MOPs can be used practically in various applications. The adsorption and separation of specific gases are typical applications. Recently, carbon dioxide (CO_2) has been pointed out as the major cause of the greenhouse effect. Most CO_2 is produced by the combustion of fossil fuels, such as by power plants and automobiles.[34] Therefore, CO_2 capture and storage from post-combustion

gases are significant challenges. In general, the post-combustion gas produced by a power plant is composed of nitrogen (N_2) (> 70%) and CO_2 (10-15 %).[35] Meanwhile, methane (CH_4) is another abundant alternative energy source. It has environmental advantages compared to other fossil fuels due to its the high ratio of hydrogen to carbon. However, natural gas contains impurities such as CO_2, N_2, and other hydrocarbons and an additional purification process is required.[35,36] For these reasons, materials for the CO_2 capture must have not only high CO_2 adsorption capacities but also good selectivity for CO_2 over other gases such as N_2 and CH_4.

Because a CO_2 molecule has a large quadrupole moment,[37] polar groups in MOPs can improve the degree of affinity for CO_2 molecules. The definite interaction between CO_2 and functional groups has been calculated according to density function theory.[38] A benzene groupshows a binding energy of only -5.57 kJ mol^{-1} with CO_2. However, the binding energy of benzene with CO_2 increases significantly by the functionalization with a polar group. For example, the binding energy between benzene with an amine group and CO_2 is -13.34 kJ mol^{-1}. MOPs have good potential as a physical adsorbent for CO_2 capture and storage due to their high degree of porosity and the possibility of surface functionalization.[5]

Figure I-11 shows examples of MOPs with high CO_2 storage and separation properties. MOP-11 with a nitrogen-rich structure was synthesized by the imine condensation reaction.[39] It showed a high BET surface area (1740 $m^2 g^{-1}$), high CO_2 uptake level (26.7 wt%, 273 K, 1 bar) and moderate selectivity for CO_2/N_2 (14.5) and CO_2/CH_4 (11.0) adsorption.

MOP-12 was synthesized by post-functionalization to improve CO_2 uptake and selectivity.[40] After amine modification, the surface area of this MOP decreased from 1249 $m^2 g^{-1}$to 554 $m^2 g^{-1}$. However, the CO_2 uptake of the MOP increased from 11.0 wt% to 12.8 wt%. Specifically, the selectivity values for CO_2/N_2 and CO_2/CH_4 were greatly increased, from 12 to 38 and from 3 to 9, respectively.

MOP-13 was synthesized by a Friedel-Crafts reaction between cyanuric chloride and ferrocene.[41] MOP-13 had a BET surface area of 875 $m^2 g^{-1}$ and showed good CO_2 uptake and CO_2/N_2 selectivity of 16.9 wt% (273 K, 1 bar) and 107, respectively. The nitrogen-rich MOP skeleton and Fe ions inside the framework contributed to the high CO_2 adsorption.

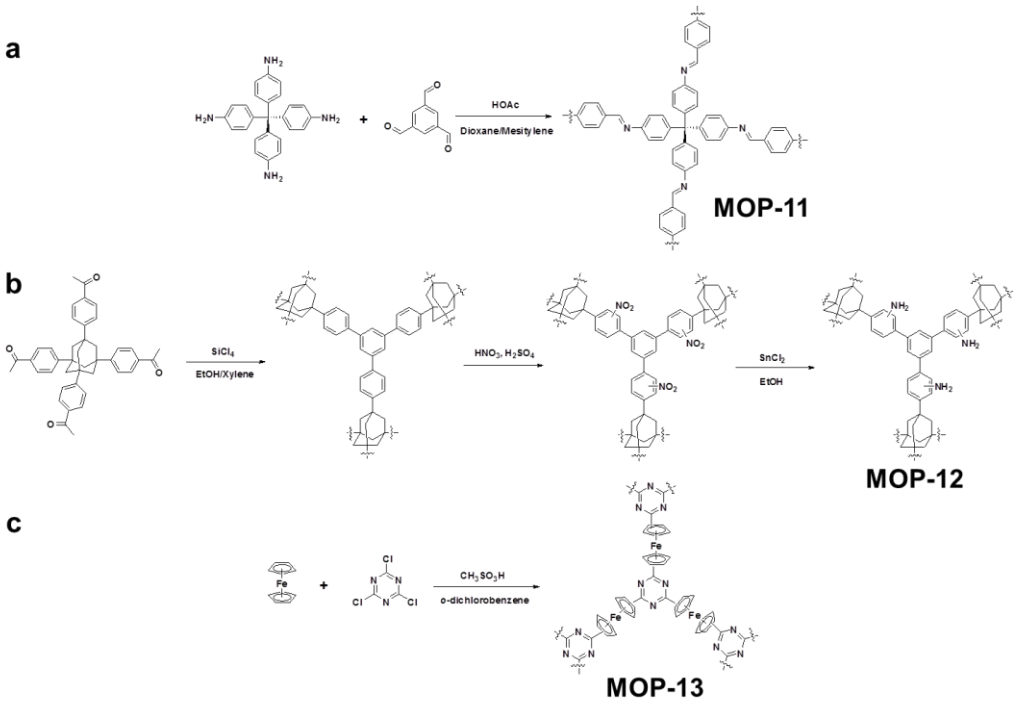

Figure I-11. Synthesis of (a) MOP-11, (b) MOP-12, and (c) MOP-13 for CO_2 adsorption.

MOPs can be used for the adsorption of harmful volatile compounds. Li's group synthesized a thiophene-containing MOP (MOP-14) for the adsorption of volatile iodine (Figure I-12).[42] Owing to its high porosity and electron-rich thiophene groups, MOP-14 showed iodine uptake of 222 wt% within 3 hours.

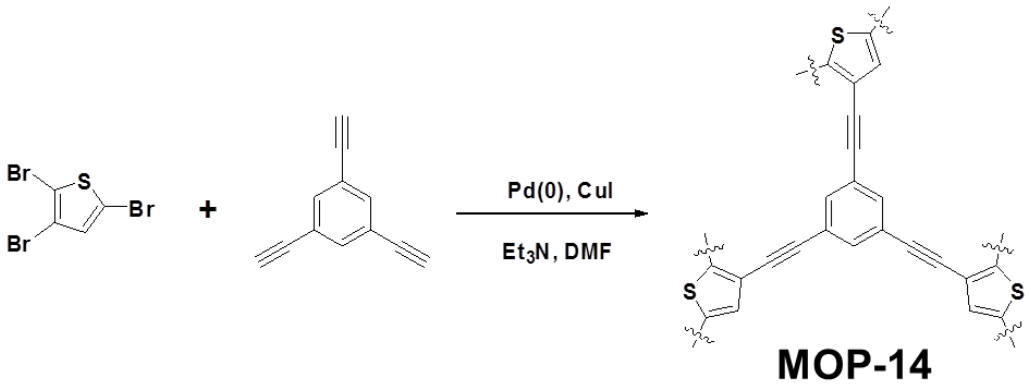

Figure I-12. Synthesis of MOP-14 for iodine adsorption.

Deng's group reported MOP-15, which had outstanding adsorption properties for organic dyes and metal ions (Figure I-13).[43] The maximum adsorption capacities of Congo red dye, methyl blue dye, and Pb^{2+} ions were 1376.7 mg g^{-1}, 629.1 mg g^{-1} and 826.1 mg g^{-1}, respectively.

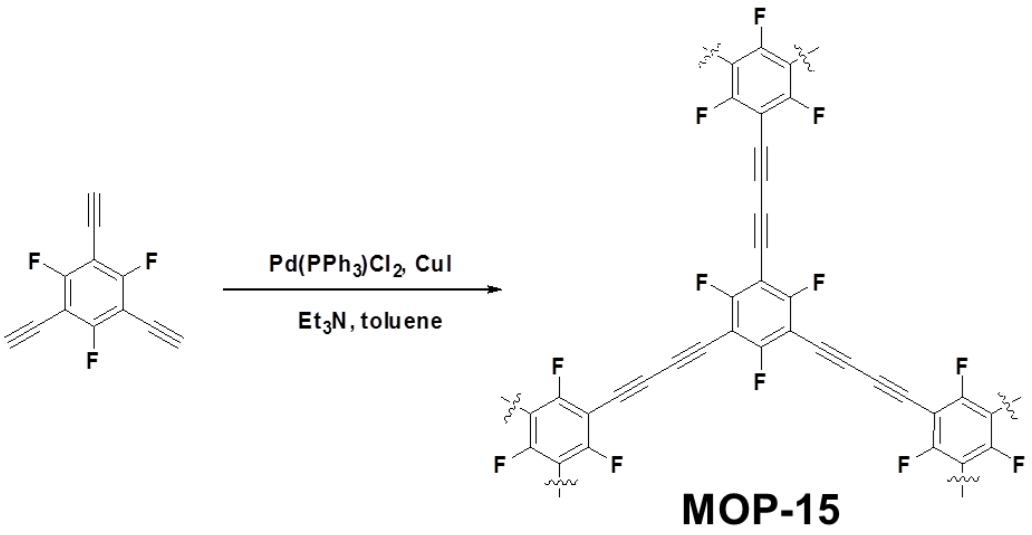

Figure I-13. Synthesis of MOP-15.

Several conjugated MOPs have recieved attention for energy applications. For example, an aza-fused CMP (MOP-16) was synthesized for supercapacitive energy storage (Figure I-14).[44] Because of its well-defined conjugated microporous structure, MOP-16 showed remarkable capacitance and energy density levels as well as good recyclability. Jiang's group prepared a hexaazatrinaphthalene CMP (HATN-CMP) for lithium-battery energy applications.[45] It had redox-active units and open nanopores, showing high energy capacity and good cycle stability.

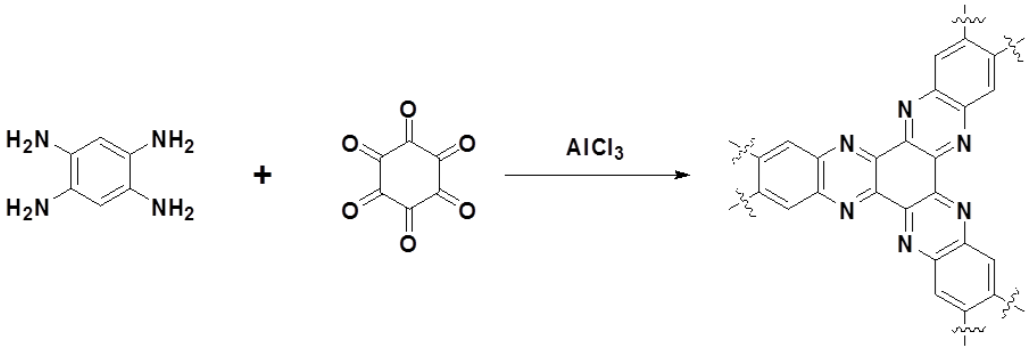

Figure I-14. Synthesis of MOP-16.

Fluorescent conjugated MOPs have the potential for use in small molecular sensing applications. For example, Liu's group synthesized an azine-linked MOP (MOP-17) by means of solvothermal condensation (Figure I-15b).[46] MOP-17 showed moderate microporosity (570 m^2g^{-1}) and high luminescence efficiency. Owing to the abundant hydroxyl groups on the pore wall, it efficiently adsorbed Cu^{2+} ions, leading to the fluorescence quenching.

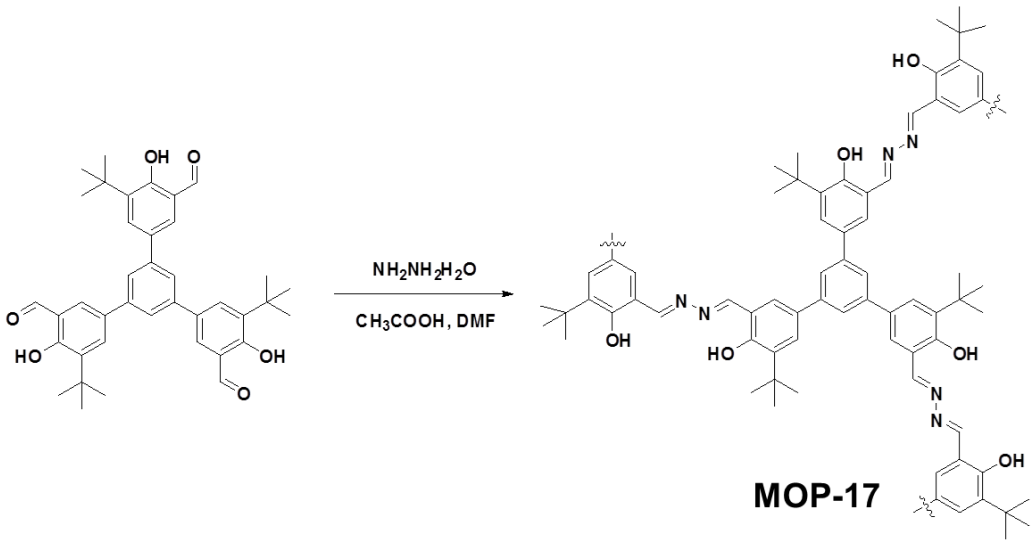

Figure I-15. Synthesis of MOP-17.

I-2. Heterogeneous Catalysis with MOPs

I-2-1. Introduction to Heterogeneous Catalysis

Heterogeneous catalysts have attracted considerable attention from the chemical industry. In general, heterogeneous catalysts are composed of an active phase and an insoluble support where active sites are dispersed (Figure I-16).[47,48] Compared to homogeneous catalysts, heterogeneous catalysts have some advantages. They can be removed by simple methods such as filtration

and centrifugation from reaction mediums, which increases the efficiency of the process and reduces the additional cost.[47,48] Heterogeneous catalysts can be used for continuous flow processes, thus expanding the applications of catalysts.[48] Moreover, some heterogeneous catalysts show catalytic properties superior to those of homogeneous catalysts due to the site-isolation and constraint effects.[49]

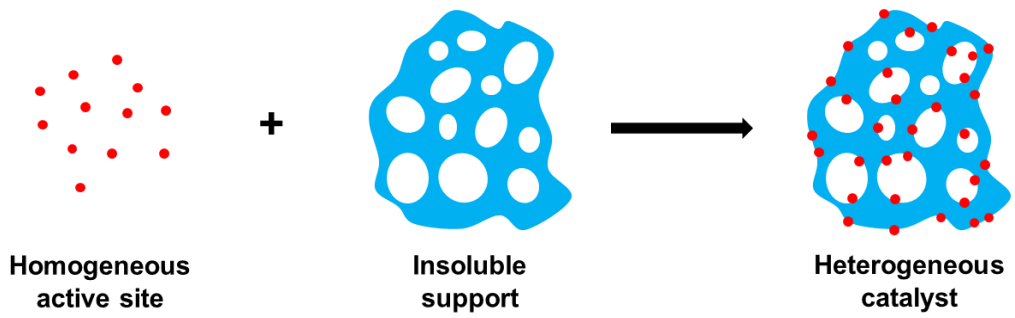

Figure I-16. Illustration of structure of a heterogeneous catalyst.

Choice of support materials for heterogeneous catalysts is important to optimize their catalytic properties. First, support materials should be stable during reaction processes. Secondly, active sites should be uniformly dispersed on the surfaces of the supports to maximize the catalytic efficiency.[50,51] Finally,

supports should immobilize active species tightly to prevent them leaching during reactions.[9,47,49]

I-2-2. Porous Materials for Heterogeneous Catalysis

Porous materials are a prime candidate as a support for heterogeneous catalysts. They have large surface areas and high porosity, which facilitates the easy diffusion of reactants to active sites.[49,50] Therefore, various types of porous materials have been researched for heterogeneous catalysis.

Zeolites are crystalline microporous inorganic materials. Zeolites are composed of aluminosilicates, and are used for oil refining and petrochemistry.[52] Some metal cations can be incorporated into zeolites by ion-exchange processes, which can act as catalytic active species.[11,52] Zeolites containing metal cations have been used as heterogeneous catalysts for the catalytic oxidation of volatile organic compounds.[11]

Porous carbons have been used as substrates for heterogeneous catalysts due to their high surface area, controllable morphologies, and good chemical stability.[9] In general, metal nanoparticles are dispersed inside porous carbons as active species. By doping heteroatoms into the surface of porous carbons, the catalytic properties and the stability of heterogeneous catalysts can be

improved.[9] Porous carbons can be also used for electrochemical catalysis due to their high electrical conductivity.[9,53]

Mesoporous silicas are prepared by a sol-gel reaction in the presence of a micelle. Mesoporous silicas have many advantages for heterogeneous catalysts, such as large surface areas, tunable pore sizes, high thermal stability levels, and a low price.[47,50] Moreover, their pore surface can be modified by co-condensation and post-grafting methods.[47] Various active species including organic groups, metal ions, and metal nanoparticles can be immobilized onto mesoporous silicas.[47,50]

I-2-3. Heterogeneous Catalysis with MOPs

Compared to carbon and inorganic materials, MOPs have many advantages when used as a support for heterogeneous catalysis, such as high porosity levels, robust molecular structures, good structural stability and functionalization capabilities.[5,51,54] Diverse types of active species have been immobilized in MOPs by numerous methods.

MOP-metal ion complexes are composed of microporous polymers with functional groups and catalytic metal ions. Metal ions are homogeneously coordinated with the functional groups of the polymers. Jiang’s group

synthesized a metalloporphyrin-based MOP (MOP-18) by the Suzuki coupling reaction (Figure I-17).[55] MOP-18 showed good selectivity for the oxidative reaction of sulfides to sulfoxides.

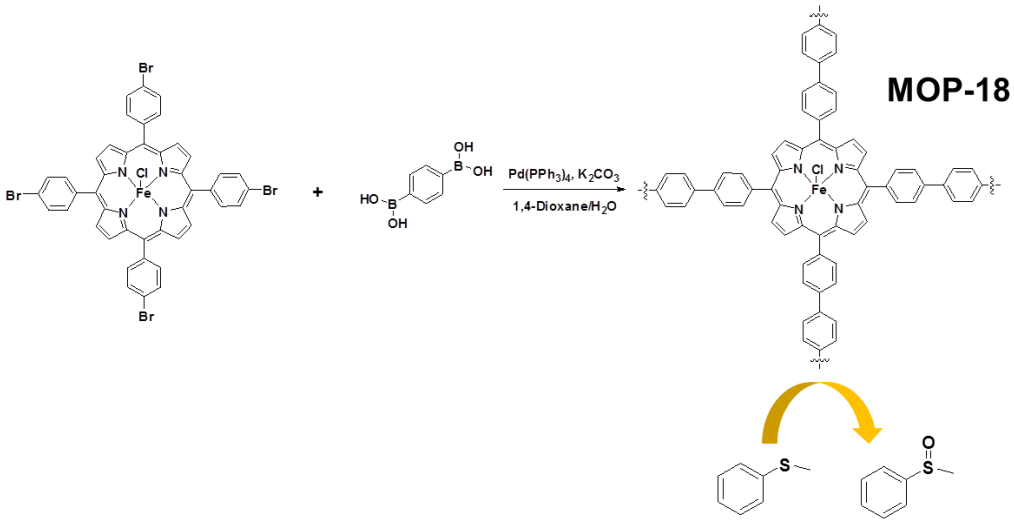

Figure I-17. Synthesis of MOP-18 and the catalytic reaction of sulfides to sulfoxides.

MOP-metal nanoparticle complexes are also used as heterogeneous catalysts. For example, Schüth's group reported a polyphenylene-Pd MOP catalyst.[56] Microporous polyphenylene was synthesized by a Pd ion-catalyzed coupling reaction. Subsequently, the MOP was thermally-treated to reduce the Pd ions to Pd nanocrystals. Zhang's group used a catechol-based MOP (MOP-

19) as a substrate for immobilizing Pd nanoparticles (Figure I-18).[31] Pd ions were captured by hydroxyl groups inside the polymer and reduced by $NaBH_4$. MOP-19 exhibited good catalytic ability for the reduction of 4-nitrophenol in an aqueous condition.

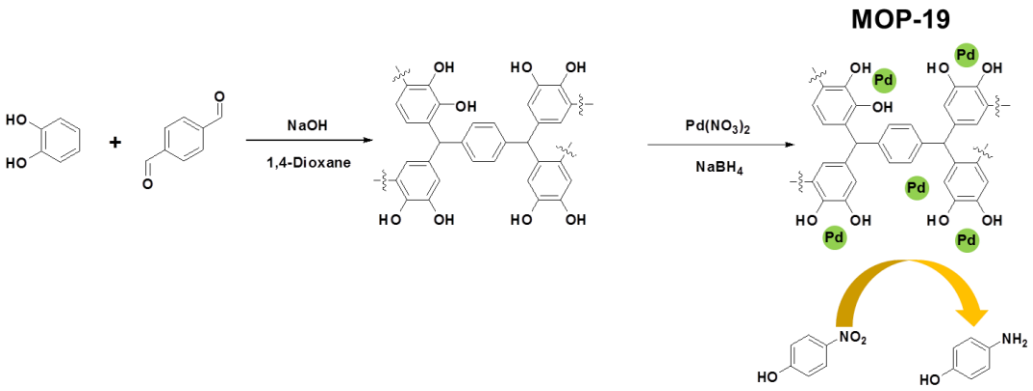

Figure I-18. Synthesis of MOP-19 and the catalytic reaction of 4-nitrophenol reduction.

Organocatalysts can be introduced into MOPs. Wang's group reported a 4-(N,N-dimethylamino)-pyridine-containing MOP (MOP-20) (Figure I-19).[57] MOP-20 showed good catalytic ability for the acylation of alcohols.

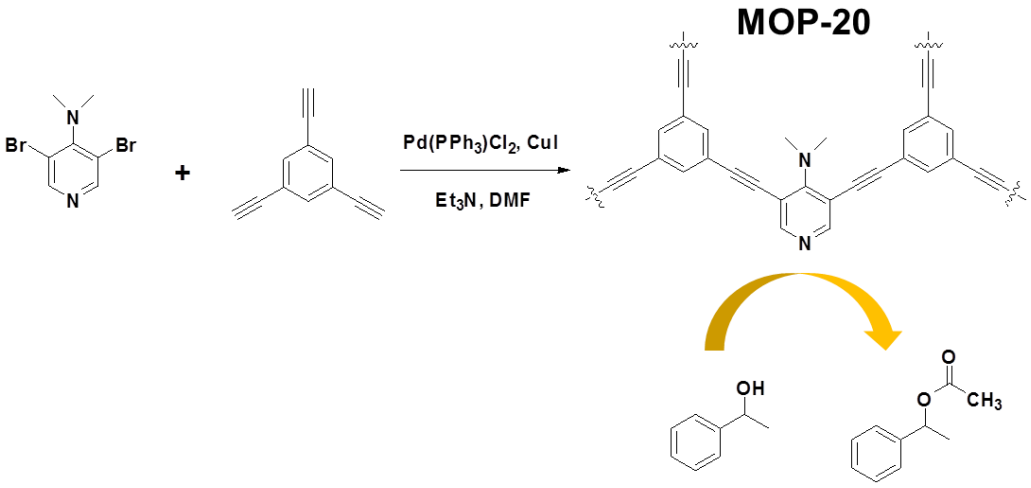

Figure I-19. Synthesis of MOP-20 and the catalytic reaction of the acylation of alcohols.

I-3. Shape Control of MOPs

Despite their superior properties and numerous potential applications, practical uses of MOPs have been limited by their poor processability.[58,59] In general, MOPs are synthesized by crosslinking reactions and are obtained in an amorphous powder form. Because they are insoluble, most MOPs are difficult to process into desired shapes. Several studies have been performed in an effort to overcome this problem.

I-3-1. MOPs with Controlled Nanostructures

MOPs with controlled nanostructures have been fabricated by several research groups. For example, Wang's group reported a hollow MOP capsule using poly (methacrylic acid) nanoparticles as sacrificial templates.[60] The nanocapsule showed near-infrared absorption property and could be used for the thermal ablation of HeLa cells. Son's group prepared an isocoumarin-containing CMP nanocapsule (MOP-21) by a one-step Sonogashira-Hagihara reaction with the etching of silica nanoparticles (Figure I-20).[61] MOP-21 could absorb visible light. Meanwhile, Feng's group synthesized CMP-nanocarbon composites using a functionalized carbon nanosphere, a carbon nanotube, reduced graphene oxide as a template.[62] They showed good photoluminescence properties via an energy transfer between CMP as a donor and nanocarbon as an acceptor.

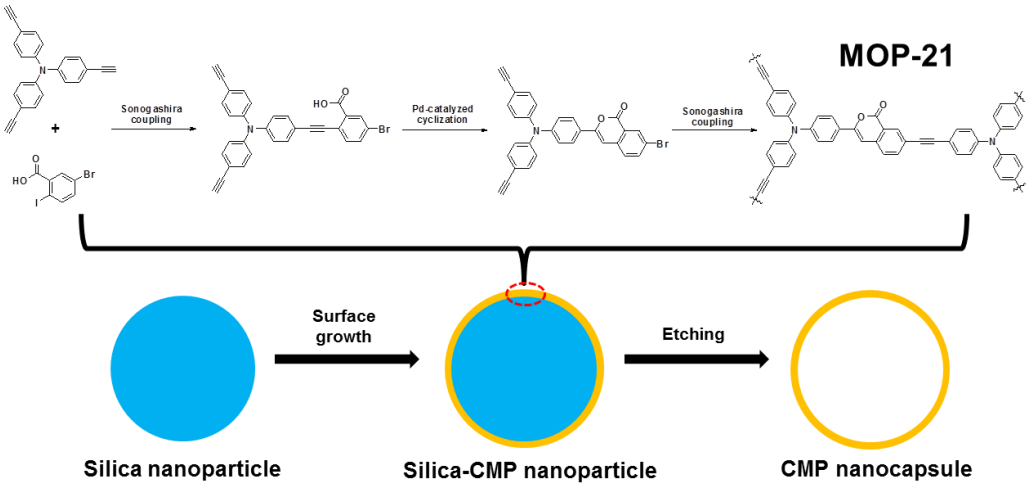

Figure I-20. Synthesis of MOP-21 using a sacrificial template.

I-3-2. MOPs with Membrane Structures

Polymers of intrinsic microporosity (PIMs) are soluble in organic solvents (Figure I-21).[63,64] Unlike crosslinked MOPs, PIMs have microporosity via their rigid and contorted structures between the polymer chains.[63] They are processed into porous films[63] and nanofibers.[64] PIM membranes have been used for gas storage and separation applications.

MOP growth on a substrate is another method to prepare film-type MOPs. Jiang's group prepared a carbazole-based conjugated MOP film by electrochemical deposition using multicycle cyclic voltammetry.[65] The thickness of the MOP was controllable by adjusting the reaction cycle number.

A freestanding film was observed when the thickness exceeded 50 nm. This film was useful for chemo-sensing and biosensing applications. Shi's group reported a MOP film grown on copper foil by means of oxidative coupling reaction.[66] Copper foil served as not only a catalyst for oxidative coupling but also as a template to provide the growth of the MOP film. Thomas's group prepared a MOP film grown on a gold electrode (Figure I-22).[67] The gold electrode was modified by 4-bromophenyl groups, thus facilitating covalent bonding between the MOP and the electrode.

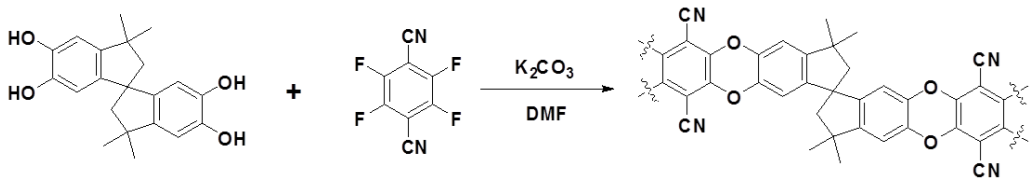

Figure I-21. Synthesis of a soluble PIM.

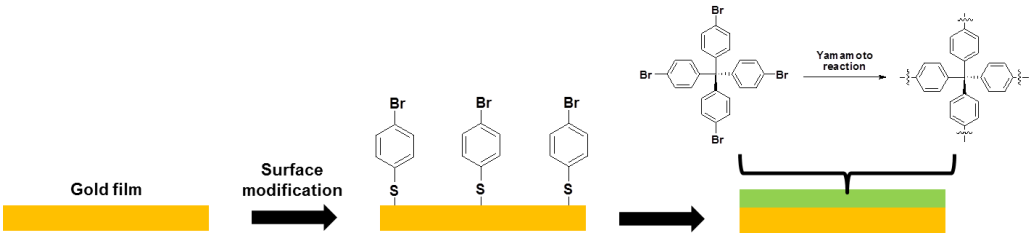

Figure I-22. Synthesis of MOP film on a functionalized gold film.

I-3-3. MOPs with Monolithic Morphologies with Hierarchical Porosity

Recently, hierarchically porous monoliths with macropores, mesopores, and micropores have received significant attention. They have highly interconnected open cell structures. The presence of macropores and mesopores provides rapid mass transfer and high accessibility to active sites.[51,68,69] Certain hierarchical porous monoliths have good mechanical stability and low flow resistance. These properties allow them to be used in specific applications such as chromatography[70] and flow-through catalysis.[69,71]

Zhang's group prepared a MOP aerogel (MOP-22) using a freeze-drying treatment (Figure I-23).[72] MOP-22 had a hierarchical pore structure and a high surface area (1701 m^2g^{-1}). Tan's group reported hierarchical porous monoliths using a high internal phase-emulsion method.[68] The porous polystyrene monoliths were post-crosslinked by the Friedel-Crafts reaction.

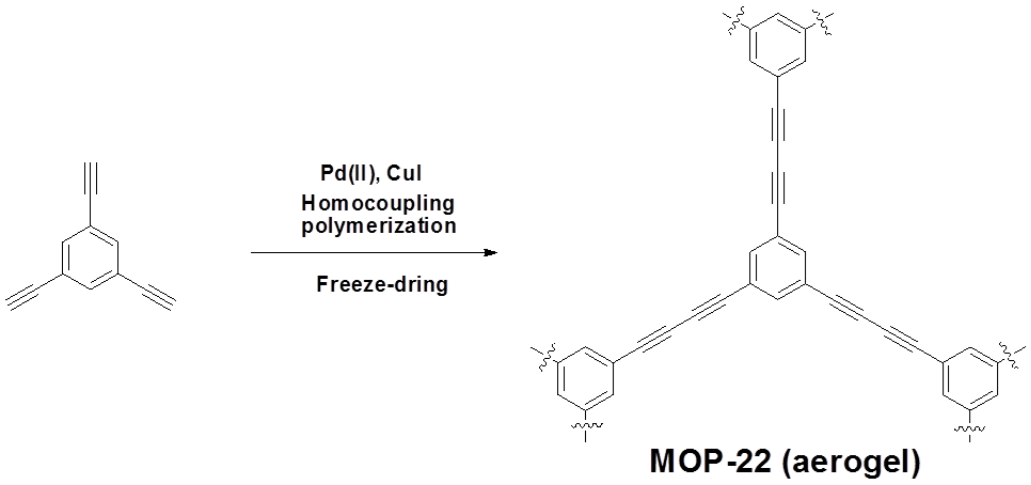

Figure I-23. Synthesis of MOP-22 with an aerogel structure.

Sponge-type materials have open cell structure, high porosity, low density, good mechanical stability and the elasticity.[58,71] Li's group fabricated a MOP nanotube-melamine sponge composite.[73] A MOP nanotube was synthesized within the melamine sponge. Due to its hydrophobicity and high porosity, the composite showed selective oil absorbency. Wang's group prepared an MOP-sponge composite via an oxidative coupling reaction.[71] A metalloporphyrin-based MOP homogeneously covered the surface of a melamine sponge. As a result of its hierarchical pore structure, the MOP-sponge composite showed improved catalytic performance compared to an identical MOP powder under a continuous flow condition.

I-4. Electrospinning for Substrates

Electrospinning is the powerful method by which to prepare nanofibers. Electrospun nanofibrous membranes have many advantages, such as large surface-to-volume ratios, high porosity, simple functionalization, and reliable mechanical stability.[74,75] Therefore, these materials can be used as porous substrates during the fabrication of MOPs with controllable forms.

I-4-1. Introduction to Electrospinning

Nanofibers are the fibrous materials with very small diameters ranging from several nanometers to several hundred nanometers. Due to their ultrafine nanostructures, nanofibers have large surface areas, high porosity, and small pore size distributions, thus offering many advantages in various fields.[76]

Electrospinning gained considerable academic attention in the 1990s for the fabrication of nanofibers after the principle of this method was initially described in 1934.[76,77] Compared to other techniques which can be used for the fabrication of nanofibers, such as the melt-blown and extrusion methods, electrospinning allows better control of the properties of nanofibers, such as the fiber diameters.[77,78]

An electrospinning setup is shown in Figure I-24. The setup has three basic elements: a capillary containing a reactant solution and a spinneret, a metal collector, and a high-voltage power supply. Two electrodes are connected to the spinneret and the collector. The reactant solution inside the capillary is fed at a controlled flow rate during the electrospinning process. When voltage (in kV) is applied to the system, the repulsive electrical force in the solution and the surface tension of the solution compete inside the solution. As a result, the pendant drop of the solution gains a conical structure, also known as a the Taylor cone.[76,79] When the applied voltage passes a critical point, the electrical force overcome the surface tension and charged liquid jets are formed from the Taylor cone and move towards the collector. During this process, the solvent is evaporated from the jets, causing the jet diameter decrease. Finally, the nanofibers are deposited on the collector, which are generally obtained in a membrane form.

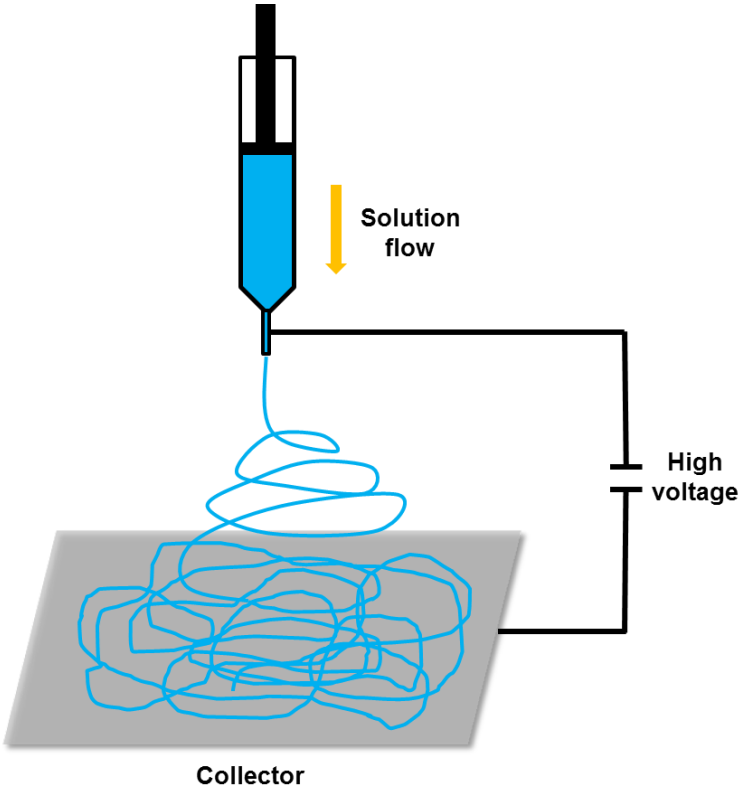

Figure I-24. Illustration of the electrospinning setup.

To control the morphology of nanofibers during electrospinning, many factors must be considered. The first examples are the intrinsic properties of the solution.[79] Because electrospinning us directly affected by the iscosity and conductivity of the reactant solution, it is important to choose the types of polymers and additives, the molecular weights of the polymers, the concentrations of the polymers and additives, and the types of solvents. Other factors are the processing conditions, including the applied voltage, the flow

rate of the solution, the diameter of the spinneret, the distance between the spinneret and the collector, the humidity, and temperature during the electrospinning process.[77,79]

I-4-2. Electrospinning for Substrates of Functional Materials

Electrospun nanofibers as substrates have been widely researched. Several preparation methods of functional materials based on electrospun nanofiber substrates are illustrated in Figure I-25.

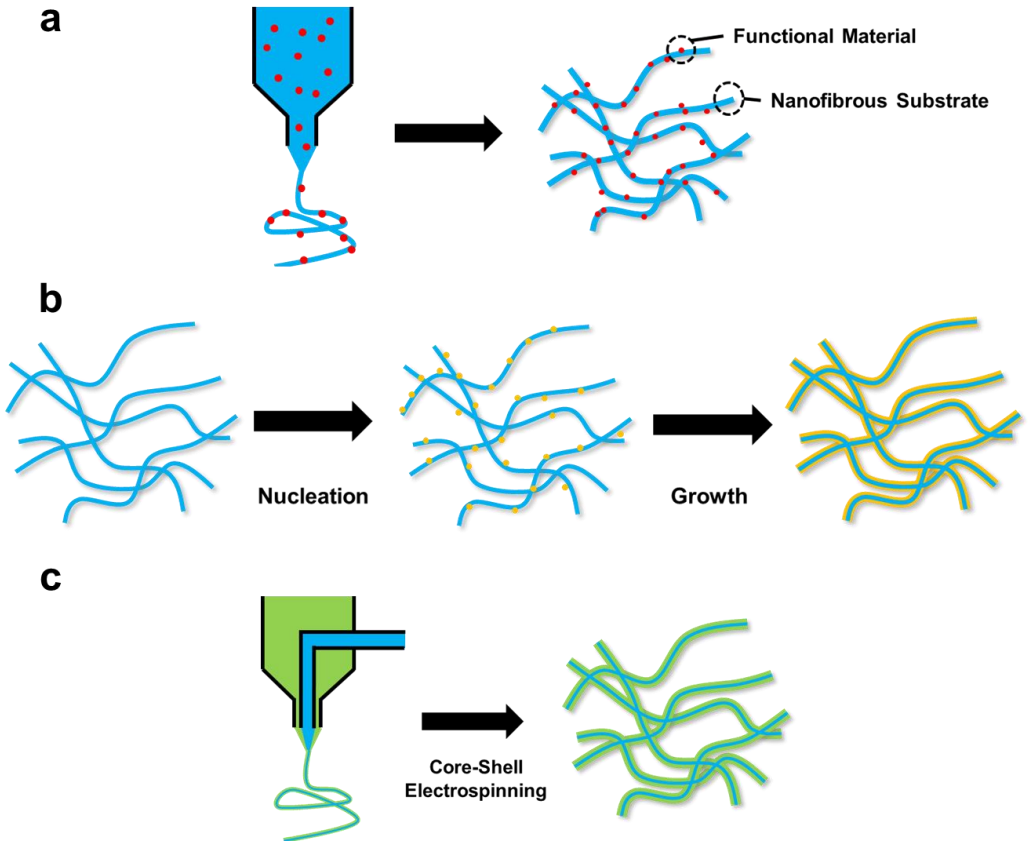

Figure I-25. Illustration of several preparation methods of functional materials based on electrospun substrates: (a) Blending electrospinning, (b) In-situ growth on a nanofiber, and (c) Core-shell electrospinning.

Blending electrospinning with polymers and functional materials is a feasible method. For instance, an upconversion-luminescence nanofibrous membrane was prepared by the combination of Ln^{3+}-doped $NaYF_4$ nanoparticles and polystyrene.[80] The nanoparticles were dispersed in the

polystyrene solution and successfully embedded into the transparent nanofibers. The membrane showed high luminescent sensitivity and exhibited good recyclability.

The in situ growth of functional materials on nanofiber substrates is another method to prepare functional composites. In general, functionalized nanofibers capable of interacting with desired materials are used as substrates. For example, polyaniline was coated onto a flexible TiO_2/SiO_2 nanofiber membrane via in situ post-polymerization.[81] Polyaniline could act as a photosensitizer for TiO_2 because the band gap of polyaniline is narrower than that of TiO_2. Therefore, this composite nanofiber showed good photocatalytic properties for organic dye degradation under a visible light condition. Lee's group prepared a crosslinked poly(vinyl alcohol) nanofibrous membrane containing silver nanoparticles.[83] The silver immobilized nanofibrous membrane demonstrated strong antimicrobial activity.

The fabrication of core-shell nanofibers can be achieved using a coaxial electrospinning method. During electrospinning, two different solutions pass through two concentrically aligned spinnerets. Functional materials are generally positioned in the shell while polymeric nanofiber cores act as the substrate. Yang's group reported core-shell type nanofiber-based gel polymer electrolytes by coaxial electrospinning.[82] Polymethylmethacrylate composed

the gelation shell, while polyacrylonitrile composed the rigid core nanofiber substrate. These electrolytes showed enhanced ionic conductivity, stability, and compatibility with a lithium-ion battery. A core-shell -structured polyacrylonitrile-polybenzoxazine nanofiber membrane was fabricated.[83] Because the electrospinning of polybenzoxazine itself is difficult due to its crosslinked structure, coaxial electrospinning was performed using a polyacrylonitrile solution (core) and a benzoxazine monomer solution (shell). The as-prepared membranes were thermally treated at 300 ^{o}C for the polymerization of benzoxazine. The core-shell porous membranes showed good non-fouling properties owing to the low surface free energy of polybenzoxazine.

I-4-3. Electrospinning for 3D Nanofibrous Structures

Recently, 3D ultralight materials have attracted attention in tissue engineering and energy applications.[79,84] Generally, such materials have an open cellular structure assembled by nanosized materials.[79] Electrospun nanofibers are good candidates for 3D ultralight materials due to their facile fabrication process and high surface-to-volume ratios.[79,85] However, electrospun nanofibers are obtained as close-packed membranes, which

seriously restricts the possibility of the formation of 3D architectures.[79,85,86] Various attempts have been made to achieve 3D nanofibrous structures.[86-88]

Nanofibrous aerogels have been prepared by the freeze-drying method.[84,85,89] Ding's group reported nanofiber-based cellular aerogel.[85] As shown in Figure I-26, electrospun nanofibers were dispersed into a solution containing a benzoxazine monomer and the nanofibrous cellular structure was obtained by means of a freeze-drying process. The as-prepared aerogels were thermally-treated for the formation of polybenzoxazine on the nanofiber surface, giving the aerogels good mechanical stability. The nanofiber-based aerogels had superelasticity and a very low density. Their morphology, size, and density were tunable by controlling the experimental conditions. The aerogels had potential applications in thermal insulation, sound adsorption, and oil-water separation.

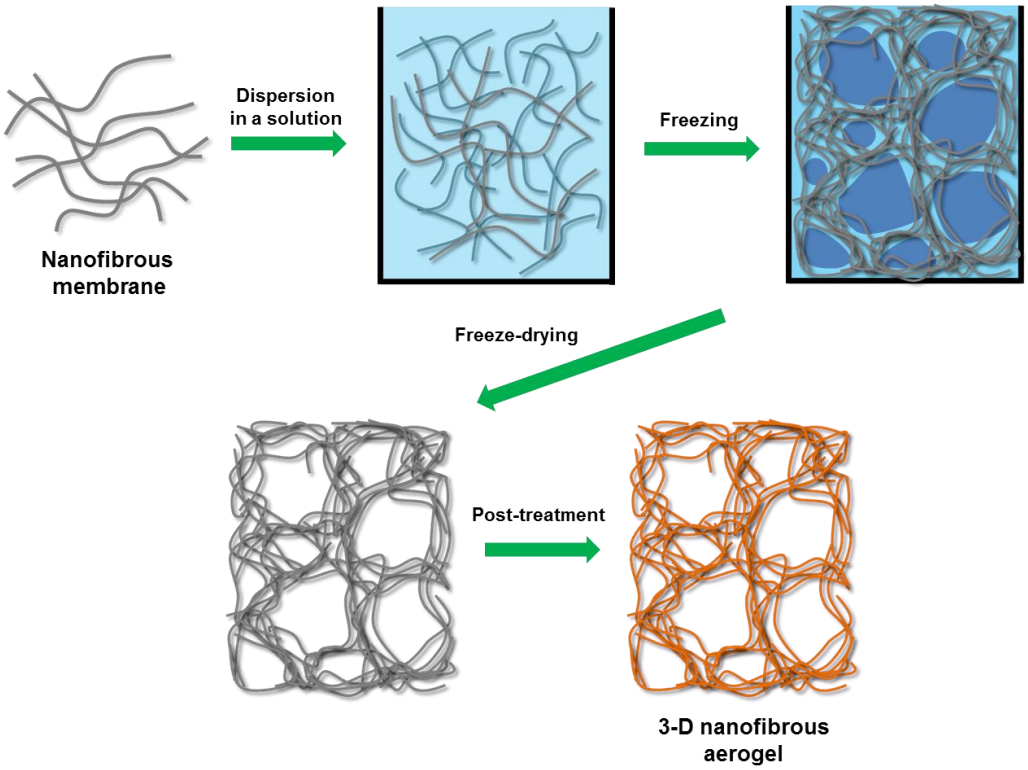

Figure I-26. Illustration of the preparation of nanofibrous aerogels by the freeze-drying method.

I-5. References

1. Sing, K. S. W.; Everett, D. H.; Haul, R. A. W.; Moscou, L.; Pierotti, R. A.; Rouquérol, J.; Siemieniewska, T. *Pure Appl. Chem.* **1985**, 57, 603–619.

2. Dawson, R.; Cooper, A. I.; Adams, D. J. *Prog. Polym. Sci.* **2012**, 37, 530-563.
3. Kim, S.; Lee, Y. M. *Prog. Polym. Sci.* **2015**, 43, 1-32.
4. McKeown, N. B.; Budd, P. M. *Macromolecules* **2010**, 43, 5163-5176.
5. Xu, Y.; Jin, S.; Xu, H.; Nagai, A.; Jiang, D. *Chem. Soc. Rev.* **2013**, 42, 8012-8031.
6. Ravikovitch, P. I.; Vishnyakov, A.; Russo, R.; Neimark, A. V. *Langmuir* **2000**, 16, 2311-2320.
7. Bruanuer, S.; Emmett, P. H.; Teller, E. *J. Am. Chem. Soc.* **1938**, 60, 309-319.
8. Walton, J. P. R. B.; Quirke, N. *Mol. Simul.* **1989**, 2, 361-391.
9. Zhang, P.; Zhu, H.; Dai, S. *ChemCatChem* **2015**, 7, 2788-2805.
10. Zhao, Y.; Liu, X.; Han, Y. *RSC Adv.* **2015**, 5, 30310-30330.
11. Barakat, T.; Rooke, J. C.; Tidahy, H. L.; Hosseini, M.; Cousin, R.; Lamonier, J. F.; Giraudon, J. M.; Weireld, G. D.; Su, B. L.; Siffert, S. *ChemSusChem* **2011**, 4, 1420-1430.
12. Dhakshinamoorthy, A.; Garcia, H. *Chem. Soc. Rev.* **2012**, 41, 5262-5284.
13. Liu, J.; Thallapally, P. K.; McGrail, B. P.; Brown, D. R.; Liu, J. *Chem. Soc. Rev.* **2012**, 41, 2308-2322.

14. Xu, S.; Luo, Y.; Tan, B. *Macromol. Rapid Commun.* **2013**, 34, 471-484.
15. Ratvijitvech, T.; Dawson, R.; Laybourn, A.; Khimyak, Y. Z.; Adams, D. J.; Cooper, A. I. *Polymer* **2014**, 55, 321-325.
16. Jiang, J. X.; Su, F.; Trewin, A.; Wood, C. D.; Campbell, N. L.; Niu, H.; Dickinson, C.; Ganin, A. Y.; Rosseinsky, M. J.; Khimyak, Y. Z.; Cooper. A. I. *Angew. Chem. Int. Ed.* **2007**, 46, 8574-8578.
17. Dawson, R.; Laybourn, A.; Khimyak, Y. Z.; Adams, D. J.; Cooper, A. I. *Macromolecules* **2010**, 43, 8524-8530.
18. Yuan, D.; Lu, W.; Zhao, D.; Zhou, H. C. *Adv. Mater.* **2011**, 23, 3723-3725.
19. Chen, L.; Honsho, Y.; Seki, S.; Jiang, D. *J. Am. Chem. Soc.* **2010**, 132, 6742-6748.
20. Chen, Q.; Wang, J. X.; Yang, F.; Zhou, D.; Bian, N.; Zhang, X. J.; Yan, C. G.; Han, B. H. *J. Mater. Chem.* **2011**, 21, 13554-13560.
21. Chen, Q.; Luo, M.; Hammershøj, P.; Zhou, D.; Han, Y.; Laursen, B. W.; Yan, C. G.; Han, B. H. *J. Am. Chem. Soc.* **2012**, 134, 6084-6087.
22. Holst, J. R.; Stöckel, E.; Adams, D. J.; Cooper, A. I. *Macromolecules* **2010**, 43, 8531-8538.
23. Li, B.; Gong, R.; Wang, W.; Huang, X.; Zhang, W.; Li, H.; Hu, C.; Tan, B. *Macromolecules* **2011**, 44, 2410-2414.

24. Wang, Z.; Zhang, B.; Yu, H.; Li, G.; Bao, Y. *Soft Matter*, **2011**, 7, 5723-5730.

25. Li, G.; Wang, Z. *Macromolecules* **2013**, 46, 3058-3066.

26. Pandey, P.; Katsoulidis, A. P.; Eryazici, I.; Wu, Y.; Kanatzidis, M. G.; and Nguyen, S. Y. *Chem. Mater.* **2010**, 22, 4974-4979.

27. Xu, C.; Hedin, N. *J. Mater. Chem. A* **2013**, 1, 3406-3414.

28. Schwab, M G.; Fassbender, B.; Spiess, H. W.; Thomas, A.; Feng, X.; Müllen, K. *J. Am. Chem. Soc.* **2009**, 131, 7216-7217.

29. Rabbani, M. G.; El-Kaderi, H. M. *Chem. Mater.* **2011**, 23, 1650-1653.

30. Katsoulidis, A. P.; He, J.; Kanatzidis, M. G. *Chem. Mater.* **2012**, 24, 1937-1943.

31. Qian, H.; He, Q.; Zheng, J.; Li, S.; Zhang, S. *Polymer* **2014**, 55, 550-555.

32. Lee, H.; Kim, H.; Choi, T. J.; Park, H. W.; Chang, J. Y. *Chem. Commun.* **2015**, 51, 9805-9808.

33. Kim, H.; Choi, T. J.; Cha, M. C.; Chang, J. Y. *J. Polym. Sci. Pol. Chem.* **2013**, 51, 3646-3653.

34. D' Alessandro, D. M.; Smit, B.; Long, J. R. *Angew. Chem. Int. Ed.* **2010**, 49, 6058-6082.

35. Bae, Y. S.; Snurr, R. Q. *Angew. Chem. Int. Ed.* **2011**, 50, 11586-11596.

36. Cavenati, S.; Grande, C. A.; Rodrigues, A. E. *J. Chem. Eng. Data* **2004**, 49, 1095-1101.

37. Chowdhury, P.; Bikkina, C.; Gumma, S. *J. Phy. Chem. C* **2009**, 113, 6616-6621.

38. Torrisi, A.; Mellot-Draznieks, C.; Bell, R. G. *J. Chem. Phys.* **2010**, 132, 044705.

39. Zhu, Y.; Long, H.; Zhang, W. *Chem. Mater*. **2013**, 25, 1630-1635.

40. İslamoğlu, T.; Rabbani, M. G.; El-Kaderi. H. M. *J. Mater. Chem. A* **2013**, 1, 10259-10266.

41. Fu, X.; Zhang, Y.; Gu, S.; Zhu, Y.; Yu, G.; Pan, C.; Wang, Z.; Hu. Y. *Chem. Eur. J.* **2015**, 21, 13357-13363.

42. Qian, X.; Zhu, Z. Q.; Sun, H. X.; Ren, F.; Mu, P.; Liang, W.; Chen, L.; Li, A. *ACS Appl. Mater. Interfaces* **2016**, 8, 21063-21069.

43. Yang, R. X.; Wang, T. T.; Deng, W. Q. *Sci. Rep.* **2015**, 5, 10155.

44. Kou, Y.; Xu, Y.; Guo, Z.; Jiang, D. *Angew. Chem. Int. Ed.* **2011**, 50, 8753-8757.

45. Xu, F.; Chen, X.; Tang, Z.; Wu, D.; Fu, R.; Jiang, D. *Chem. Commun.* **2014**, 50, 4788-4790.

46. Li, Z.; Zhang, Y.; Xia, Y.; Liu, X. *Chem. Commun.* **2016**, 52, 6613-6616.

47. Cheng, T.; Zhao, Q.; Zhang, D.; Liu, G. *Green Chem.* **2015**, 17, 2100-2122.

48. Copéret, C.; Comas-Vives, A.; Conley, M. P.; Estes, D. P.; Fedorov, A.; Mougel, V.; Nagae, H.; Núñez-Zarur, F.; Zhizhko, P. A. *Chem. Rev.* **2016**, 116, 323-421.

49. Song, C. E.; Lee, S. G. *Chem. Rev.* **2002**, 102, 3495-3524.

50. Price, P. M.; Clark, J. H.; Macquarrie, D. J. *J. Chem. Soc. Dalton Trans.* **2000**, 101-110.

51. Sun, Q.; Dai, Z.; Meng, X.; Xiao, F. S. *Chem. Soc. Rev.* **2015**, 44, 6018-6034.

52. Davis, M. E.; Lobo, R. F. *Chem. Mater.* **1992**, 4, 756-768.

53. Liu, D.; Guo, Q.; Hou, O.; Niwa, O.; You, T. *ACS Catal.* **2014**, 4, 1825-1829.

54. Zhang, Y.; Riduan, S. N. *Chem. Soc. Rev.* **2012**, 41, 2083-2094.

55. Chen, L.; Yang, Y.; Jiang, D. *J. Am. Chem. Soc.* **2010**, 132, 9138-9143.

56. Wang, F.; Mielby, J.; Richter, F. H.; Wang, G.; Prieto, G.; Kasama, T.; Weidenthaler, C.; Bongard, H. J.; Kegnæs, S.; Fürstner, A.; Schüth, F. *Angew. Chem. Int. Ed.* **2014**, 53, 1-5.

57. Zhang, Y.; Zhang, Y.; Sun, Y. L.; Du, X.; Shi, J. Y.; Wang, W. D.; Wang, W. *Chem. Eur. J.* **2012**, 18, 6328-6334.

58. Lim, Y.; Cha, M. C.; Chang, J. Y. *Sci. Rep.* **2015**, 5, 15957.

59. Liu, J.; Tobin, J. M.; Xu, Z.; Vilela, F. *Polym. Chem.* **2015**, 6, 7251-7255.

60. Tan, J.; Wan, J.; Guo, J.; Wang, C. *Chem. Commun.* **2015**, 51, 17394-17397.

61. Park, N.; Ko, K. C.; Shin, H. W.; Lee, S, M.; Kim, H. J.; Lee, J. Y.; Son, S. U. *J. Mater. Chem. A* **2016**, 4, 8010-8014.

62. Zhuang, X.; Gehrig, D.; Forler, N.; Liang, H.; Wagner, M.; Hansen, M. R.; Laquai, F.; Zhang, F.; Feng, X. *Adv. Mater.* **2015**, 27, 3789-3796.

63. Budd, P. M.; Elabas, E. S.; Ghanem, B. S.; Makhseed, S.; Mckeown, N. B.; Msayib, K. J.; Tattershall, C. E.; Wang, D. *Adv. Mater.* **2004**, 16, 456-459.

64. Zhang, C.; Li, P.; Cao, B. *Ind. Eng. Chem. Res.* **2015**, 54, 8772-8781.

65. Gu, C.; Huang, N.; Gao, J.; Xu, F.; Xu, Y.; Jiang, D. *Angew. Chem. Int. Ed.* **2014**, 53, 4850-4855.

66. Zhang, L.; Wang, K.; Qian, X.; Liu, H.; Shi, Z. *ACS Appl. Mater. Interfaces* **2013**, 5, 2761-2766.

67. Becker, D.; Heidary, N.; Horch, M.; Gernert, U.; Zebger, I.; Schmidt, J.; Fischer, A.; Thomas, A. *Chem. Commun.* **2015**, 51, 4283-4286.

68. Yang, X.; Tan, L.; Xia, L.; Wood, C. D.; Tan, B. *Macromol. Rapid Commun.* **2015**, 36, 1553-1558.

69. Darder, M. d. M.; Salehinia, S,; Parra, J.; Herrero-Martinez, J.; Svec, F.; Cerdà, V.; Palomino, G. T.; Maya, F. *ACS Appl. Mater. Interfaces* **2017**, 9, 1728-1736.

70. Svec, F.; Lv, Y. *Anal. Chem.* **2015**, 87, 250-273.

71. Wu, K.; Guo, J.; Wang, C. *Angew. Chem. Int. Ed.* **2016**, 55, 1-6.

72. Du, R.; Zhang, N.; Xu, H.; Mao, N.; Duan, W.; Wang, J.; Zhao, Q.; Liu, Z.; Zhang, J. *Adv. Mater.* **2014**, 26, 8053-8058.

73. Fan, W.; Liu, Z.; Zhang, Z.; Zhang, Q.; Ma, W.; Tan, D.; Li, A. *Micropor. Mesopor. Mater.* **2014**, 496, 335-340.

74. Destaye, A. G.; Lin, C. K.; Lee, C. K. *ACS Appl. Mater. Interfaces* **2013**, 5, 4745-4752.

75. Zhao. R.; Wang, Y.; Li, X.; Sun, B.; Wang, C. *ACS Appl. Mater. Interfaces* **2015**, 7, 26649-26657.

76. Frenot. A.; Chronakis, I. S. *Curr. Opin. Colloid Interface Sci.* **2003**, 8, 64-75.

77. Greiner, A.; Wendorff, J. H. *Angew. Chem. Int. Ad.* **2007**, 46, 5670-5703.

78. Teo, W. E.; Ramakrishna, S. *Nanotechnology* **2006**, 17, 89-106.

79. Sun, B.; Long, Y. Z.; Zhang, H. D.; Li, M. M.; Duvail, J. L.; Jiang, X. Y.; Yin, H. L. *Prog. Polym. Sci.* **2014**, 39, 862-890.

80. Liu, K. C.; Zhang, Z. Y.; Shan, C. X.; Feng, Z. Q.; Li, J. S.; Song, C. L.; Bao, Y. N.; Qi, X. H.; Dong, B.; *Light Sci. Appl.* **2016**, 5, e16136.

81. Liu, Z.; Miao, Y. E.; Liu, M.; Ding, Q.; Tjiu, W. W.; Cui, X.; Liu, T. *J. Colloid Interf. Sci.* **2014**, 424, 49-55.

82. Bi, H.; Sui, G.; Yang, X. *J. Power Sources* **2014**, 267, 309-315.

83. Kao, T. H.; Cheng, C. C.; Huang, C. F.; Chen, J. K. *RSC Adv.* **2015**, 5, 58760-58771.

84. Duan, G.; Jiang, S.; Moss, T.; Agarwal, S.; Greiner, A. *Polym. Chem.* **2016**, 7, 2759-2764.

85. Si, Y.; Yu, J.; Tang, X.; Ge, J.; Ding, B. *Nat. Commun.* **2014**, 5, 5802.

86. Zhang, D.; Chang, *J. Nano Lett.* **2008**, 8, 3283-3287.

87. Han, D.; Gouma, P. I. *Nanomedicine.* **2006**, 2, 37-41.

88. Sun, B.; Long, Y. Z.; Yu, F.; Li, M. M.; Zhang, H. D.; Li, W. J.; Xu, T. X. *Nanoscale* **2012**, 4, 2134-2137.

89. Duan, G.; Jiang, S.; Jérôme, V.; Wendorff, J. H.; Fathi, A.; Uhm, J.; Altstädt, V.; Herling, M.; Breu, J.; Freitag, R.; Agarwal, S.; Greiner, A. *Adv. Funct. Mater.* **2015**, 25, 2850-2856.

Chapter II.

Homogenized Electrospun Nanofiber Reinforced Microporous Polymer Sponge

II-1. Introduction

High surface areas and narrow pore sizes are the characteristics of microporous organic polymers (MOPs), allowing massive gas adsorptions and selective molecular storage.[1-6] MOPs are most outstanding in terms of flexibility in the structural design of microporous materials including zeolites and activated carbons. Many of MOPs have highly cross-linked conjugated structures. They are synthesized by numerous chemical reactions including metal-catalyzed cross-coupling reactions,[6-11] Friedel-Craft reactions,[3,12] Diels-Alder reaction,[13] thiol-yne reaction,[14] and condensation reactions.[2,15,16] In addition, specific functional groups can be introduced to the MOPs by the selection of appropriate comonomers or by post reactions.[17-19] Based on these synthetic advantages, MOPs have been tailored for specific applications such as gas storage and separation,[2,20,21] heterogeneous catalysis,[22,23] light emitting and harvesting,[5,6,24] energy storage,[25-27] sensors,[28] and superabsorption.[29]

The mechanical property of a material is one of the major factors, which determine its practical usage. Materials can have opportunities for broader applications by combining particular physicochemical properties with mechanical properties. There has been no extensive research focusing on the mechanical properties of microporous polymers, as they are usually obtained as powders with poor processability. Although there were some reports of

macroscopic gels formed during the polymerization of microporous polymers, the gels fragmented into small particles in the work-up processes.[11,30] The growth of MOP on a substrate is a way to circumvent the processability problem. A number of MOPs were polymerized on the surfaces of quartz,[31] poly(methyl methacrylate),[32] gold,[33] copper,[34] and graphene[35] and were obtained in various forms.

A sponge-like three-dimensional network structure has many attractive properties such as reversible compressibility, high porosity, low density, and flexibility. The combination of the MOPs and sponge-like network is particularly useful for fast adsorption and release of chemicals. There are several examples of MOP-based sponges for use in dye adsorption[36] and heterogeneous catalysis.[37] Nevertheless, it is still a challenge to synthesize MOP-based sponges with sufficient mechanical strength for practical applications.

In this study, we prepared a compressible and monolithic MOP composite sponge using a homogenized electrospun nanofiber as the reinforcement. The MOP composite sponge was obtained by the Sonogashira-Hagihara coupling reaction of an aryl halide and an alkyne in a dispersion of electrospun nanofibers. Herein, we describe the synthesis, microporosity, and adsorption properties of the composite sponge.

II-2. Experimental

Materials. Poly(vinyl alcohol) (PVA) (MW 85,000-124,000, 87-89 % hydrolyzed), tetraethyl orthosilicate (TEOS) (> 99.0 %), 1,4-dibromobenzene (98 %) and copper iodide (CuI) were purchased from Sigma-Aldrich. 2,5-Dibromoaniline (97 %), N,N-diisopropylethylamine (DIPEA) (98+ %) and methylene blue (MB) were obtained from ACROS Organics. 1,3,5-Triethynylbenzene (> 98.0 %) and bis(triphenylphosphine)palladium(II) dichloride ($PdCl_2(PPh_3)_2$) (> 98.0 %) were purchased from Tokyo Chemical Industry.

Electrospun PVA-Silica Nanofiber (PVASi) Mat. A PVA-silica nanofiber mat was prepared according to the literature procedure with minor modifications. A mixture of TEOS (1.09 g, 5.23 mmol), ethanol (1.09 g), H_2O (0.54 g) and HCl aqueous solution (0.1 mL, 2 M) were stirred at 60 ^oC for 1 h and then was added to a solution of PVA (0.275 g) in deionized H_2O (2 g). After stirring at 60 ^oC for 1 h, the resultant solution was transferred into a syringe equipped with an 18 gauge needle. The collecting plate covered with an aluminium foil was placed 15 cm from the tip of the needle. Electrospinning was performed at a voltage of 20 kV and a flow rate of 0.3 mL h^{-1}. The as-spun nanofiber mat was heated at 80 ^oC for 24 h in the atmosphere to finish the sol-

gel reaction.

Dispersion of PVASi by Homogenization. A mat of PVASi pieces (2 g, 2 x 2 cm^2) was homogenized in toluene (200 mL) at 13,000 rpm for 30 min using a Homogenizer HG-15D (DAIHAN Scientific Co). The homogenization process was repeated 3 times to give a homogeneous dispersion of PVASi.

Fabrication of MOP-Nanofiber Composite Monoliths (PVASi@TEDB-NH_2 and PVASi@TEDB). A dispersion of PVASi (6 mL) was mixed with toluene (1 mL) and DIPEA (2 mL) into the 20 ml vial and degassed by the nitrogen purging for 30 min. Subsequently, 1,3,5-triethynylbenzene (150 mg, 1 mmol) and 2,5-dibromoaniline (or 1,4-dibromobenzene, 1 mmol) were dissolved to the dispersion. And then, $PdCl_2(PPh_3)_2$ (20 mg, 24.7 μmol) and 6 mg of CuI (6 mg, 31.5 μmol) were added to the solution and sonicated for 5 s. the prepared mixture was treated at 80 ^oC for 24 h without stirring under aerobic condition. After reaction, a resultant composite was washed with ethanol and THF and dried under vacuum for 24 h at room temperature. Additionally, Soxhlet extraction was performed by methanol for 24 h. Finally, the monolithic MOP-PVASi composite sponge was obtained.

For comparison, microporous polymer TEDB-NH_2 and TEDB were

prepared in the same manner as described above except that a dispersion of PVASi was not added to the reaction mixture.

MB Adsorption Properties of PVASi@TEDB-NH_2. PVASi@TEDB-NH_2 (100 mg) was immersed in an aqueous MB solution (20 mL, 0.05 mM) and was manually compressed and released with a rate of 3 s for a cycle. The UV-Vis absorption of the solution was measured every 40 cycles. For comparison, a static adsorption experiment was carried out by immersing the same mass of PVASi@TEDB-NH_2 in the MB solution with stirring at 300 rpm and the UV-Vis absorption of the solution was monitored. The sponge was reused after the Soxhlet extraction with methanol and drying.

PVASi@TEDB-NH_2 Based Syringe Filter. PVASi@TEDB-NH_2 was prepared to have a diameter of 19 mm and a height of 10 mm and was used as a syringe filter. An aqueous MB solution (10 mL, 0.05 mM) was poured into a syringe plugged with PVASi@TEDB-NH_2 and filtered. The filtered solution was observed by the UV-Vis absorption spectra.

Instrumental Characterization. Scanning electron microscopy (SEM) images were obtained by a Carl Zeiss SUPRA 55VP. Transmission electron

microscopy (TEM) images were measured by a JEM-2100 operating at 200 kV. TEM samples were dispersed in THF and a drop of the mixture was placed on a carbon-coated copper TEM grid. Energy-dispersive X-ray spectroscopy (EDS) elemental maps were obtained using an Oxford instrument X-MaxN detector and analyzed with an AZtecEnergy EDS analyser. Solid-state ^{13}C NMR spectra were recorded on a Bruker Avance 400WB spectrometer (100 MHz) equipped with a CP-MAS probe. Powder X-ray diffraction (PXRD) patterns were measured using a New D8 Advance (Cu K_α radiation, λ = 1.54 Å). Thermogravimetric analyses (TGA) were performed on a TA modulated TGA2050 with a heating rate of 10 ℃/min under nitrogen. The FT-IR spectra were measured by a PERKIN ELMER Spectrum GX I spectrometer using KBr pellets. The compression tests were performed by an Instron 5543 universal testing machine. A cylindrical sponge having a diameter of 21 mm and height of 17 mm was used for the measurement. The strain-stress curves were recorded at a strain rate of 5 mm min^{-1}. 10 cycles of the loading-unloading test was measured at a strain rate of 50 mm min^{-1}. N_2 adsorption-desorption isotherms and CO_2 uptake properties were investigated by a Belsorp-Max (BEL Japan, Inc.) apparatus. UV-Vis spectra were obtained with a Sinco S-3150 spectrometer.

II-3. Results and Discussion

II-3-1. Synthesis and the Morphology of the MOP-Nanofiber Composites

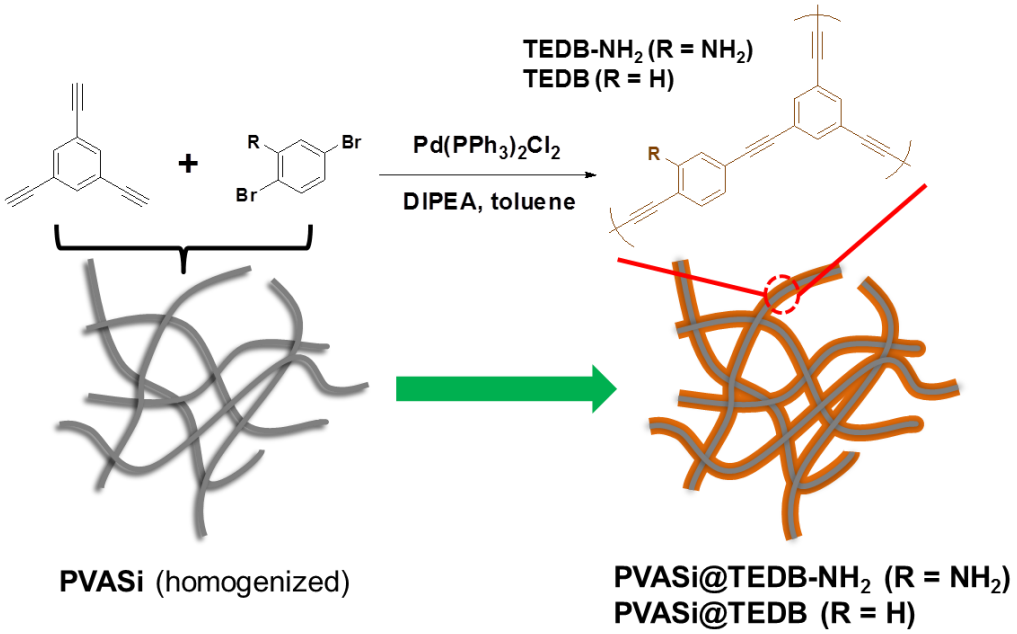

Scheme II-1. Synthesis of PVASi@TEDB-NH_2 and PVASi@TEDB.

Our synthetic approach to the MOP-electrospun nanofiber composite sponge is shown in Scheme II-1. The Sonogashira-Hagihara coupling reaction is a mild and efficient method to form a conjugated structure and has been considerably used to synthesize a microporous polymer.[7,8,10,11] 1,4-Dibromobenzene and 2,5-dibromoaniline were chosen as the aryl halides and 1,3,5-triethynylbenzene as the aryl acetylene monomer for the synthesis of the

MOPs with highly crosslinked structures. The Sonogashira–Hagihara coupling reaction between these monomers has been reported to yield microporous polymers in a powder form.[38,39] In this study, two polymers, TEDB and TEDB-NH_2, were also obtained as powders from the reaction of 1,3,5-triethynylbenzene with 1,4-dibromobenzene and 2,5-dibromoaniline, respectively (Figure II-1a, b). TEDB and TEDB-NH_2 showed a BET surface area of 718 and 548 m^2g^{-1}, respectively (Figure II-1c, d).

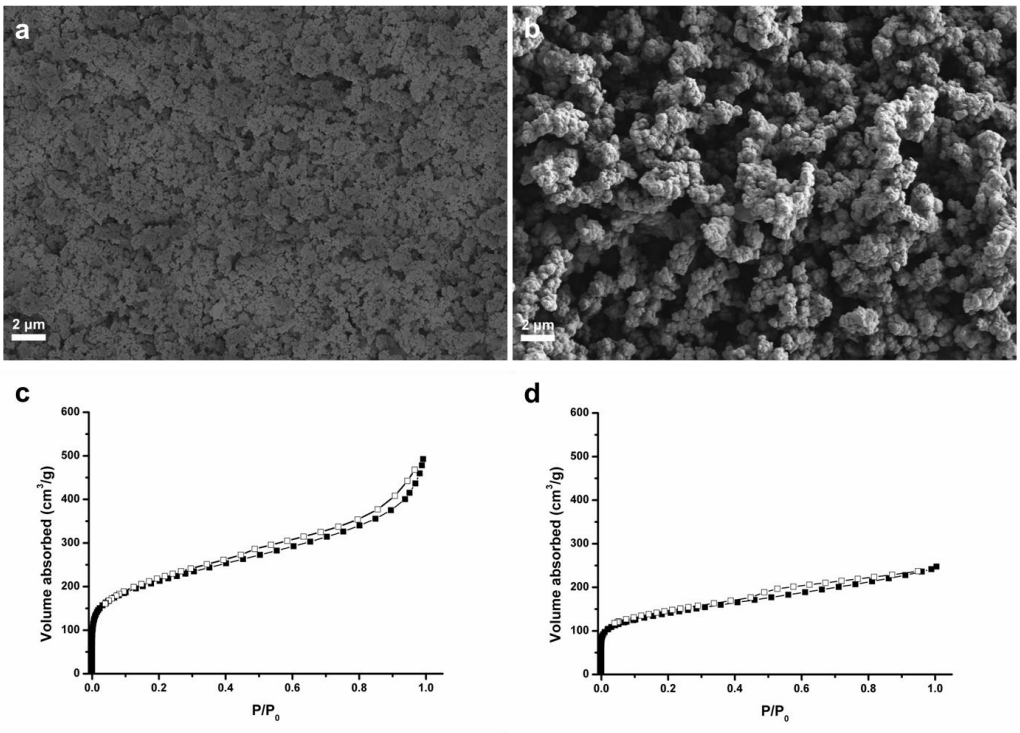

Figure II-1. SEM images of (a) TEDB and (b) TEDB-NH_2. N_2 adsorption-desorption isotherms measured at 77 K for (c) TEDB and (d) TEDB-NH_2.

The MOP growth on the electrospun fiber was attempted by carrying out the Sonogashira-Hagihara coupling reaction of 1,4-dibromobenzene or 2,5-dibromoaniline with 1,3,5-triethynyl-benzene in the presence of homogenized PVASi nanofibers prepared from a solution of PVA and TEOS. PVASi showed good chemical and thermal stability, because of the crosslinked structure resulting from the reaction between the hydroxyl groups of PVA and TEOS.[40,41] PVASi was obtained as a nonwoven mat. The SEM and TEM images showed that PVASi had a smooth surface and an average fiber diameter of 230 nm (Figure II-2). In order to secure sufficient area for the MOP growth, the PVASi mat was cut into pieces, and they were homogenized in toluene until a stable dispersion was formed (Figure II-3a, b). The homogenized PVASi nanofibers had a length ranging from dozens to hundreds of micrometers (Figure II-3c).

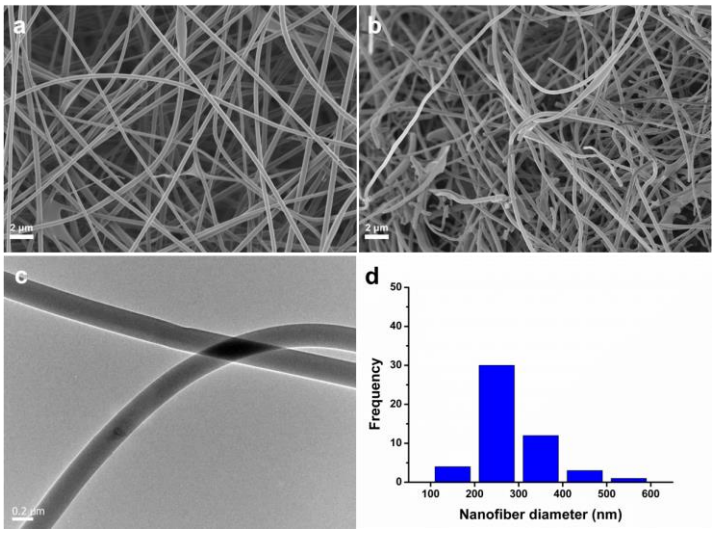

Figure II-2. SEM images of PVASi (a) before and (b) after homogenization. (c) TEM image and (d) the diameter distribution of as-spun PVASi.

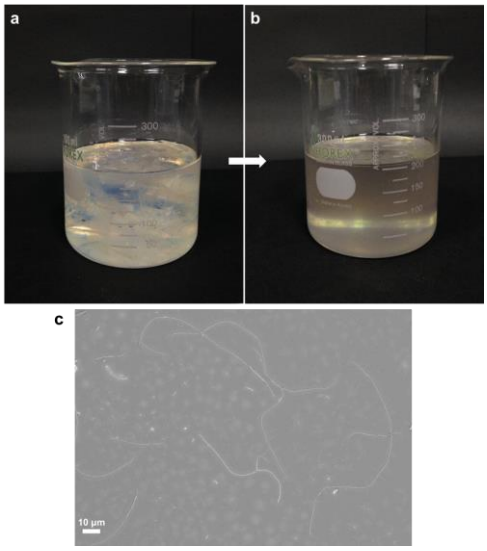

Figure II-3. Photographs of (a) pieces of a PVASi mat in toluene and (b) a dispersion of homogenized PVASi in toluene. (c) SEM image of individual homogenized PVASi nanofibers at low magnification.

Both PVASi@TEDB-NH_2 and PVASi@TEDB obtained from 2,5-dibromoaniline and 1,4-dibromobenzene, respectively, appeared to have monolithic sponge-like structures. However, their microstructures were very different. Figure II-4 shows the SEM and TEM images of PVASi@TEDB-NH_2. The SEM image of the composite prepared from 2,5-dibromoaniline (PVASi@TEDB-NH_2) showed entangled nanofibers and each nanofiber was uniformly wrapped with a thick layer of the polymer. An average layer thickness was 325 nm. The EDS analysis confirmed that nitrogen atoms from TEDB-NH_2 were uniformly dispersed on the surface of the nanofibers (Figure II-5). In contrast, the composite obtained from 1,4-bromobenzene (PVASi@TEDB) had a very thin polymer layer with an irregular surface. A considerable amount of the polymer powders was also found between the fibers (Figure II-6). This result could be attributed to the hydrophobic property of the polymer. TEDB consisted of hydrocarbon units and poorly interacted with the hydrophilic surface of PVASi.

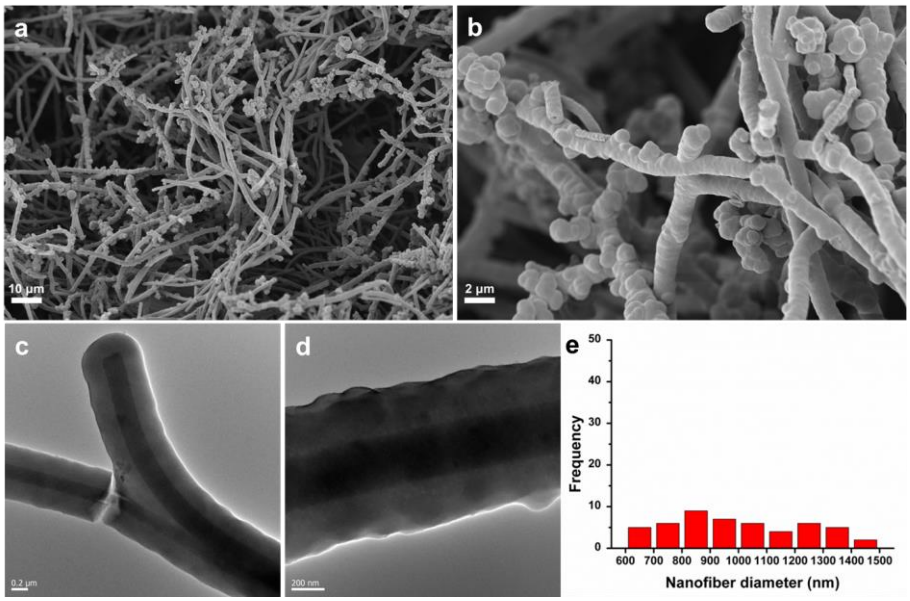

Figure II-4. (a), (b) SEM and (c), (d) TEM images of PVASi@TEDB-NH_2. (e) The diameter distribution of PVASi@TEDB-NH_2 nanofibers.

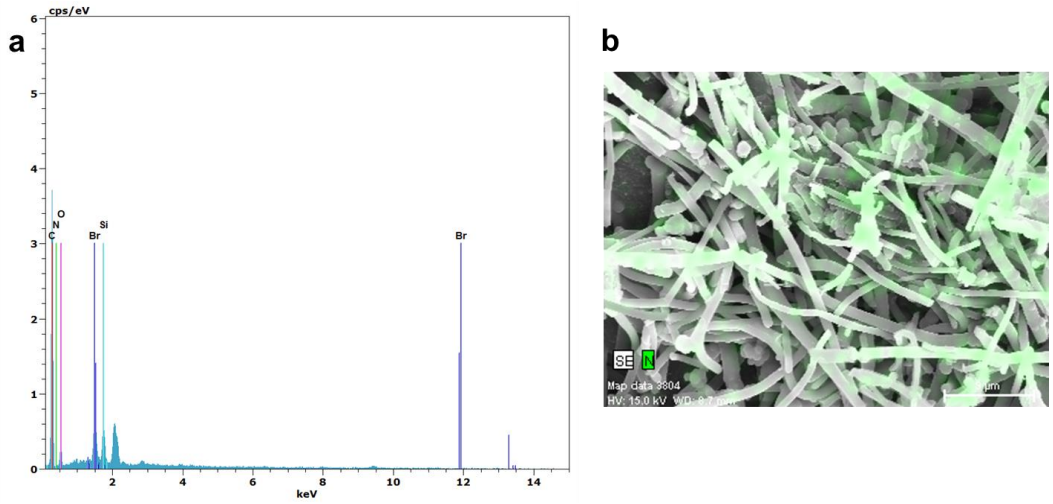

Figure II-5. (a) EDS elemental analysis and (b) mapping of nitrogen for PVASi@TEDB-NH_2.

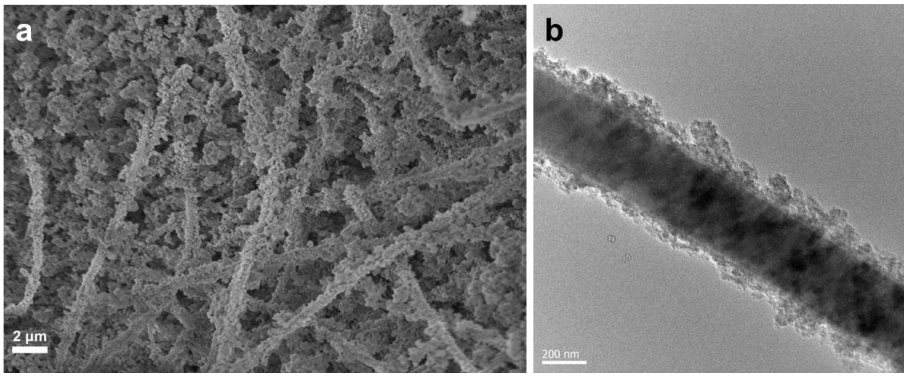

Figure II-6. (a) SEM and (b) TEM images of PVASi@TEDB.

Two factors affected the growth of the MOP on the electrospun fiber surface. The first one was the adsorption property of metallic catalysts on the nanofiber surface. PVASi had many hydroxyl groups on the surface that could interact with various metal ions.[42,43] Therefore, palladium (II) and copper (I) catalysts for the Sonogashira-Hagihara coupling reaction could be bound to the surface of PVASi to initiate the polymerization.[34] The second one was the interaction between the polymer and the nanofiber surface. TEDB-NH_2 obtained from 2,5-dibromoaniline had primary amino groups, which could form hydrogen bonds with the hydroxyl groups on the surface of PVASi.[44] As observed in the TEM images, PVASi@TEDB-NH_2 had a core-shell structure (Figure II-4c, d). TEDB-NH_2 coated the nanofibers and also acted as a material to weld the nanofibers, ensuring the construction of highly interconnected geometry as well as high structural stability.[45,46] The fused and entangled fiber

structure and a large void space conferred reversible elasticity to the composite under compressive force.[47] The average density of PVASi@TEDB-NH_2 was 30.4 mg cm^{-3}, which was comparable to those of silica aerogels[48] and carbon nanotube foams.[49]

II-3-2. Characterization of PVASi@TEDB-NH_2

As-prepared PVASi@TEDB-NH_2 exhibited reversible compressibility (Figure II-7). The compressive stress-strain curves of PVASi@TEDB-NH_2 measured at the set strain maxima of 20, 40 and 60% showed reversible stress-strain hysteresis (Figure II-7b) as observed in the open-cell foams.[47,50] During 10 loading-unloading cycles to a maximum strain of 40%, only a small change was observed in the stress-strain curves (Figure II-7c), indicating that the composite had a high mechanical strength against compression.[47,51]

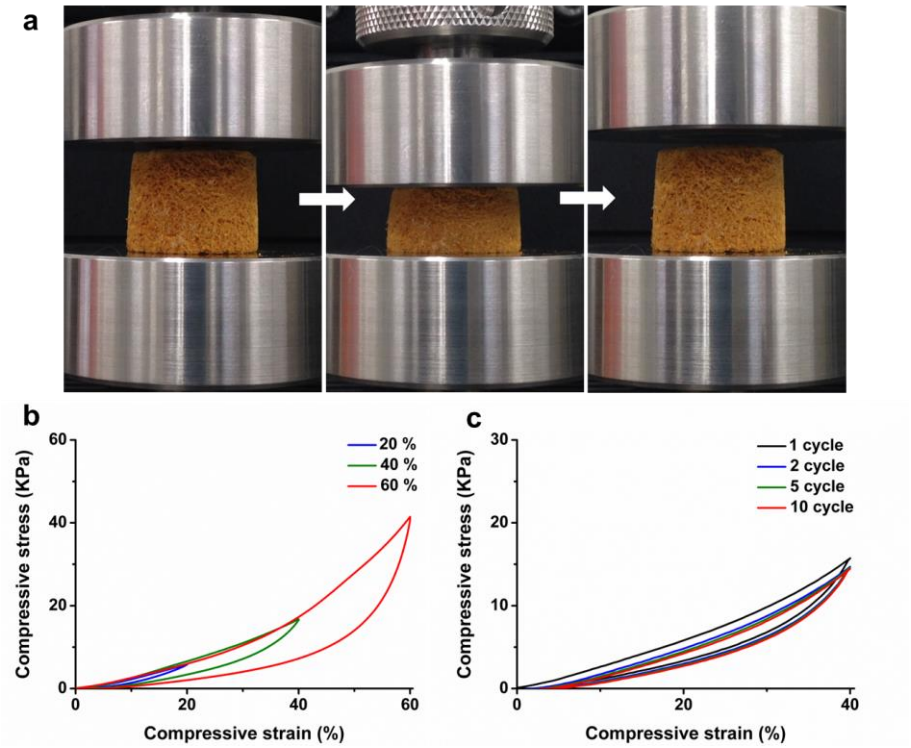

Figure II-7. (a) Images of PVASi@TEDB-NH_2 under loaded and unloaded conditions (strain = 40%). (b) Compressive stress-strain curves (maximum stress = 20, 40 and 60%) and (c) 10 cycles of loading-unloading test results of PVASi@TEDB-NH_2 (maximum strain = 40%).

The structures of TEDB-NH_2 and PVASi@TEDB-NH_2 were further characterized by solid state ^{13}C NMR and FT-IR spectroscopy (Figure II-8a, b). In the ^{13}C NMR spectrum, PVASi@TEDB-NH_2 showed the peaks for aromatic and acetylenic carbons of TEDB-NH2 at 149, 132, 124, 110 and 90 ppm[39,52]

and the peaks at 66, 45 and 21 ppm corresponding to the carbons of PVA containing the unhydrolyzed acetate side groups.[53] In the FT-IR spectrum of PVASi@TEDB-NH_2, the peaks for -C≡C- groups of TEDB-NH2 and Si-O-Si bonds of PVASi appeared at 2222 and 1075 cm^{-1}, respectively. The PXRD patterns of PVASi@TEDB-NH_2 and TEDB-NH_2 did not show any distinct peaks, suggesting that they had amorphous structures (Figure II-8c).

PVASi@TEDB-NH2 was thermally stable up to 300 ^oC when measured by TGA (Figure II-8d). The char yields of PVASi, TEDB-NH_2 and PVASi@TEDB-NH2 at 800 ^oC were 55.5, 79.4 and 73.2 wt%, respectively. We calculated the content of PVASi (Y) in PVASi@TEDB-NH_2 to be 25.9 wt% using the following equation:

$$C_1 \times (Y/100) + C_2 \times \{(100-Y)/100\} = C_3 \quad (1)$$

where C_1, C_2, C_3 are the char yields of PVASi, TEDB-NH_2 and PVASi@TEDB-NH_2, respectively.

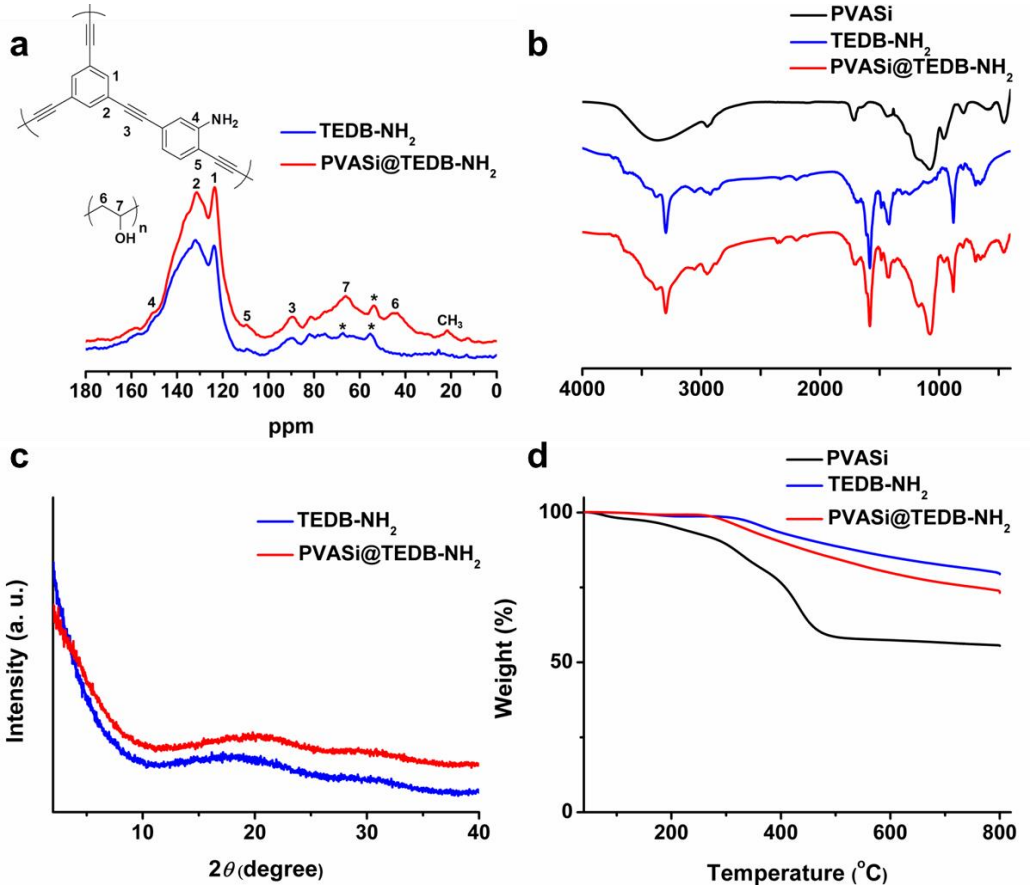

Figure II-8. (a) Solid state ^{13}C CP/MAS NMR spectra, (b) FT-IR spectra, and (c) PXRD patterns of TEDB-NH_2 and PVASi@TEDB-NH_2. (d) TGA thermograms of PVASi, TEDB-NH_2, and PVASi@TEDB-NH_2.

II-3-3. Porosity of PVASi@TEDB-NH_2

The porosities of PVASi@TEDB-NH2 and TEDB-NH2 were investigated by cryogenic N_2 adsorption-desorption analysis (Figure II-9a). Both materials

showed a combination of type I and IV isotherms,[54] indicating the existence of micropores and mesopores inside the materials. The average BET surface areas of PVASi@TEDB-NH_2 and TEDB-NH_2 for three time measurements were 447 and 506 m^2g^{-1}, respectively. The surface area of PVASi@TEDB-NH_2 was slightly lower than TEDB-NH_2 because of the presence of PVASi nanofibers which didn't have microporosity. The N_2 adsorption-desorption isotherms of PVASi@TEDB-NH_2 and TEDB-NH_2 showed similar patterns, indicating that the pore structure of TEDB-NH_2 was not significantly changed by the PVASi substrate from which the polymer was grown. The non-local density functional theory (NLDFT) pore size distributions (Figure II-9b) showed that both PVASi@TEDB-NH_2 and TEDB-NH_2 had the micropores and the mesopores. The CO_2 uptake amounts of PVASi@TEDB-NH_2 and TEDB-NH_2 measured at 273 K and 1 bar were 1.45 and 1.95 mmol g^{-1}, respectively (Figure II-10). The CO_2 uptake property of TEDB-NH_2 was similar to the result reported in the literature.[39]

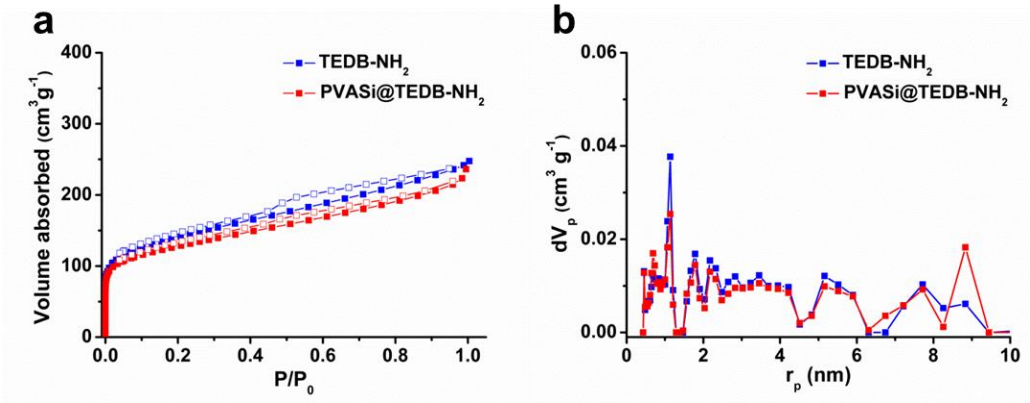

Figure II-9. (a) N_2 adsorption-desorption isotherms measured at 77 K and (b) NLDFT pore size distributions of PVASi@TEDB-NH_2 and TEDB-NH_2.

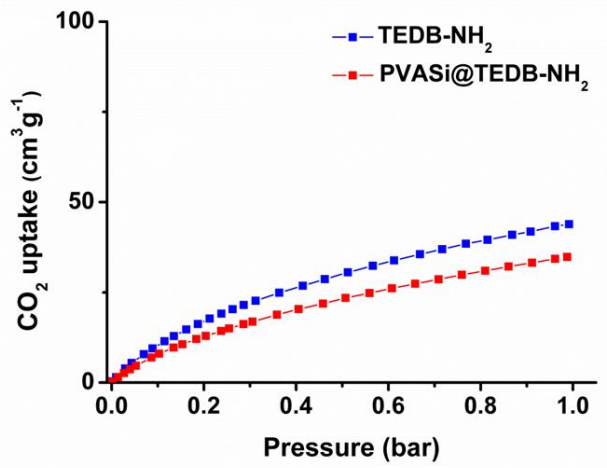

Figure II-10. CO_2 uptakes at 273 K of PVASi@TEDB-NH_2 and TEDB-NH_2.

II-3-4. Application of PVASi@TEDB-NH_2 as Organic Dye Adsorbent

Because of smaller pore sizes compared to those of mesoporous and macroporous materials,[55] microporous materials have a great potential as the adsorbents of toxic small molecules dissolved in water such as aromatic compounds,[56] organic dyes,[13,57] and endocrine disruptors.[58] The adsorption properties of PVASi@TEDB-NH_2 in an aqueous solution were investigated using MB as the model pollutant.

PVASi@TEDB-NH_2 was immersed in an aqueous MB solution and manually compressed and released in situ at a rate of ~3 s per cycle. Figure II-11 shows the UV-Vis spectra of the MB solution (0.05 mM). After 360 compression-release cycles, the absorbance of the solution reached zero, indicating the complete removal of MB as we could observe with naked eye (Figure II-12a). When the composite was allowed to absorb MB without the compression and release, a very small amount of the dye was removed in the same period time. Relatively more MB was adsorbed by PVASi@TEDB-NH_2 with stirring, but its removal rate was still far lower than that of the compression and release method. This result clearly stated the advantage of the compressible microporous material as an adsorbent. When PVASi@TEDB-NH_2 was compressed in the MB solution, inner pores were closely packed and deformed[47] and the air inside the composite sponge escaped. When the pressure was released, the composite sponge returned to the initial volume and

absorbed the solution. Through this process, more MB molecules could be transferred to and entered in the micropores of PVASi@TEDB-NH_2 by the capillary force.[59] Since the mass transportation in the micropores is relatively inhibited rather than the mesopores and the macropores, dye molecules were efficiently captured and confined inside the micropores. In addition, hydrophilic amine groups within the frame could help TEDB-NH_2 to have the affinity with water.[55,60] Figure II-13 shows the water absorption property of the composite sponge. PVASi@TEDB-NH_2 was floating on water at the beginning. After 10 cycles of compression and release, however, the composite sponge was immersed in water. Although the surface of PVASi@TEDB-NH_2 was hydrophobic, the compression and release process allowed the rapid absorption of water. The dye adsorbed PVASi@TEDB-NH_2 was simply regenerated by the Soxhlet extraction with methanol and could be reused. MB adsorption efficiency of the sponge was maintained even after the 5-time cyclic adsorption test (Figure II-12b).

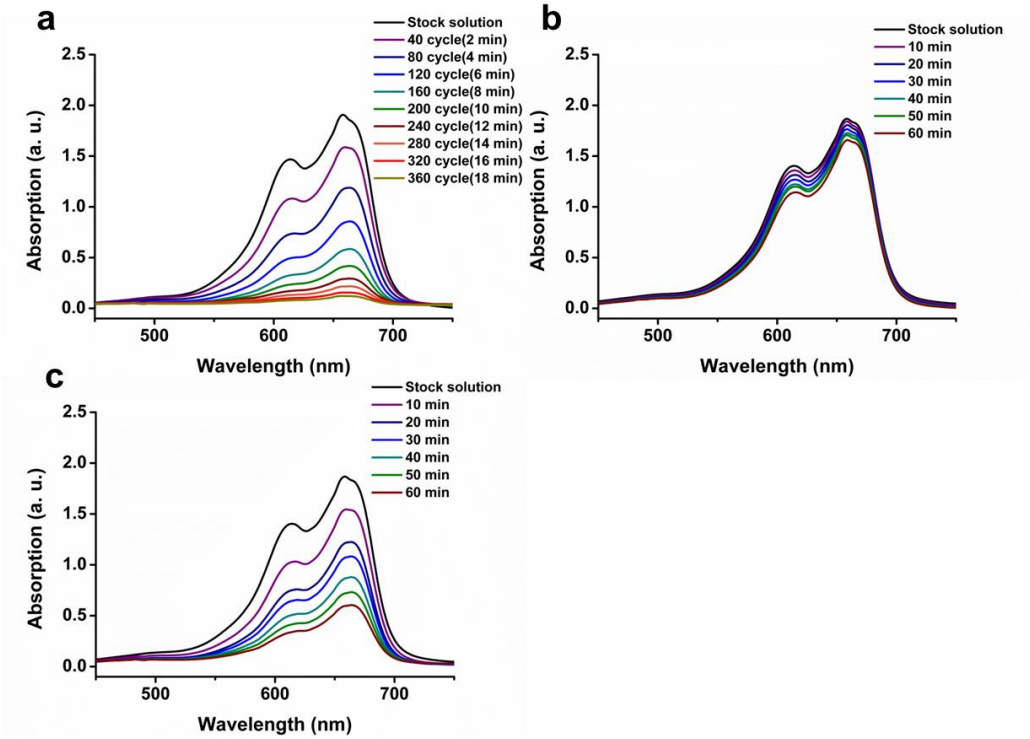

Figure II-11. UV–vis spectra of the aqueous MB solution (initial concentration = 5 x 10^{-5} M) measured after removing the dye by (a) compression and release process and by static adsorption (b) without stirring and (c) with stirring.

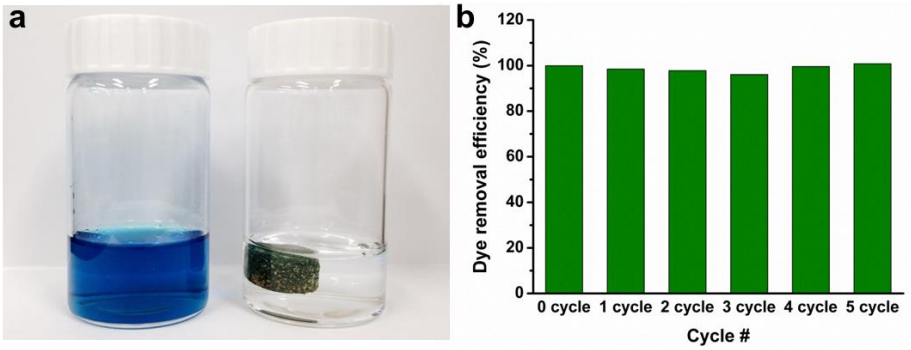

Figure II-12. (a) Photographs of aqueous MB solutions before (left) and after (right) adsorption. (b) Recycle test results of PVASi@TEDB-NH_2 for MB adsorption by the compression and release process.

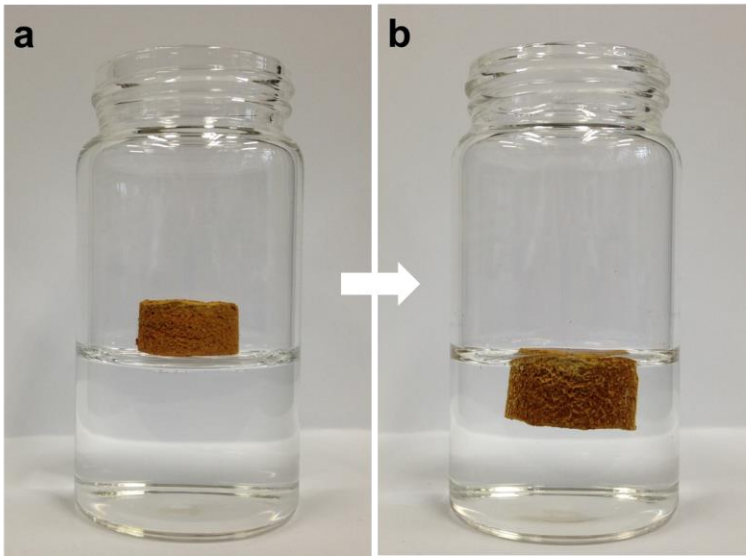

Figure II-13. Photographs of PVASi@TEDB-NH_2 in water (a) before and (b) after 10 cycles of compression and release.

A syringe filtration is another fast and efficient method of separation.[61,62] PVASi@TEDB-NH_2 can be used as a syringe filter because of its monolithic property, compressibility and hierarchical porosity. PVASi@TEDB-NH_2 was prepared that fitted into a syringe and used for filtration. The blue MB solution turned colorless after filtration (Figure II-14a), and the UV-Vis spectrum of the filtrate proved that MB molecules were completely removed (Figure II-14b). A syringe filter was recycled through the Soxhlet extraction and reused five times without significant deterioration in the adsorption property (Figure II-15).

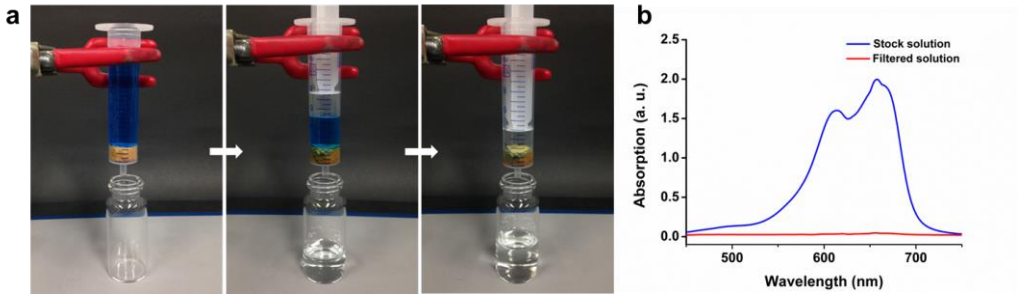

Figure II-14. (a) Sequential photographs of the filtration process using a PVASi@TEDB-NH_2 syringe filter. (b) UV–vis spectra of the aqueous MB solution before and after the filtration.

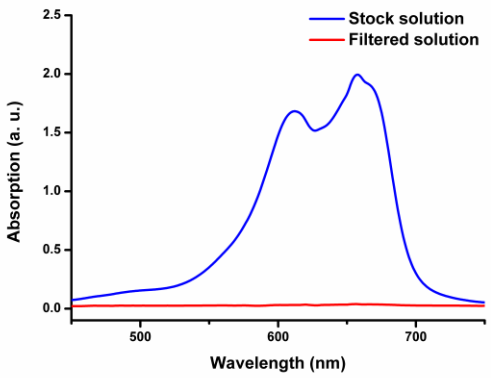

Figure II-15. UV-Vis spectrum of the aqueous MB solution measured after filtration with a five times regenerated syringe filter.

II-4. Conclusions

In summary, a compressible MOP-nanofiber composite, PVASi@TEDB-NH_2, was fabricated via the Sonogashira-Hagihara coupling reaction of 2,5-dibromoaniline and 1,3,5-triethynylben-zene in a dispersion of homogenized PVASi nanofibers. The microstructure analyses revealed that PVASi@TEDB-NH_2 had a core-shell structure, in which TEDB-NH2 uniformly coated the PVASi nanofibers. The PVASi nanofibers were interconnected by entanglement, and the junctions were bonded with the polymer, providing the composite with structural stability and compressibility. The composite was compressed and

released repeatedly, allowing the rapid removal of a pollutant in water. It was anticipated that the synthetic method of MOPs using electrospun nanofibers as the substrates would open a new way to fabricate monolithic and structurally stable functional microporous polymer composites.

II-5. References

1. Yuan, S.; Dorney, B.; White, D.; Kirklin, S.; Zapol, P.; Yu, L.; Liu, D. J. *Chem. Commun.* **2010**, *46*, 4547–4549.
2. Xu, C.; Hedin, N. *J. Mater. Chem. A* **2013**, *1*, 3406-3414.
3. Xiang, L.; Zhu, Y.; Gu, S.; Chen, D.; Fu, X.; Zhang, Y.; Yu, G.; Pan, C.; Hu, Y. A. *Macromol. Rapid Commun.* **2015**, *36*, 1566–1571.
4. Pandey, P.; Katsoulidis, A.P.; Eryazici, I.; Wu, Y.; Kanatzidis, M.G.; Nguyen, S. T. *Chem. Mater.* **2010**, *22*, 4974–4979.
5. Jiang, J. X.; Trewin, A.; Adams, D. J.; Cooper, A. I. *Chem. Sci.* **2011**, *2*, 1777–1781.
6. Chen, L.; Honsho, Y.; Seki, S.; Jiang, D. *J. Am. Chem. Soc.* **2010**, *132*, 6742–6748.
7. Fischer, S.; Schimanowitz, A.; Dawson, R.; Senkovska, I.; Kaskel, S.; Thomas, A. *J. Mater. Chem. A* **2014**, *2*, 11825–11829.

8. Lim, H.; Chang, J. Y. *Macromolecules* **2010**, *43*, 6943–6945.
9. Schmidt, J.; Werner, M.; Thomas, A. *Macromolecules* **2009**, *42*, 4426–4429.
10. Jiang, J. X.; Su, F.; Trewin, A.; Wood, C.D.; Niu, H.; Jones, J. T. A.; Khimyak, Y. Z.; Cooper, A. I. *J. Am. Chem. Soc.* **2008**, *130*, 7710–7720.
11. Jiang, J.X.; Su, F.; Trewin, A.; Wood, C.D.; Campbell, N. L.; Niu, H.; Dickinson, C.; Ganin, A. Y.; Rosseinsky, M. J.; Khimyak, Y. Z.; Cooper, A. I. *Angew. Chemie. Int. Ed.* **2007**, *46*, 8574–8578.
12. Lim, H.; Cha, M. C.; Chang, J. Y. *Polym. Chem.* **2012**, *3*, 868–870.
13. Kim, H.; Choi, T.; Cha, M. C.; Chang, J. Y. *J. Polym. Sci. Part A Polym. Chem.* **2013**, *51*, 3646–3653.
14. Lee, H.; Kim, H.; Choi, T. J.; Park, H. W.; Chang, J. Y. *Chem. Commun.* **2015**, *51*, 9805–9808.
15. Li, G.; Zhang, B.; Yan, J.; Wang, Z. *J. Mater. Chem. A* **2014**, *2*, 18881–18888.
16. Nandi, S.; Werner-Zwanziger, U.; Vaidhyanathan, R. *J. Mater. Chem. A* **2015**, *3*, 21116–21122.
17. Xu, Y.; Jin, S.; Xu, H.; Nagai, A.; Jiang, D. *Chem. Soc. Rev.* **2013**, *42*, 8012–8031.

18. Dawson, R.; Cooper, A. I.; Adams, D. *J. Prog. Polym. Sci.* **2012**, *37*, 530–563.
19. Cooper, A.I. *Adv. Mater.* **2009**, *21*, 1291–1295.
20. Chen, Y.; Sun, H.; Yang, R.; Wang, T.; Pei, C.; Xiang, Z.; Zhu, Z.; Liang, W.; Li, A.; Deng, W. *J. Mater. Chem. A* **2015**, *3*, 87-91.
21. Bao, L.; Sun, H.; Zhu, Z.; Liang, W.; Mu, P.; Zang, J.; Li, A. *Mater. Lett.* **2016**, *178*, 5-9.
22. Ma, B.C.; Ghasimi, S.; Landfester, K.; Vilela, F.; Zhang, K. A. I. *J. Mater. Chem. A* **2015**, *3*, 16064–16071.
23. Zhang, Y.; Riduan, S. N. *Chem. Soc. Rev.* **2012**, *41*, 2083–2094.
24. Xu, Y.; Nagai, A.; Jiang, D. *Chem. Commun.* **2013**, *49*, 1591–1593.
25. Kou, Y.; Xu, Y.; Guo, Z.; Jiang, D. *Angew. Chemie. Int. Ed.* **2011**, *50*, 8753–8757.
26. Xu, F.; Chen, X.; Tang, Z.; Wu, D.; Fu, R.; Jiang, D. Chem. Commun., **2014**, *50*, 4788–4790.
27. Vilela, F.; Zhang, K.; Antonietti, M. *Energy Environ. Sci.* **2012**, *5*, 7819-7832.
28. Gu, C.; Huang, N.; Gao, J.; Xu, F.; Xu, Y.; Jiang, D. *Angew. Chemie. Int. Ed.* **2014**, *53*, 4850–4855.
29. Du, R.; Zhang, N.; Xu, H.; Mao, N.; Duan, W.; Wang, J.; Zhao, Q.;

Liu, Z.; Zhang, J. *Adv. Mater.* **2014**, *26*, 8053–8056.

30. Jiang, J. X.; Su, F.; Niu, H.; Wood, C. D.; Campbell, N. L.; Khimyak, Y. Z; Cooper, A. I. *Chem. Commun.* **2008**, *4*, 486–488.
31. Cha, M. C.; Lim, Y.; Chang, J. Y. *J. Polym. Sci. Part A Polym. Chem.* **2015**, *53*, 2336–2342.
32. Tan, J.; Wan, J.; Guo, J.; Wang, C. *Chem. Commun.* **2015**, *51*, 17394–17397.
33. Becker, D.; Heidary, N.; Horch, M.; Gernert, U.; Zebger, I.; Schmidt, J.; Fischer, A.; Thomas, A. *Chem. Commun.* **2015**, *51*, 4283–4286.
34. Zhang, L.; Wang, K.; Qian, X.; Liu, H.; Shi, Z. *ACS Appl. Mater. Interfaces* **2013**, *5*, 2761–2766.
35. Zhuang, X.; Gehrig, D.; Forler, N.; Liang, H.; Wagner, M.; Hansen, M. R; Laquai, F.; Zhang, F.; Feng, X. *Adv. Mater.* **2015**, *27*, 3789–3796.
36. Lim, Y.; Cha, M. C.; Chang, J. Y. *Sci. Rep.* **2015**, *5*, 15957.
37. Wu, K.; Guo, J.; Wang, C. *Angew. Chem. Int. Ed.* **2016**, *55*, 1-6.
38. Kiskan, B.; Weber, J. *ACS Macro Lett.* **2012**, *1*, 37–40.
39. Ratvijitvech, T.; Dawson, R.; Laybourn, A.; Khimyak, Y. Z.; Adams, D. J.; Cooper, A. I. *Polymer* **2014**, *55*, 321–325.
40. Pirzada, T.; Arvidson, S. A.; Saquing, C. D.; Shah, S. S.; Khan, S. A. *Langmuir* **2012**, *28*, 5834–5844.

41. Keshtkar, A. R.; Irani, M.; Moosavian, M .A. *J. Radioanal. Nucl. Chem.* **2013**, *295*, 563–571.
42. Wang, J.; Kondrat, S. A.; Wang, Y.; Brett, G. L.; Giles, C.; Bartley, J. K.; Lu, L.; Liu, Q.; Kiely, C. J.; Hutchings, G. J. *ACS Catal.* **2015**, *5*, 3575–3587.
43. Haider, S.; Park, S. Y. *J. Memb. Sci.* **2009**, *328*, 90–96.
44. Liu, Z.; Miao, Y. E.; Liu, M.; Ding, Q.; Tjiu, W. W.; Cui, X.; Liu, T. *J. Colloid Interface Sci.* **2014**, *424*, 49–55.
45. Lin, Z.; Gui, X.; Gan, Q.; Chen, W.; Cheng, X.; Liu, M.; Zhu, Y.; Yang, Y.; Cao, A.; Tang, Z. *Sci. Rep.* **2015**, *5*, 11336.
46. Kim, K. H.; Oh, Y.; Islam, M. F. *Nat. Nanotechnol.* **2012**, *7*, 562–566.
47. Si, Y.; Yu, J.; Tang, X.; Ge, J.; Ding, B. *Nat. Commun.* **2014**, *5*, 5802.
48. Pierre, A. C.; Pajonk, G. M. *Chem. Rev.* **2002**, *102*, 4243–4266.
49. Worsley, M. A.; Kucheyev, S. O.; Satcher, J. H.; Hamza, A. V.; Baumann, T. F. *Appl. Phys. Lett.* **2009**, *94*, 2007–2010.
50. Lorna, J. G.; Michael, F. A. *Cellular Solids: Structure and Properties*, 2nd ed; Cambridge University Press, 1997.
51. Ruan, C.; Ai, K.; Li, X.; Lu, L. *Angew. Chemie. Int. Ed.* **2014**, *53*, 5556–5560.
52. Dawson, R.; Laybourn, A.; Khimyak, Y. Z.; Adams, D. J.; Cooper, A. I.

Macromolecules **2010**, *43*, 8524–8530.

53. Terao, T.; Maeda, S; Saika, A. *Macromolecules* **1983**, *16*, 1535–1538.
54. Sing, K. S. W.; Everett, D. H.; Haul, R .A. W.; Moscou, L.; Pierotti, R. A.; Rouquérol, J.; Siemieniewska, T. *Pure Appl. Chem.* **1985**, *57*, 603-619.
55. Li, B.; Su, F.; Luo, H.; Liang, L.; Tan, B. *Microporous Mesoporous Mater.* **2011**, *138*, 207–214.
56. Ji, L.; Liu, F.; Xu, Z.; Zheng, S.; Zhu, D. *Environ. Sci. Technol.* **2009**, *43*, 7870–7876.
57. Yang, R. X.; Wang, T. T.; Deng, W .Q. *Sci. Rep.* **2015**, *5*, 10155.
58. Zhao, R. S.; Wang, X.; Yuan, J. P.; Zhang, L. L. *Microchim. Acta* **2009**, *165*, 443–447.
59. Zhuang, X.; Wan, Y.; Feng, C.; Shen, Y.; Zhao, D. *Chem. Mater.* **2009**, *21*, 706-716.
60. László, K. *Microporous Mesoporous Mater.* **2005**, *80*, 205–211.
61. Fu, G.; Su, Z.; Jiang, X.; Yin, *J. Polym. Chem.* **2014**, *5*, 2027–2034.
62. Lu, Y.; He, W.; Cao, T.; Guo, H.; Zhang, Y.; Li, Q.; Shao, Z.; Cui, Y.; Zhang, X. *Sci. Rep.* **2014**, *4*, 5792.

Chapter III.

Preparation of a Microporous Polymer Membrane Containing Pd Nanoparticles as a Catalytic Membrane

III-1. Introduction

Catalytic membranes are a class of heterogeneous catalysts, which have catalytic sites inside porous membrane supports. They can perform a catalytic reaction during diverse membrane processes, which have many advantages compared with other heterogeneous catalysts.[1] For instance, catalytic membranes are suitable for continuous catalytic processes, which can give steady conversion over time.[1-3] Also, they don't need to be removed from the reaction mixture after a reaction, which facilitates a reuse of catalysts.[3,4] Catalytic membranes have been used for various applications such as gas-phase reactions,[5-7] photocatalytic reactions[2,8,9] and liquid-phase reactions.[3,4,10] Catalytic membranes have been prepared using various organic and inorganic materials. Especially, polymeric materials for catalytic membranes have attracted a considerable interest because of some advantages such as low costs, good processability, and large scale preparation.[4,11,12]

Friedel-Crafts reaction between aromatic compounds is an efficient way to synthesize hypercrosslinked microporous polymers (HCPs).[13] Relatively cheap catalysts are used for Friedel-Crafts reaction. Various types of aromatic compounds are available for the reaction, which enables to produce diverse functional HCPs.[13-17] Several groups have studied HCP-based heterogeneous catalysts containing metal ions,[14,18] metal nanoparticles,[17,19,20] and

organocatalysts.[15,18] However, HCPs are general prepared in insoluble powder forms, which limits severely their applications for catalytic membranes. Recently, a HCP-based catalytic membrane was prepared by the in-situ Friedel-Crafts reaction of a polystyrene-ionic liquid membrane,[21] but studies on this topic are still sparse.

In this work, we prepared a HCP-based microporous catalytic membrane using an electrospun nanofiber membrane as a substrate. Electrospinning is a powerful method to make a membrane composed of nanofibers, showing a large surface area, high porosity, and reliable mechanical stability.[22,23] Moreover, an electrospun nanofiber membrane can be functionalized with various materials such as polymers, metal oxides, and metal-organic frameworks.[24-26] The HCP-based microporous membrane was obtained by carrying out the Friedel-Crafts reaction of an aromatic monomer in the presence of an aminated polyacrylonitrile (APAN) membrane. Palladium (Pd) nanoparticles were incorporated into the APAN membrane and used for a catalytic reduction of 4-nitrophenol (4-NP).

III-2. Experimental

Materials. 1,1'-Bi-2-naphthol (99 %), palladium chloride ($PdCl_2$) (59 wt% Pd) and diethylenetriamine were purchased from ACROS Organics. Dimethoxymethane (98 %), and sodium borohydride ($NaBH_4$) (95 %) were obtained from Tokyo Chemical Industry. Polyacrylonitrile (PAN) (MW ~ 150,000) and 4-nitrophenol (4-NP) (99 %) were purchased from Sigma-Aldrich. Iron (III) chloride anhydrous ($FeCl_3$) was purchased from Fisher chemicals. Sodium carbonate (Na_2CO_3) was obtained from Shinyo pure chemicals Co. Other solvents were purchased from Junsei Chemical. All materials were used without any purification.

Preparation of the Aminated PAN (APAN) Nanofibrous Membrane. PAN (0.6 g) was dissolved in DMF (5.4 g) at 50 ^{o}C. The PAN solution was transferred into a syringe with an 18 gauge needle. The syringe was placed 20 cm from the collecting plate covered with an aluminum foil. Electrospinning was performed at a voltage of 20 kV and a flow rate of 1.0 mL h^{-1}. The as-spun PAN nanofiber membrane was dried at 60 ^{o}C for 24 h.

The APAN nanofibrous membrane was prepared by an amination of the PAN membrane using diethylenetriamine. It was performed *via* the previously reported method.[27]

Preparation of the HCP-Nanofiber Composite Membrane (APAN-HCP). $FeCl_3$ (2594 mg, 1.6 * 10^{-2}mol) was dispersed in 40 mL of 1,2-dichloroethane. The APAN membrane (300 mg) and 1,1'-bi-2-naphthol (1145 mg, 4 * 10^{-3} mol) were added to the solution, which was stirred for 24 h at room temperature. Subsequently, dimethoxymethane (1219 mg, 1.6 * 10^{-2} mol) was added dropwise to the mixture. The mixture was heated to 80 ^{o}C with stirring at 400 rpm for 24 h. The as-prepared composite membrane was washed with THF and methanol and dried under vacuum at room temperature.

The Palladium Decorated HCP-Nanofiber Composite Membrane (APAN-HCP-Pd). $PdCl_2$ (140 mg) was dissolved in 70 mL of acetonitrile at 90 ^{o}C. APAN-HCP (350 mg) was immersed in the $PdCl_2$ solution at 90 ^{o}C with stirring at 300 rpm. After 24 h, the membrane was removed from the $PdCl_2$ solution and immersed in 100 mL of $NaBH_4$ solution (0.25 M of $NaBH_4$, H_2O : EtOH = 1 : 3) for 3 h. The resultant membrane was washed with H_2O and EtOH and dried under vacuum at room temperature.

Catalytic Reduction of 4-Nitrophenol by the Membrane Catalyst via the Filtration. 100 mL of a 4-nitrophenolate aqueous solution was prepared by mixing 50 mL of 4-NP solution (2 * 10^{-4} M) and 50 mL of $NaBH_4$ (8 * 10^{-2} M)

solution. APAN-HCP-Pd membrane having a circular shape with a diameter of 55 mm (0.72 mm thickness, 350 mg) was placed in a Buchner funnel with a filter paper as the support. The 4-nitrophenolate solution was passed through APAN-HCP-Pd by the vacuum pump and the filtrate was collected in a round-bottom flask. The filtration was ended within 3 minutes. The filtrate underwent the same process for the fifth time. UV-Vis spectroscopy was used to monitor the reduction of 4-NP.

Instrumental Characterization. The FT-IR spectrum was measured by a TENSOR27 FT-IR Spectrometer. Solid-state ^{13}C NMR spectrum was recorded on a Bruker Avance II spectrometer (125 MHz). Powder X-ray diffraction (PXRD) patterns were observed using a New D8 Advance (Cu K_α radiation, λ = 1.54 Å). Thermogravimetric analyses (TGA) were performed on a TA modulated TGA2050 with a heating rate of 10 ℃/min under nitrogen. Scanning electron microscopy (SEM) images were obtained by a Carl Zeiss SUPRA 55VP. Energy-dispersive X-ray spectroscopy (EDS) elemental map was obtained using an Oxford instrument X-MaxN detector and analyzed with an AZtecEnergy EDS analyzer. N_2 adsorption-desorption isotherms were investigated by a Belsorp-Max (BEL Japan, Inc.) apparatus. The tensile tests were performed by an Instron-5543 universal testing machine. Transmission electron microscopy (TEM) images were obtained using a Talos L120C

operating at 120 kV. TEM samples were prepared by dropping a dispersion of materials in EtOH on a carbon-coated copper TEM grid. X-ray photoelectron spectroscopy (XPS) was measured by a KRATOA AXIS-His spectrometer equipped with an Mg K_a X-ray source. Inductively coupled plasma mass spectrometry (ICP-MS) was measured by a Varian 820-MS to calculate a weight percentage of Pd in the membrane. Pd was dissolved in strong nitric acid before measurement. UV-Vis spectra were recorded with a Sinco S-3150 spectrometer.

III-3. Results and Discussion

III-3-1. Synthesis and Characterizations of a HCP-based Microporous Membrane

Our synthetic strategy to a HCP-based microporous membrane is shown in Scheme III-1. Friedel-Crafts reaction of an aromatic compound with dimethoxymethane has been reported to produce a microporous polymer.[28] We chose 1,1'-bi-2-naphthol as an aromatic monomer for the preparation of a HCP, which can chelate metal ions such as Mo, Pd, and Pt ions.[29]

Polyacrylonitrile (PAN) has been widely used for the production of nanofibrous membranes because of its low cost, thermal stability, chemical resistance, and mechanical stability.[30,31] Moreover, PAN nanofibers are easily functionalized by the reactions of cyano groups to be suitable for certain applications such as ion-exchange and metal ion adsorption.[31-34] In this study, an aminated polyacrylonitrile (APAN) nanofibrous membrane was chosen as a substrate because of its outstanding adsorption properties of metal ions including Fe(III).[33,34] In the Friedel-Crafts reaction with $FeCl_3$ as a catalyst, Fe(III) ions were expected to be bound to APAN nanofibers and to act as reaction sites for the polymerization.[35,36] Also, the aromatic monomer, 1,1'-bi-2-naphthol, could interact with amine groups of APAN nanofibers through

hydrogen bonding. The APAN nanofiberous membrane was prepared by the amination reaction of a electrospun PAN membrane with diethylenetriamine according to the previously reported method.[27]

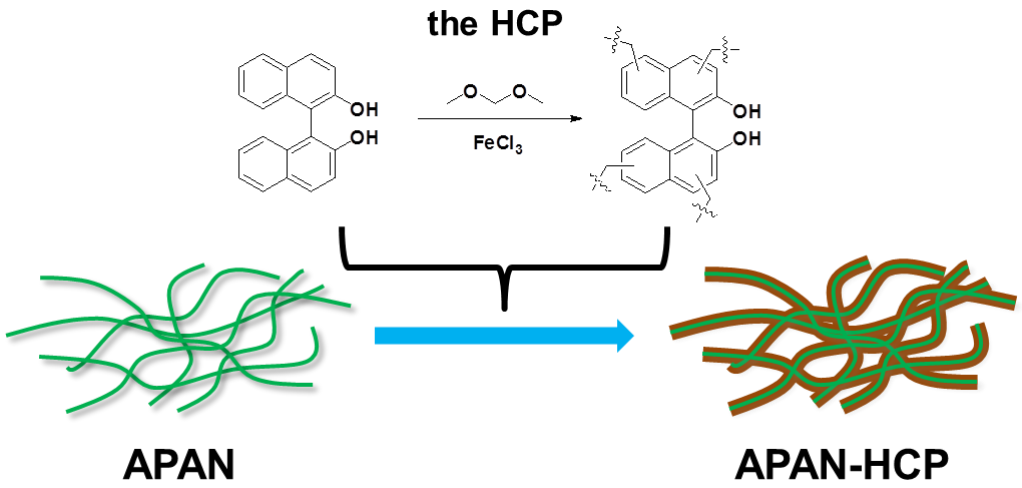

Scheme III-1. Schematic illustration of preparation of the HCP-based microporous membrane.

The amination of the PAN membrane was characterized by FT-IR spectroscopy. As shown in Figure III-1, PAN shows a strong peak at 2244 cm^{-1} corresponding to the stretching vibration of nitrile groups. After amination, the intensity of nitrile peak decreased while new peaks at 1655 cm^{-1} and 1587 cm^{-1} appeared, which corresponded to the bending vibration of the N-H group and the stretching vibration of the amide groups.[27,33]

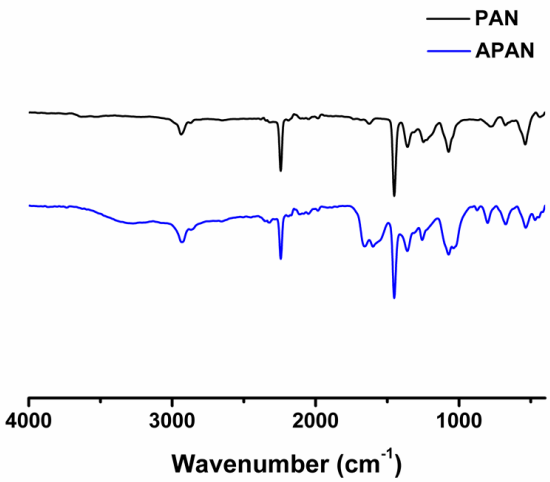

Figure III-1. FT-IR spectra of PAN and APAN.

Figure III-2 shows the microstructures of the PAN and the APAN membranes. The PAN membrane was composed of networked nanofibers having a diameter around 300 nm. The APAN membrane had the same microstructure as the PAN membrane, indicating that the amination reaction didn't change the membrane structure.

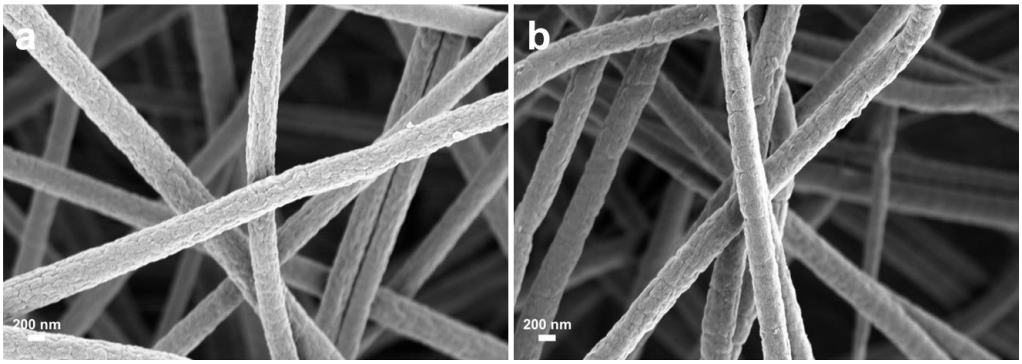

Figure III-2. SEM images of (a) the PAN membrane and (b) the APAN membrane.

A HCP coated nanofibrous membrane (APAN-HCP) was fabricated by carrying out the Friedel-Crafts reaction of 1,1'-bi-2-naphthol with dimethoxymethane in the presence of the APAN membrane. The photographs of the membranes are shown in Figure III-3. The APAN membrane had yellowish color while the PAN membrane had white color. After the Friedel-Crafts reaction, the color of the membrane turned to brown, implying the incorporation of the HCP. The shapes of the membranes were not changed by the reactions.

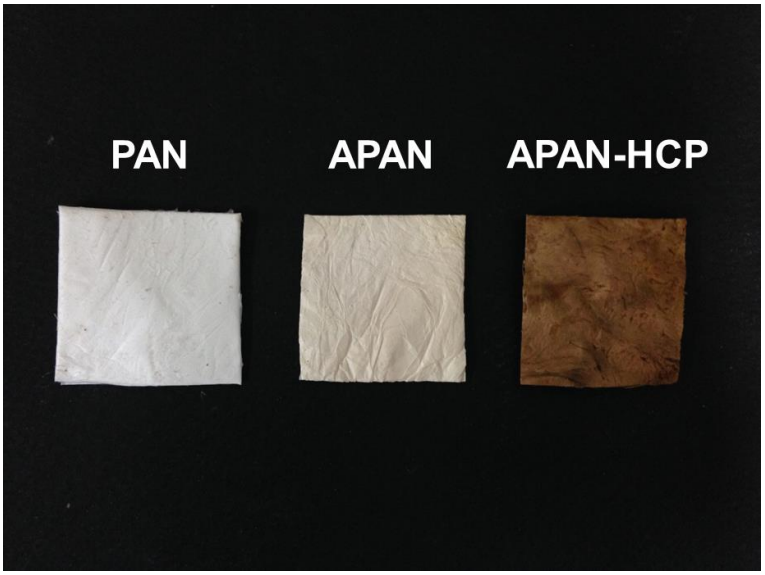

Figure III-3. The photographs of the PAN membrane, the APAN membrane, and APAN-HCP.

Figure III-4 shows the SEM images of APAN-HCP and the HCP. APAN-HCP had a nanofibrous structure having a diameter around 400 nm while the HCP was composed of nanoparticles and nanofibers. The nanofibers of APAN-HCP were smoothly coated by the HCP.[35]

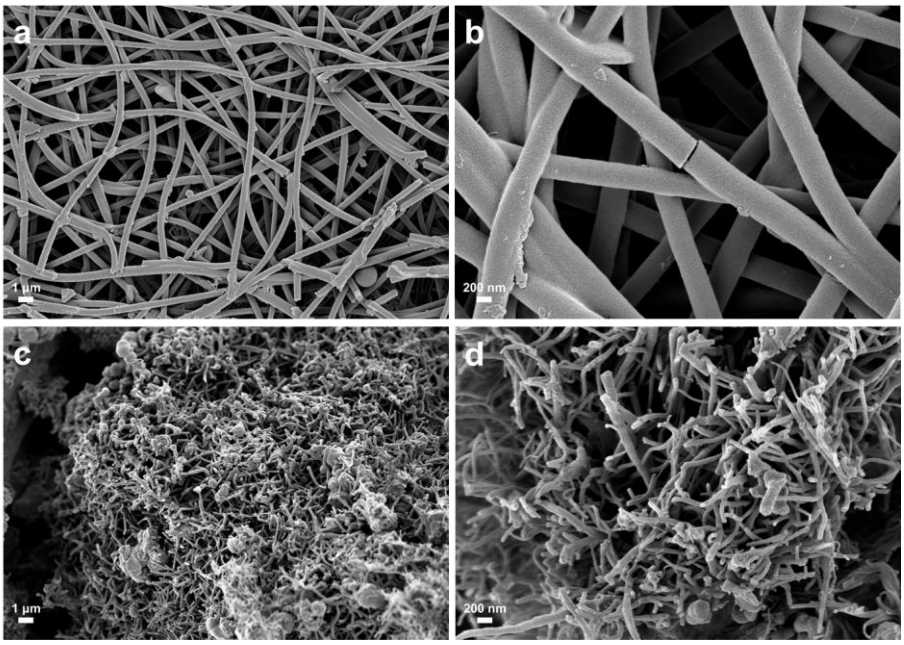

Figure III-4. SEM images of (a), (b) APAN-HCP and (c), (d) the HCP.

The chemical structures of APAN-HCP and the HCP were characterized by FT-IR and solid ^{13}C NMR spectroscopy (Figure III-5a, b). In the FT-IR spectrum, APAN-HCP showed all the peaks of APAN and the HCP. The ^{13}C NMR spectrum of the HCP showed two distinct peaks at 152 ppm and 127 ppm, which corresponded to C-OH carbons and other aromatic carbons, respectively. A broad peak at 30 ppm was assigned to aliphatic bridges between aromatic rings.[15] APAN-HCP also showed the peaks of the HCP but the peak intensity at 30 ppm was much larger than that observed in the HCP due to the presence of the aliphatic carbons in the nanofibers.

The PXRD patterns of APAN-HCP and the HCP are shown in Figure III-5c. The HCP did not have any distinct peaks, indicating its amorphous structure. APAN-HCP showed the peaks at $2\theta = 17^{o}$ and 29^{o}, which were assigned to the (100) and (101) planes of PAN.[37]

The TGA thermogram in Figure III-5d showed that APAN-HCP was thermally stable up to 300 ^{o}C. The char yields of the HCP, APAN, and APAN-HCP at 800 ^{o}C were 64.1, 39.0, and 55.4 wt%, respectively. The weight percentage of the HCP in APAN-HCP was 65.1 wt%, when based on the TGA results.[35]

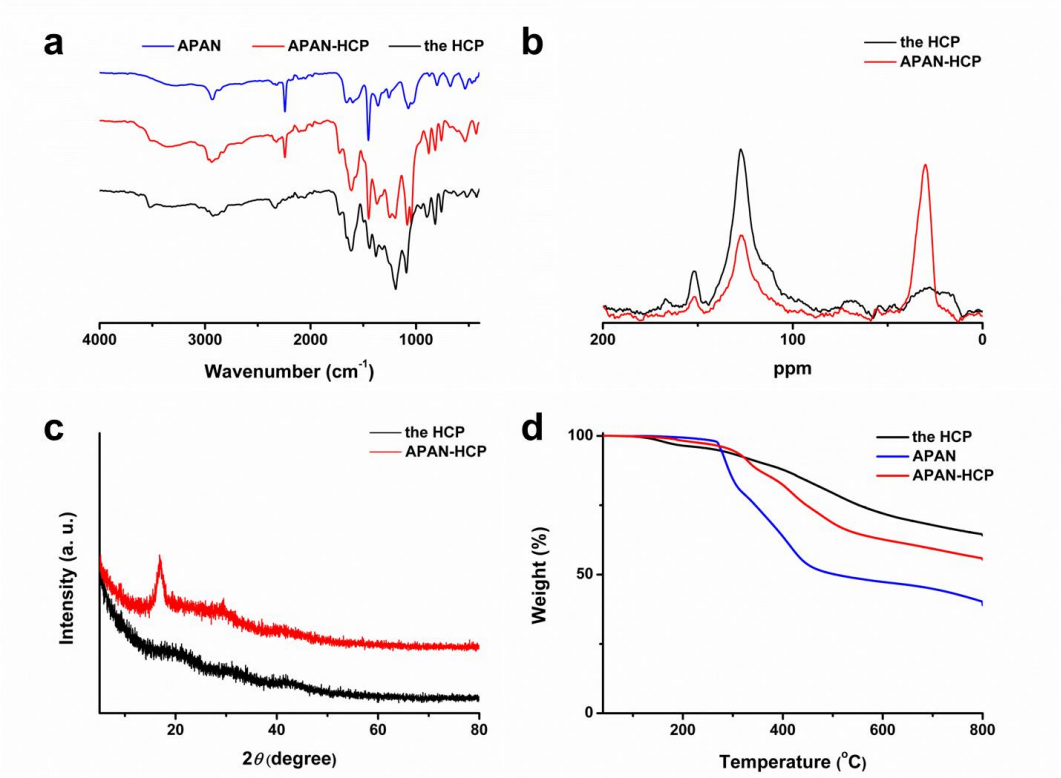

Figure III-5. (a) FT-IR spectra of APAN, APAN-HCP, and the HCP. (b) Solid state ^{13}C CP/MAS NMR spectra and (c) PXRD patterns of the HCP and APAN-HCP. (d) TGA thermograms of APAN, APAN-HCP and the HCP.

The porosities of APAN, the HCP, and APAN-HCP were investigated by N_2 adsorption-desorption analysis at 77 K (Figure III-6a). The HCP and APAN-HCP showed similar type I isotherms, which indicated the presence of micropores.[38] The surface areas of APAN, the HCP, and APAN-HCP were 19, 620, and 375 m^2g^{-1}, respectively. **A**s shown in Figure III-6b, the HCP and

APAN-HCP had similar non-local density functional theory (NLDFT) pore size distribution patterns, suggesting that the pore structure of the HCP was not significantly influenced by the reaction conditions.[35]

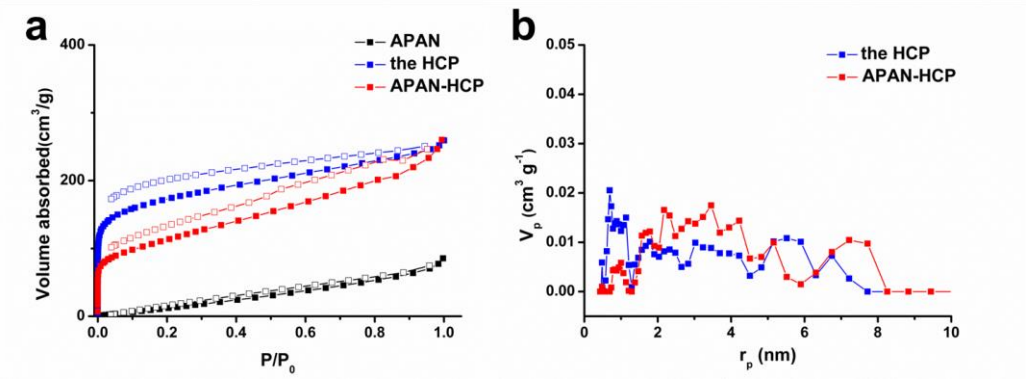

Figure III-6. (a) N_2 adsorption-desorption isotherms of APAN, the HCP, and APAN-HCP. (b) NLDFT pore size distributions of the HCP and APAN-HCP.

To investigate the effect of amine groups on the HCP growth at the nanofiber surface, a HCP-based microporous membrane (PAN-HCP) was prepared using the PAN membrane as a substrate instead of the APAN membrane. Compared with APAN-HCP, PAN-HCP had a very thin layer of the HCP on the surface of the nanofiber (Figure III-7a). The BET surface area of PAN-HCP was 108 m^2g^{-1}, which was much lower than that of APAN-HCP (Figure III-7b). These results suggested that the introduction of amino groups

onto the nanofibers significantly contributed to the even growth of the HCP on the nanofiber surface through their favorable interactions with the catalyst and the monomer.[35]

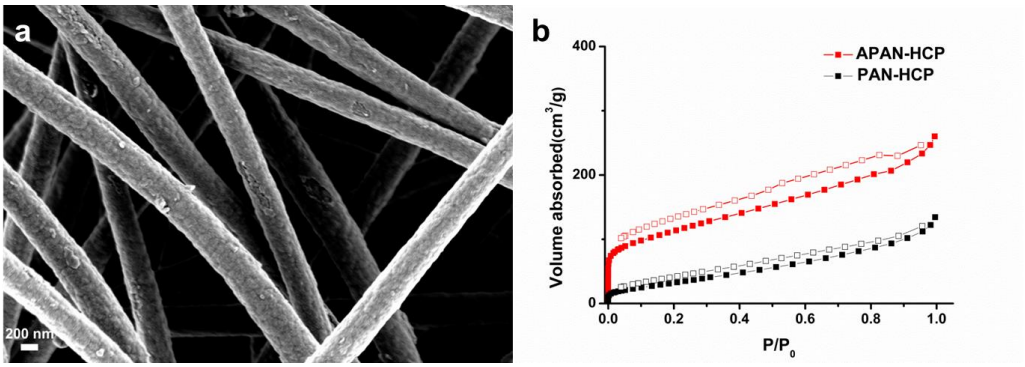

Figure III-7. (a) SEM image of PAN-HCP. (b) Comparison of N_2 adsorption-desorption isotherms of APAN-HCP and PAN-HCP.

APAN-HCP maintained the mechanical strength and flexibility of the APAN membrane (Figure III-8a). The mechanical properties of the APAN membrane and APAN-HCP were measured by the tensile tests (Figure III-8b, c). The ultimate tensile strength of APAN-HCP was slightly higher than that of the APAN membrane, while the ultimate strain of APAN-HCP was lower than that of the APAN membrane. This result indicated the stiffening of the membrane, probably due to the formation of the interfiber bonding caused by the growth of the HCP.[39-41] APAN-HCP could be easily cut into a desired shape using a

knife or a scissor.

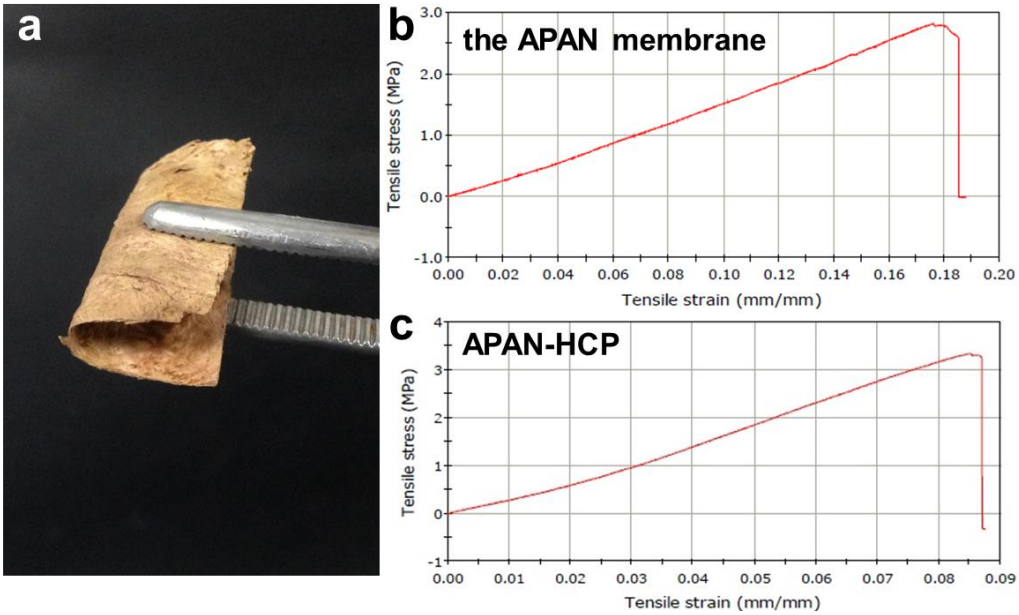

Figure III-8. (a) Photograph of the bent APAN-HCP. Tensile stress-strain curves of (b) the APAN membrane and (c) APAN-HCP.

III-3-2. Fabrication of a Pd-Containing Microporous Catalytic Membrane and Its Catalytic Ability

The microporous catalytic membrane was prepared via in-situ growth of Pd nanoparticles inside APAN-HCP (APAN-HCP-Pd). Briefly, $PdCl_2$ was first adsorbed to APAN-HCP. Pd^{2+} ion could be immobilized by 1,1'-bi-2-naphthol

units of the HCP.[29] The reduction of Pd^{2+} ions was performed by immersing the membrane in an aqueous $NaBH_4$ solution. As shown in the SEM images, the fibrous structure of the membrane was not significantly changed after the reduction reaction (Figure III-9a). The TEM analysis of APAN-HCP-Pd clearly showed the formation of Pd nanoparticles (Figure III-9b). The EDS elemental mapping indicated that Pd species were homogeneously distributed on the nanofibers (Figure III-9c). In the XPS analysis of APAN-HCP-Pd, two peaks appeared at 336.1 and 341.4 eV, corresponding to Pd $3d_{5/2}$ and Pd $3d_{3/2}$ binding energies of Pd(0) (Figure III-9d).[42] The amount of Pd species in the catalytic membrane was 6.90 wt%, when calculated by ICP-MS analysis.

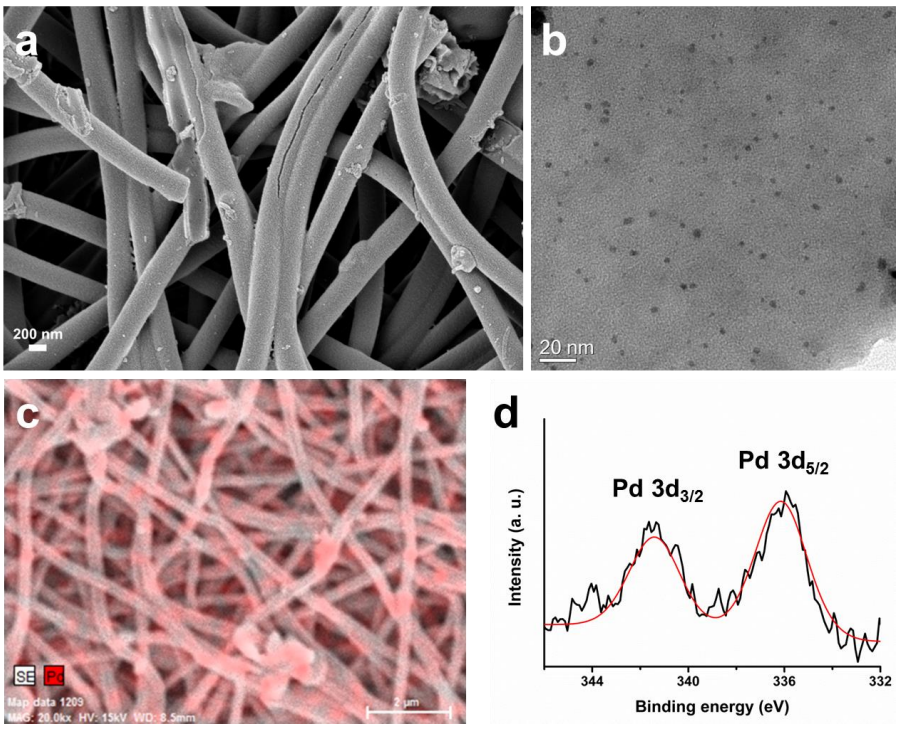

Figure III-9. (a) SEM image and (b) TEM image of APAN-HCP-Pd. (c) EDS mapping of Pd for APAN-HCP-Pd. (d) High-resolution XPS spectrum of Pd3d region of APAN-HCP-Pd.

The catalytic ability of APAN-HCP-Pd was evaluated in the reduction of 4-NP. APAN-HCP-Pd having a circular shape with a diameter of 55 mm was placed in the Buchner funnel with a filter paper as the support. And the 4-nitrophenolate aqueous solution (1 * 10^{-4} M, 100 mL) was passed under vacuum through APAN-HCP-Pd. The calculated flow rate of the solution was

0.56 mL sec^{-1}. Since APAN-HCP-Pd had a hierarchical pore structure, the solution was rapidly passed through APAN-HCP-Pd.[43,44]

Figure III-10a shows the UV absorption spectra of the 4-nitrophenolate solution measured after the several repeated catalytic reactions with APAN-HCP-Pd. The absorption peak of the 4-nitrophenolate solution at 400 nm significantly decreased after it was passed through the membrane while the peak at 298 nm increased, indicating the reduction of 4-NP to 4-aminophenol.[43,45] The conversion yields were 68.0 and 95.1 % when two and six cycles of the reaction were performed, respectively. APAN-HCP-Pd maintained its original structure and flexibility during many cycles of the reaction. The catalytic activity of APAN-HCP-Pd was slightly decreased after two sets of six cycles of the reaction as shown in Figure III-10b.

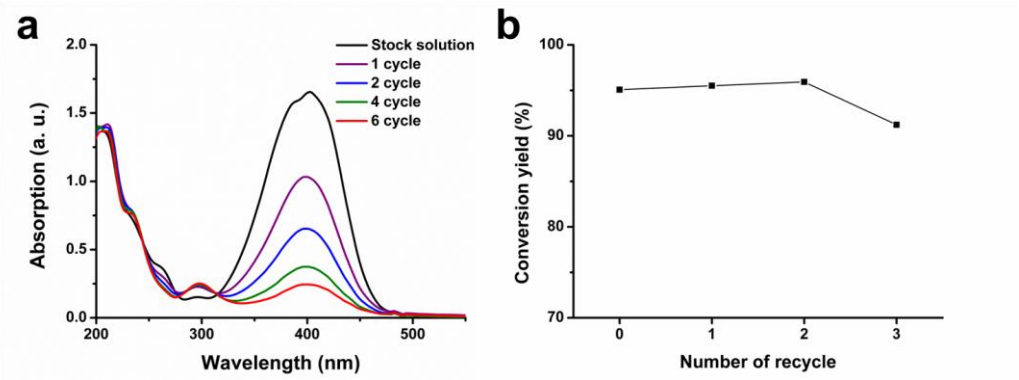

Figure III-10. (a) UV-Vis spectra of the aqueous 4-nitrophenolate solution (initial concentration = 1 x 10^{-4} M) measured during the filtration process with APAN-HCP-Pd. (b) Change in the 4-NP conversion efficiency of APAN-HCP-Pd during recycling (1 set = six filtration cycles).

III-4. Conclusions

In summary, a microporous catalytic membrane, APAN-HCP-Pd, was fabricated using an electrospun APAN membrane as a substrate. Friedel-Crafts reaction of 1,1'-bi-2-naphthol with dimethoxymethane in the presence of the APAN membrane produced a hierarchically porous membrane, where the APAN nanofibers were uniformly coated with the microporous HCP. The HCP-based nanofibrous membrane had microporosity, mechanical stability, and flexibility. Pd nanoparticles were successfully immobilized inside the HCP-

based membrane by the in-situ reduction of Pd^{2+} ions. APAN-HCP-Pd showed a good catalytic ability in the reduction of 4-NP as a membrane catalyst. APAN-HCP-Pd had a potential use for flow-through catalytic membrane reactions.

III-5. References

1. Westermann, T.; Melin, T. *Chem. Eng. Process.* **2009**, *48*, 17-28.
2. Iglesias, O; Rivero, M. J.; Urtiaga, A. M.; Ortiz, I. *Chem. Eng. J.* **2016**, *305*, 136-148.
3. Gu, Y.; Favier, I.; Pradel, C.; Gin, D. L.; Lahitte, J-. F.; Noble, R. D.; Gómez, M.; Remigy, J-. C. *J. Membrane Sci.* **2015**, *492*, 331-339.
4. Wang, Z.; Chen, X.; Li, K.; Bi, S.; Wu, C.; Chen, L. *J. Membrane Sci.* **2015**, *496*, 95-107.
5. Armor, J. N. *J. Membrane Sci.* **1998**, *147*, 217-233.
6. Meng, L.; Tsuru, T. *Catal. Today* **2016**, *268*, 3-11.
7. Kim, S. -J.; Tan, S.; Claure, M. T.; Gil, L. B.; More, K. L.; Liu, Y.; Moore, J. S.; Dixit, R. S.; Pendergast, Jr. J. G.;, Sholl, D. S.; Jones, C. W.; Nair, S. *ACS Appl. Mater. Interfaces* **2016**, *8*, 24671-24681.
8. Athanasekou, C. P.; Moustakas, N. G.; Morales-Torres, S.; Pastrana-Martínez, L. M.; Figueiredo, J. L.; Faria, J. L.; Silva, A. M. T.; Dona-

Rodriguez, J. M.; Romanos, G. E.; Falaras, P. *Appl. Catal. B-Environ.* **2015**, *178*, 12-19.

9. Zhou, K. -G.; McManus, D.; Prestat, E.; Zhong, X.; Shin, Y.; Zhang, H. -L.; Haigh, S. J.; Casiraghi, C. *J. Mater. Chem. A* **2016**, *4*, 11666-11671.
10. Moschetta, E. G.; Negretti, S.; Chepiga, K. M.; Brunelli, N. A.; Labreche, Y.; Feng, Y.; Rezaei, F.; Lively, R. P.; Koros, W. J.; Davies, H. M. L; Jones, C. W. *Angew. Chem. Int. Ed.* **2015**, *54*, 6470-6474.
11. Ozdemir, S. S.; Buonomenna, M. G.; Drioli, E. *Appl. Catal. A-Gen.* **2006**, *307*, 167-183.
12. Mendes, A.; Sousa, J. M. *Catal. Today* **2003**, *82*, 241-254.
13. Xu, S.; Luo, Y.; Tan, B. *Macromol. Rapid Commun.* **2013**, *34*, 471-484.
14. Li, B.; Guan, Z.; Wang, W.; Yang, X.; Hu, J.; Tan, B.; Li, T. *Adv. Mater.* **2012**, *24*, 3390-3395.
15. Wang, J.; Sng, W.; Yi, G.; Zhang, Y. *Chem. Commun.* **2015**, *51*, 12076-12079.
16. Zhang, A.; Gao, H.; Li, W.; Bai, H.; Wu, S.; Zeng, Y.; Cui, W.; Zhou, X.; Li, L. *Polymer* **2016**, *101*, 388-394.
17. Li, H.; Meng, B.; Chai, S-. H.; Liu, H.; Dai, S. *Chem. Sci.*, **2016**, *7*, 905-909.
18. Dou, Z.; Xu, L.; Zhi, Y.; Zhang, Y.; Xia, H.; Mu, Y.; Liu, X. *Chem. Eur.*

J. **2016**, *22*, 9919-9922.

19. Mondal, J.; Kundu, S. K.; Ng, W. K. H.; Singuru, R.; Borah, P.; Hirao, H.; Zhao, Y.; Bhaumik, A. *Chem. Eur. J.* **2015**, *21*, 19016-19027.
20. Puthiaraj, P.; Ahn, W. -S. *Catal. Sci. Technol.* **2016**, *6*, 1701-1709
21. Chinnappan, A.; Chung, W. -J.; Kim, H. *J. Mater. Chem. A* **2015**, *3*, 22960-22968.
22. Greiner, A.; Wendorff, J. H. *Angew. Chem. Int. Ed.* **2007**, *46*, 5670-5703.
23. Thavasi, V.; Singh, G.; Ramakrishna, S. *Energy Environ. Sci.* **2008**, *1*, 205-221.
24. Yan, J.; Huang, Y.; Miao, Y. -E.; Tjiu, W. W.; Liu, T. *J. Hazard. Mater.* **2015**, *283*, 730-739.
25. Wu, J.; Yang, H. *ACS Catal.* **2014**, *4*, 144-151.
26. Zhang, Y.; Yuan, S.; Feng, X.; Li, H.; Zhou, J.; Wang, B. *J. Am. Chem. Soc.* **2016**, *138*, 5785-5788.
27. Zhang, J.; Xue, Q.; Pan, X.; Jin, Y.; Lu, W.; Ding, D.; Guo, Q. *Chem. Eng. J.* **2017**, *307*, 643-649.
28. Dawson, R.; Stevens, L. A.; Drage, T. C.; Snape, C. E.; Smith, M. W.; Adams, D. J.; Cooper, A. I. *J. Am. Chem. Soc.* **2012**, *134*, 10741-10744.
29. Griffith, W. P.; Nogueira, H. I. S.; White, A. J. P.; Williams, D. J.

Polyhedron **1997**, *16*, 1323-1329.

30. Neghlani, P. K.; Rafizadeh, M.; Taromi, F. A. *J. Hazard. Mater.* **2011**, *186*, 182-189.
31. Liu, Q.; Zhong, L. -B.; Zhao, Q. -B.; Frear, C.; Zheng, Y. -M. *ACS Appl. Mater. Interfaces* **2015**, *7*, 14573-14583.
32. Zhang, B. W.; Fischer, K.; Bieniek, D.; Kettrup, A. *React. Polym.* **1994**, *24*, 49-58.
33. Deng, S.; Bai, R.; Chen, J. P. *Langmuir* **2003**, *19*, 5058-5064.
34. Kiani G. R.; Sheikhloie, H.; Arsalani, N. *Desalination* **2011**, *269*, 266-270.
35. Kim, J. G.; Choi, T. J.; Chang, J. Y. *Chem. Eng. J.* **2016**, *306*, 242-250.
36. Zhang, L.; Wang, K.; Qian, X.; Liu, H.; Shi. Z. *ACS Appl. Mater. Interfaces* **2013**, *5*, 2761-2766.
37. Zhao, W.; Lu, Y.; Jiang, J.; Hu. L.; Zhou, L. *RSC Adv.* **2015**, *5*, 23508-23518.
38. Sing, K.S.W.; Everett, D.H.; Haul, R.A.W.; Moscou, L.; Pierotti, R.A.; Rouquérol, J.; Siemieniewska, T. *Pure Appl. Chem.* **1985**, *57*, 603-619.
39. Choi, S. -S. *J. Mater. Sci.* **2004**, *39*, 1511-1513.
40. Destaye, A. G.; Lin, C. -K.; Lee, C. -K. *ACS Appl. Mater. Interfaces* **2013**, *5*, 4745-4752.

41. Si, Y.; Yu, J.; Tang, X.; Ge, J.; Ding, B. *Nat. Commun.* **2014**, *5*, 5802.

42. Qian, H.; He, Q.; Zheng, J.; Li, S.; Zhang, S. *Polymer* **2014**, *55*, 550-555.

43. Wang, R.; Liu, Y.; Li, B.; Hsiao, B. S.; Chu, B. *J. Membrane Sci.* **2012**, *392-393*, 167-174.

44. Raza, A.; Ding, B.; Zainab, G.; El-Newehy, M.; Al-Deyab, S. S.; Yu, J. *J. Mater. Chem. A* **2014**, *2*, 10137-10145.

45. Niu, T.; Xu, J.; Xiao, W.; Huang, J. *RSC Adv.*, **2014**, *4*, 4901-4904.

Chapter IV.

Preparation of a Sulfur-Functionalized Microporous Polymer Sponge and In Situ Growth of Silver Nanoparticles: a Compressible Monolithic Catalyst

IV-1. Introduction

Porous materials with high surface areas are widely used for heterogeneous catalysis as supports. The main advantages of a heterogeneous catalyst over its homogeneous analogue are the easy separation of the catalyst from a reaction mixture and its tolerance in harsh operating conditions. The chemical and morphological structures of the supporting materials have a significant influence on the performance of the heterogeneous catalysts through their interactions with catalytically active species.[1] Typical catalyst supports are porous materials, including a variety of carbon materials and oxides such as alumina and silica. Organic polymers with low surface areas have been used in catalytic reactions, where reagents or catalysts are immobilized to the polymer backbones.[2]

Recent advances on microporous organic polymers (MOPs) provide new opportunities to develop efficient heterogeneous catalysts. MOPs have characteristics of high surface areas, low density and flexibility in the architectural design.[3,4] As heterogeneous catalyst supports, MOPs have the following significant advantage over porous carbon and oxide materials: MOPs are easily functionalized by the post-modifications and thereby the interactions between the active species and the supports can be adjusted,[4-6] resulting in high catalytic activity and recyclability.

A majority of MOPs are constructed by coupling reactions of multifunctional monomers.[5-12] They have highly cross-linked structures and usually obtained as infusible powders, which seriously restricts their processability and use.[13] Several methods have been studied to fabricate shape controlled MOPs like spherical nanoparticles[14] and films.[11.15,16] Recently we reported sponge-like monolithic microporous polymers.[17] Spongy polymeric materials have useful properties, such as low density, high porosity and compressibility.[17-19] These attractive features would allow easy uptake and release of chemicals.

Herein, we report a monolithic catalyst based on a MOP sponge. The MOP sponge had a three-dimensional network structure composed of tubular polymer fibers. It showed reversible compressibility and hierarchical porosity. The sponge was functionalized with sulfur groups and then decorated with silver nanoparticles. The activity of the monolithic catalyst was evaluated in the reduction reaction of 4-nitrophenol. The acceleration of the reaction rate was achieved by taking advantage of the compressible property of the catalyst.

IV-2. Experimental

Materials. 1,4-Diiodotetrafluorobenzene (98 %), copper iodide (CuI), silver nitrate (99 %) and 4-nitrophenol (4-NP) (99 %) were purchased from Sigma-Aldrich. 1,3,5-Triethynylbenzene (98 %), bis(triphenylphosphine)palladium(II) dichloride ($Pd(PPh_3)_2Cl_2$) (98 %), 1,3-propanedithiol (99 %) and sodium borohydride ($NaBH_4$) (95 %) were purchased from Tokyo Chemical Industry. Azobisisobutyronitrile (AIBN) was obtained from Junsei Chemical. AIBN was recrystallized by methanol, and other chemicals were used without further purification.

Preparation of a Microporous Polymer Sponge. 1,3,5-Triethynylbenzene (225 mg, 1.5 mmol) and 1,4-diiodotetrafluorobenzene (603 mg, 1.5 mmol) were dissolved in a cosolvent of toluene (9.0 mL) and triethylamine (4.5 mL). $Pd(PPh_3)_2Cl_2$ (30.0 mg, 37.0 μmol) and CuI (9.0 mg, 47.2 μmol) were added to the solution and dispersed by sonication. The mixture was moved to the 10 mL vial and heated at 60 ^oC for 24 h without stirring under aerobic conditions. A resultant polymer was washed with THF and ethanol and was Soxhlet extracted using methanol. After drying in vacuo at room temperature, the MOP sponge was obtained as a monolith.

Sulfur-Functionalized MOP Sponge (S-MOPS). A piece of MOP sponge (100 mg) was immersed in 25 mL of toluene and degassed by bubbling with nitrogen. 1,3-Propanedithiol (218 mg, 2.0 mmol) and AIBN (330 mg, 2.0 mmol) were added to the mixture. After stirring for 1 h at room temperature, the thiol-yne reaction was performed at 90 ^{o}C for 24 h under nitrogen. The resulting functionalized polymer was washed with THF and ethanol and dried in vacuo at room temperature.

Silver Decorated MOP Sponge as a Heterogeneous Catalyst (S-MOPS-Ag). Silver nitrate (140 mg, 0.82 mmol) was dissolved in a mixture of H_2O (15 mL) and ethanol (30 mL). S-MOPS (140 mg) was put in the solution and was compressed and released 100 times to uptake Ag^+ ions. The sponge was removed from the silver nitrate solution and squeezed to get rid of the excess solution. The Ag^+ ion containing-sponge was immediately immersed in a solution of $NaBH_4$ (308 mg, 8.24 mmol) in a mixture of H_2O (15 mL) and ethanol (30 mL). The sponge was compressed and released 100 times and stirred for 3 h. The MOP sponge-Ag composite was washed with H_2O and ethanol and dried in vacuo at room temperature.

Catalytic Reduction Reaction of 4-Nitrophenol by S-MOPS-Ag. A piece

of S-MOPS-Ag (60.0 mg) was immersed in ethanol for 1 min and was squeezed to remove ethanol. The ethanol wetted-sponge was then immersed in H_2O. After stirring for 10 min, the sponge was squeezed to remove H_2O. A reaction solution was prepared by mixing aqueous solutions of 4-NP (0.2 mM, 15 mL) and $NaBH_4$ (80.0 mM, 15 mL). Subsequently, the S-MOPS-Ag was added to the solution, and manually compressed and released with a rate of 3 s for the cycle. The reduction of 4-NP was monitored by UV-Vis absorption spectroscopy. For comparison, the reduction experiments without stirring (static condition) and with stirring were also carried out under the same conditions except that the sponge was not compressed. The sponge was reused after washing with H_2O and ethanol and drying.

Instrumental Characterization. Scanning electron microscopy (SEM) images were observed by a Carl Zeiss SUPRA 55VP. Transmission electron microscopy (TEM) images were obtained using a JEM-2100 operating at 200 kV. TEM samples were prepared by dropping a dispersion of the polymers in THF on a carbon-coated copper TEM grid. Energy-dispersive X-ray spectroscopy (EDS) elemental maps were measured by an Oxford instrument X-MaxN detector and analysed with an AZtecEnergy EDS analyzer. Solid-state ^{13}C NMR spectra were obtained on a Bruker Avance 400WB spectrometer (100

MHz) equipped with a CP-MAS probe. Elemental analyses were performed on a Flash EA 1112 elemental analyzer. Powder X-ray diffraction (PXRD) patterns were recorded using a New D8 Advance (Cu K_α radiation, λ = 1.54 Å). Thermogravimetric analyses (TGA) were performed using a TA modulated TGA2050 with a heating rate of 10 ℃/min under nitrogen. FT-IR spectra were observed by a PERKIN ELMER Spectrum GX I spectrometer using KBr pellets. The compression tests were performed by an Instron 5543 universal testing machine. A cylindrical sponge having a diameter of 18 mm and height of 13 mm was used for the measurement. The strain-stress curves were recorded at a strain rate of 3 mm min-1. A 10 cycles of the loading-unloading test was carried out at a strain rate of 30 mm min^{-1}. N_2 adsorption-desorption isotherms were obtained by a Belsorp-Max (BEL Japan, Inc.) apparatus. Inductively coupled plasma mass spectrometry (ICP-MS) was performed using a Varian 820-MS to calculate a weight percentage of Ag in the composite. Ag nanoparticles were dissolved in strong nitric acid before measurement. X-ray photoelectron spectroscopy (XPS) was measured by a KRATOA AXIS-His spectrometer equipped with a Mg K_α X-ray source. UV-Vis spectra were recorded with a Sinco S-3150 spectrometer.

IV-3. Results and Discussion

IV-3-1. Synthesis and Characterization of a MOP Sponge

A monolithic MOP sponge was synthesized via Sonogashira-Hagihara coupling reaction between 1,4-diiodotetrafluorobenzene and 1,3,5-triethynylbenzene (Scheme IV-1). The reaction was performed at 60 ^{o}C without stirring in a co-solvent of toluene and TEA (2:1, v/v). The reaction mixture turned into a viscose gel in 60 min, and a monolithic MOP was isolated after 24 h. The MOP could be prepared in various shapes and sizes using a reaction vessel as a mold. For example, a cylindrical MOP was synthesized in a 10 mL vial as shown in Scheme IV-1. The MOP was light with an average density of 47.0 mg cm^{-3} and maintained its original shape even after washing and drying. The ^{13}C solid state NMR spectrum showed all the carbon peaks from the expected polymer structure. The peaks from aromatic carbons appeared at 143, 132, 120 and 102 ppm, and the carbon peaks from acetylene groups showed up at 98 and 77 ppm (Figure IV-1).

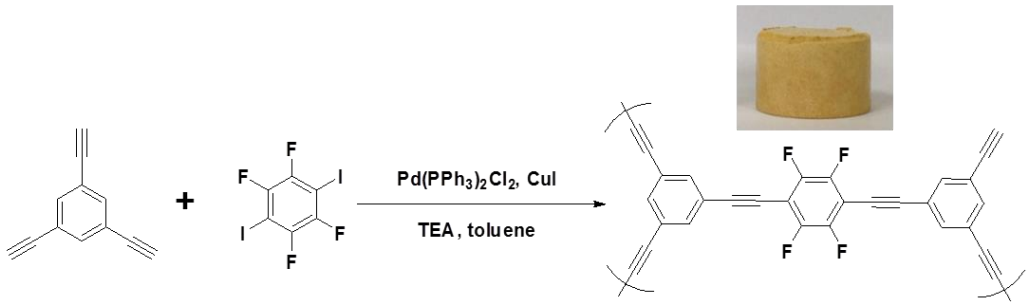

Scheme IV-1. Reaction scheme for the synthesis of the MOP sponge and its photo image.

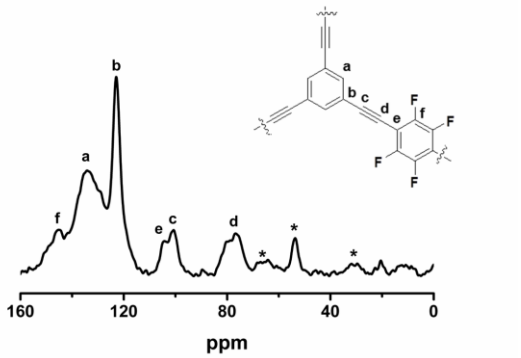

Figure IV-1. Solid state ^{13}C CP/MAS NMR spectrum of the MOP sponge.

Figure IV-2 shows compressive stress-strain test results for the MOP sponge at the set strain maxima of 20 and 40 %. The MOP sponge had reversibly compressible properties. The stress-strain curve patterns were similar to those of porous foam-like materials, which consisted of the elastic region ($\varepsilon < 15$ %)

and the plateau region (15 % < ε < 40 %).[20] After 10 loading-unloading cycles to a maximum strain of 40%, a slight decrease in the maximum stress was observed, but the deformation was recoverable upon release of the stress.

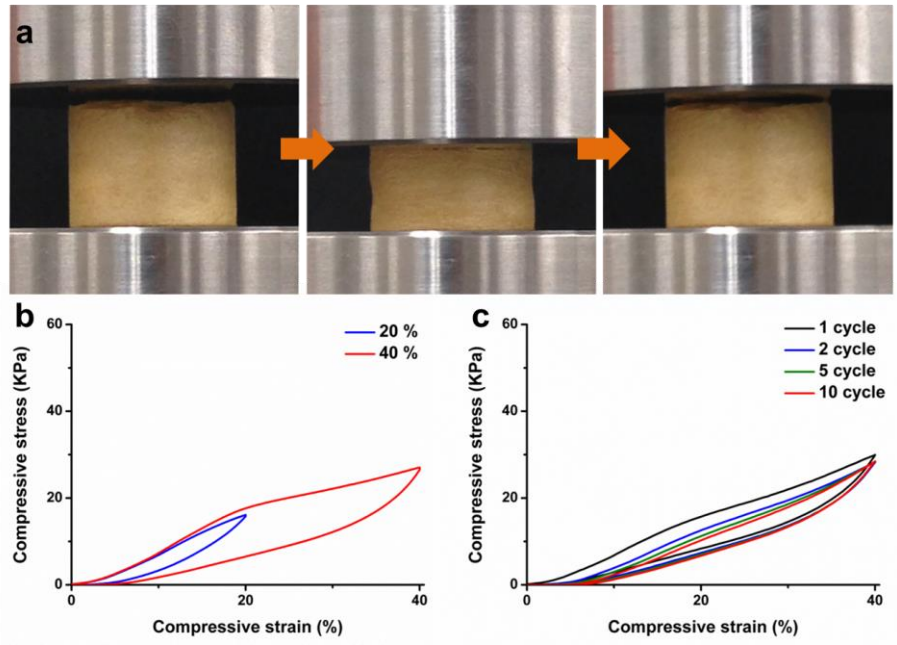

Figure IV-2. (a) Images of the MOP sponge under compression and release conditions. (b) Compressive stress-strain curves (maximum strain = 20 and 40 %) and (c) 10 cycles of loading-unloading test results of the MOP sponge (maximum strain = 40 %).

The microscopy study revealed that the monolithic and compressible properties of the MOP sponge resulted from its intriguing fibrous

microstructure (Figure IV-3). Polymer fibers with a diameter of hundreds of nanometers were found to constitute the monolith. The TEM and SEM images showed that each polymer fiber had a hollow tubular structure with open ends. The overall morphology of the MOP sponge resembled that of a carbon nanotube (CNT) sponge.[20,21] Fibrous tubular structures are usually not expected for cross-linked polymers prepared from multifunctional monomers. We presume that tubular shapes were induced by step reactions in combination with the structured self-assembly of the reactants in the Sonogashira-Hagihara coupling reaction,[22] but need further study to fully understand the mechanism. A few other examples of polymerization systems that produce tubular fibers have been reported.[22-24]

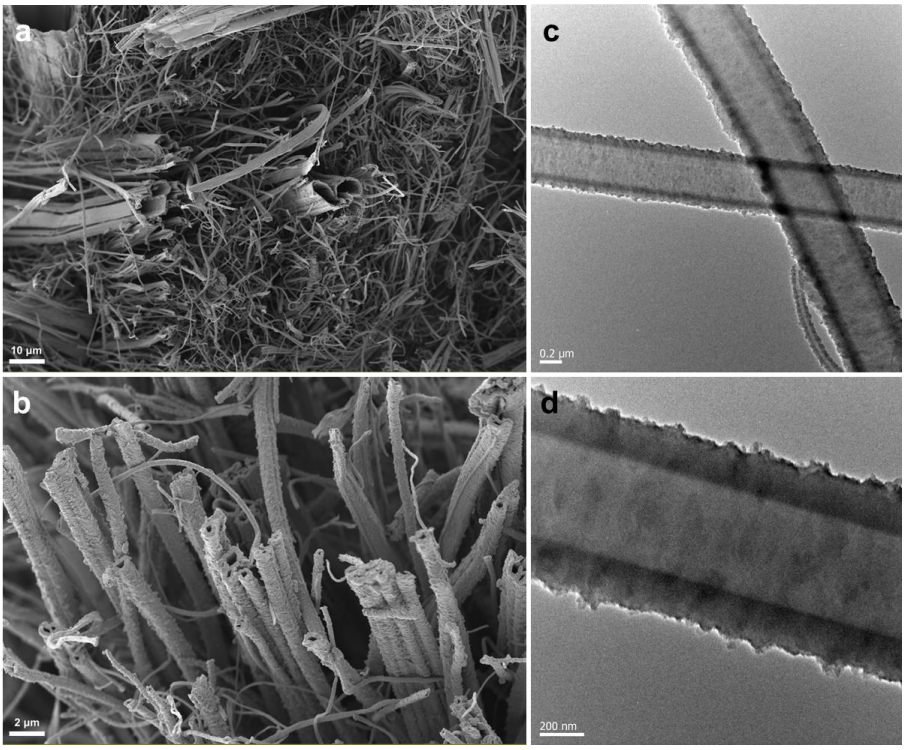

Figure IV-3. (a), (b) SEM and (c), (d) TEM images of the MOP sponge.

IV-3-2. Functionalization of a MOP Nanotube Sponge with Sulfur Groups

MOPs prepared from multifunctional monomers usually contained many reactive groups. They were functionalized by post-reactions for specific purposes such as hydrophilicity enhancement,[25] gas adsorption[26] and generation of catalytic centers.[27] The MOP sponge had disubstituted and terminal alkyne groups, which could be used for the post-modification.[25,28] The thiol-yne reaction is a coupling reaction between a thiol and an alkyne,

which proceeds in a high yield via a radical mechanism. The thiol-yne reaction of the MOP sponge was carried out with 1,3-propanedithiol using AIBN as a radical initiator to give a sulfur-functionalized MOP sponge (S-MOPS) (Scheme IV-2). Sulfur groups are well known for their high affinity to heavy metals such as silver, gold and palladium.[29,30]

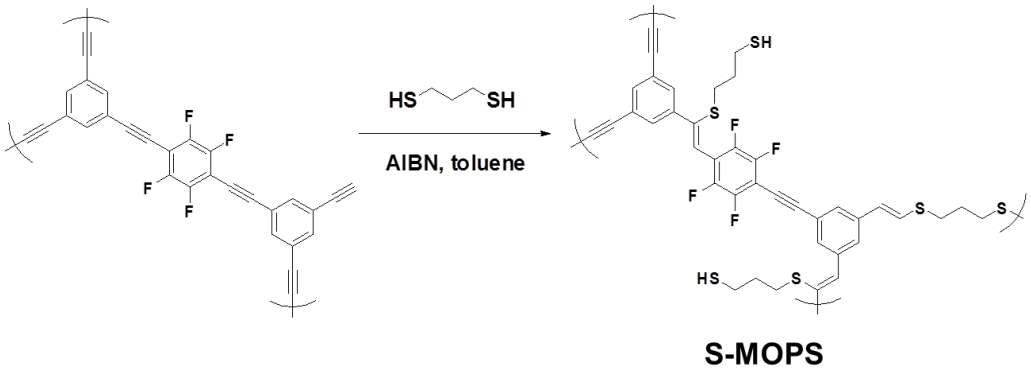

Scheme IV-2. Thiol-yne modification of the MOP sponge and a possible structure of S-MOPS.

S-MOPS maintained the monolithic shape and the entangled fibrous tubular microstructure as observed in the SEM and TEM images (Figure IV-4a, b). The EDS elemental mapping showed the homogeneous distribution of sulfur atoms on the surface of the polymer (Figure IV-4c). S-MOPS showed reversible compressibility similar to the MOP sponge (Figure IV-5), but the maximum

stress of S-MOPS at 40 % strain was slightly higher than that of the MOP sponge.

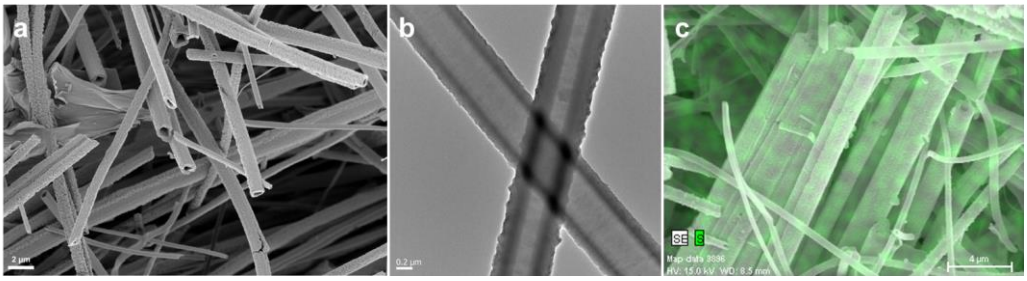

Figure IV-4. (a) SEM and (b) TEM images of S-MOPS. (c) EDS mapping of sulfur for S-MOPS.

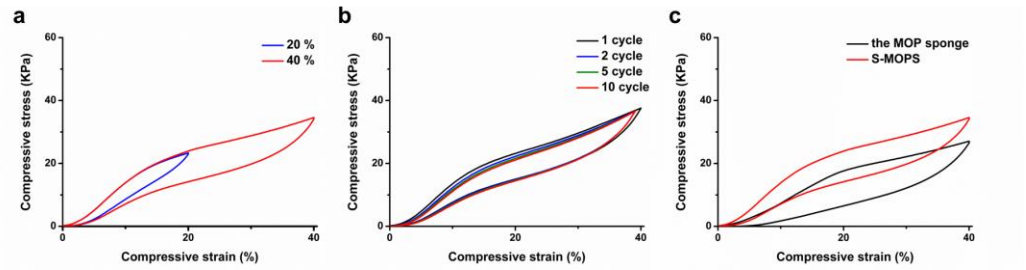

Figure IV-5. (a) Compressive stress-strain curves (maximum strain = 20 and 40 %) and (b) 10 cycles of the loading-unloading test results of S-MOPS (maximum strain = 40 %). (c) Comparison of hysteresis curves of the MOP sponge and S-MOPS at 40 %.

The structural change of the MOP sponge after the thiol-yne reaction was investigated by FT-IR and solid state ^{13}C NMR spectroscopy. In the FT-IR

spectrum of the MOP sponge, the -C≡C- band of substituted acetylene groups and the C-H band of terminal acetylene groups appeared at 2222 and 3330 cm^{-1}, respectively. After the thiol-yne reaction, the peak intensities of those bands decreased considerably.[25,28] Also, the peaks around 3000 cm^{-1} newly appeared, which corresponded to the C-H band of propyl groups (Figure IV-6a). The solid state ^{13}C NMR spectrum of S-MOPS showed the carbon peaks of propyl groups at around 30 ppm (Figure IV-6b). The elemental analysis also confirmed the presence of sulfur (14.1 wt%) (Table IV-1). All these results corroborated that the MOP sponge was successfully functionalized by the thiol-yne reaction.[25,28,31] Both the MOP sponge and S-MOPS did not have discernible crystalline peaks in the PXRD patterns (Figure IV-6c). Thermogravimetric analysis showed (Figure IV-6d) that the MOP sponge was thermally stable up to 300 ^{o}C. The degradation of S-MOPS began earlier than the MOP sponge probably due to the presence of propyl groups.[32]

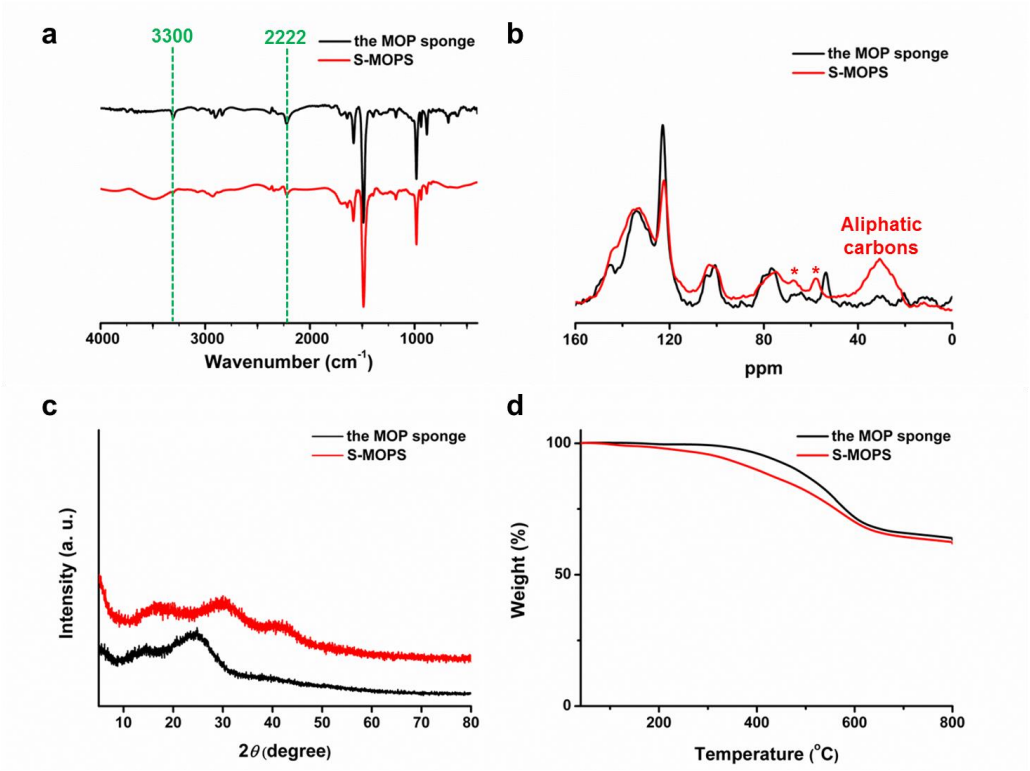

Figure IV-6. (a) FT-IR spectra, (b) Solid state ^{13}C CP/MAS NMR spectra, (c) PXRD patterns and (d) TGA thermograms of the MOP sponge and S-MOPS.

Table IV-1. Elemental compositions of the MOP sponge and S-MOPS measured by elemental analysis.

	C (wt%)	H (wt%)	S (wt%)
The MOP sponge	67.6	1.8	0
S-MOPS	66.4	2.6	14.1

The pore structures of the MOP sponge and S-MOPS were studied by N_2 adsorption-desorption analysis at 77 K (Figure IV-7a, Table IV-2). The Brunauer-Emmett-Teller (BET) surface area of the MOP sponge was 512 m^2 g^{-1}. After the thiol-yne reaction, the BET surface area of the MOP sponge was increased to 649 m^2 g^{-1}, which was unusual compared with the previous reports.[25,28] This result could be attributable to the favorable change in the pore structure to the surface area where total pore and micropore volumes increased, and an average pore size decreased by the post-reaction. NLDFT pore size analysis (Figure IV-7b) revealed that mesopores in the range of 15 - 40 nm found in the MOP sponge almost disappeared and more meso- and micropores with a size of less than 10 nm formed after the thiol-yne reaction. We presumed that the reaction of the alkyne groups of the MOP sponge with the dithiol produced a more highly crosslinked network[31-33] with an increase in the micropore volume.

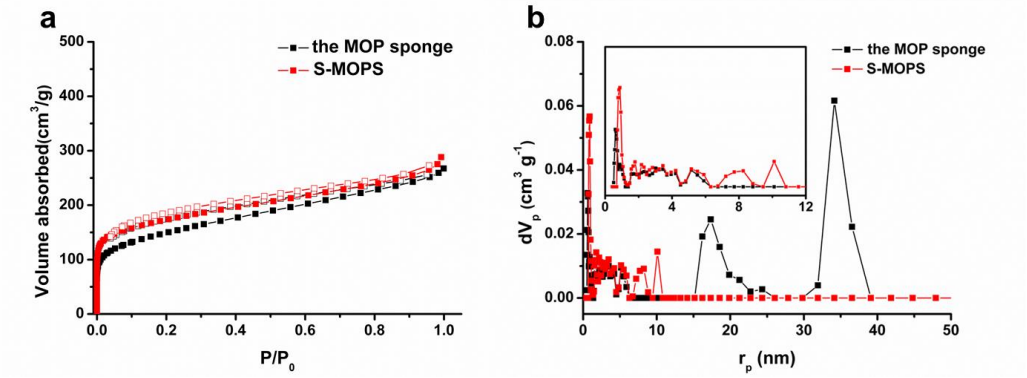

Figure IV-7. (a) N_2 adsorption-desorption isotherms measured at 77 K and (b) NLDFT pore size distributions of the MOP sponge and S-MOPS.

Table IV-2. Porosity data of the MOP sponge and S-MOPS.

	S_{BET}[a] $m^2\ g^{-1}$	S_{micro}[b] $m^2\ g^{-1}$	S_{micro}/S_{BET}	V_{total}[c] $cm^3\ g^{-1}$	V_{micro}[d] $cm^3\ g^{-1}$	V_{micro}/V_{total}	Pore size[a] nm
the MOP sponge	512	331	0.646	0.440	0.182	0.414	3.43
S-MOPS	649	487	0.750	0.472	0.235	0.498	2.91

[a]The surface area and average pore size were calculated from N_2 adsorption-desorption isotherms by the BET method. [b]The surface area from micropores was calculated by the t-plot method. [c]Pore volume at $P/P_0 = 0.99$. [d]Pore volume at $P/P_0 = 0.1$.

IV-3-3. A Silver Decorated MOP Sponge as a Heterogeneous Catalyst

A monolithic heterogeneous catalyst was prepared by using the MOP sponge as a support. The high porosity and compressibility of the MOP sponge were expected to allow rapid absorption of organic reactants,[34-36] which could increase the efficiency of the catalytic reaction. Silver was chosen as a metal catalyst, which is relatively cheap and shows excellent catalytic activity in many organic reactions.[37,38] A silver decorated MOP sponge as a heterogeneous catalyst was prepared by in-situ growth of silver nanoparticles inside the MOP sponge. Briefly, S-MOPS was immersed in a silver nitrate solution, and compressed and released repeatedly to absorb Ag^+ ions. The subsequent reduction reaction with $NaBH_4$ was carried out to produce the silver nanoparticles supported on S-MOPS (S-MOPS-Ag).

Figure IV-8a and b show the SEM and TEM images of S-MOPS-Ag, respectively. The EDS elemental mapping showed the even distribution of Ag atoms inside the MOP sponge (Figure IV-8c). The average diameter of Ag nanoparticles was 7.08 nm (Figure IV-8d).

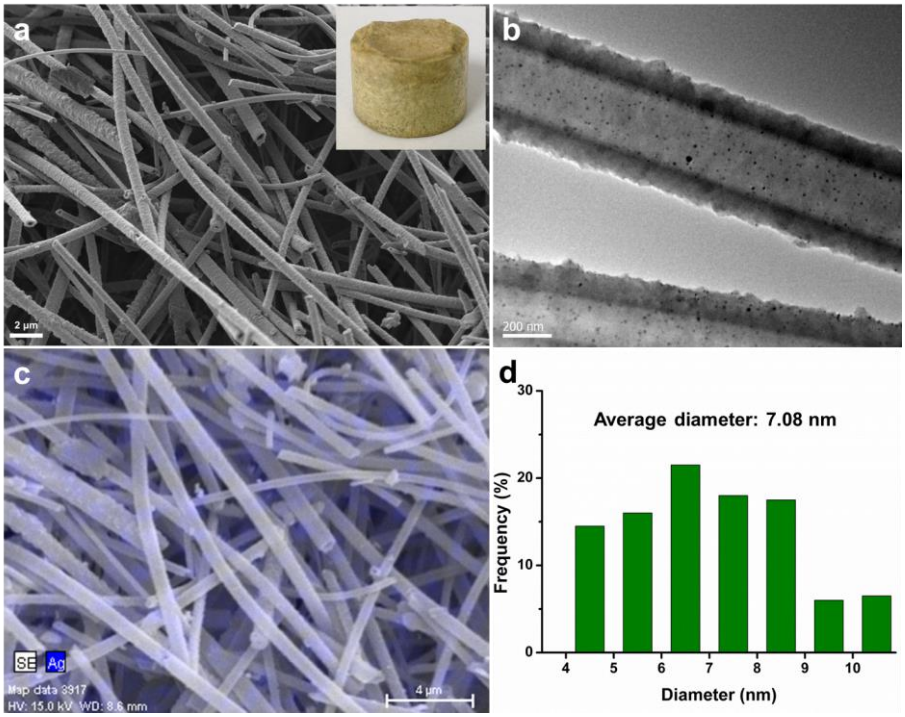

Figure IV-8. (a) SEM image and the photograph (inset) of S-MOPS-Ag. (b) TEM image and (c) EDS mapping of silver atoms for S-MOPS-Ag. (d) Diameter distribution of Ag nanoparticles inside S-MOPS-Ag.

In the PXRD analysis of S-MOPS-Ag (Figure IV-9a), four sharp diffraction peaks appeared at $2\theta = 38$, 44, 64 and 77°, which were indexed to the (111), (200), (220) and (311) planes of cubic Ag, respectively.[38,39] In the high-resolution XPS spectrum, the peaks were observed at 368 and 374 eV, corresponding to Ag $3d_{5/2}$ and Ag $3d_{3/2}$ binding energies, respectively (Figure IV-9b). These results supported that Ag^+ ions were successfully converted to

metallic Ag by the reduction reaction.[38,40] The amount of Ag nanoparticle loading inside S-MOPS-Ag was 5.39 wt% when calculated by ICP-MS analysis. S-MOPS-Ag showed similar compressive stress-strain behaviors to S-MOPS (Figure IV-10a). BET surface area of S-MOPS-Ag decreased slightly to 560 m^2 g^{-1} from 649 m^2 g^{-1} of S-MOPS (Figure IV-10b).[41]

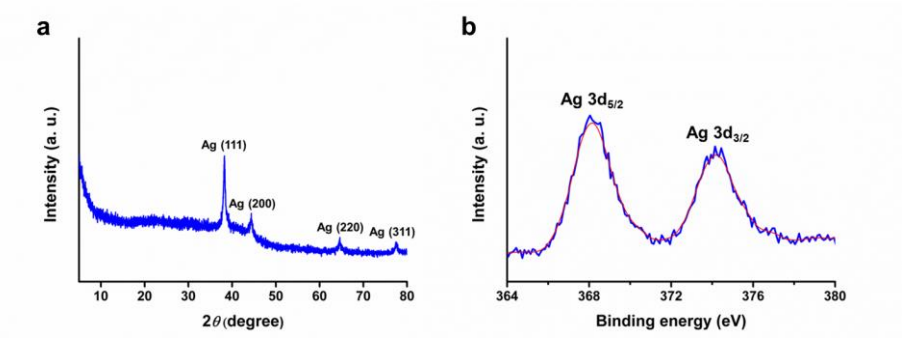

Figure IV-9. (a) PXRD pattern of S-MOPS-Ag. (b) High-resolution XPS spectrum of Ag3d region of S-MOPS-Ag.

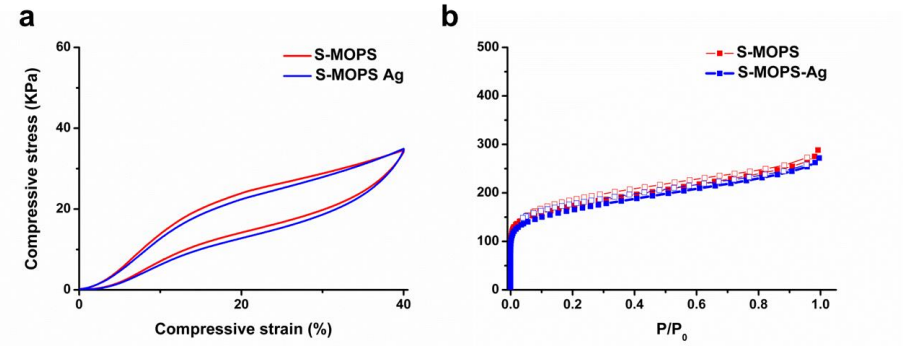

Figure IV-10. (a) Compressive stress-strain curves (maximum strain = 40%) and (b) N_2 adsorption-desorption isotherms measured at 77 K of S-MOPS and S-MOPS-Ag.

IV-3-4. Catalytic Ability Evaluation of S-MOPS-Ag for the Reduction of 4-Nitrophenol

The catalytic activity of S-MOPS-Ag was evaluated in the reduction reaction of 4-nitrophenol (4-NP) to 4-aminophenol by $NaBH_4$.[33,40,41] Because of hydrophobicity of the MOP framework, a piece of monolithic S-MOPS-Ag was first wetted with ethanol and then with water by solvent-exchange before the catalytic reaction. A reaction solution was prepared by mixing aqueous 4-NP and $NaBH_4$ solutions, which showed an absorption maximum around 400 nm due to the formation of 4-nitrophenolate.[40,41] For the catalytic reaction to proceed, S-MOPS-Ag was immersed in the reaction solution and manually compressed and released with a rate of 3 s for the cycle. The progress of the reduction reaction could be monitored by UV-Vis spectroscopy and the naked eye (Figure IV-11a, b). The absorption peak intensity of 4-nitrophenolate at 400 nm was rapidly diminished, and a new peak developed around 300 nm. After 160 compression-release cycles, the peak intensity became weak, and the initially reddish solution turned almost colorless, suggesting the near completion of the reduction reaction.[40,41] In contrast, the reaction occurred very slowly when the reduction reaction was carried out without the

compression-release process. (Figure IV-11c, d). S-MOPS alone did not catalyze the 4-NP reduction under the same experimental conditions (Figure IV-12).

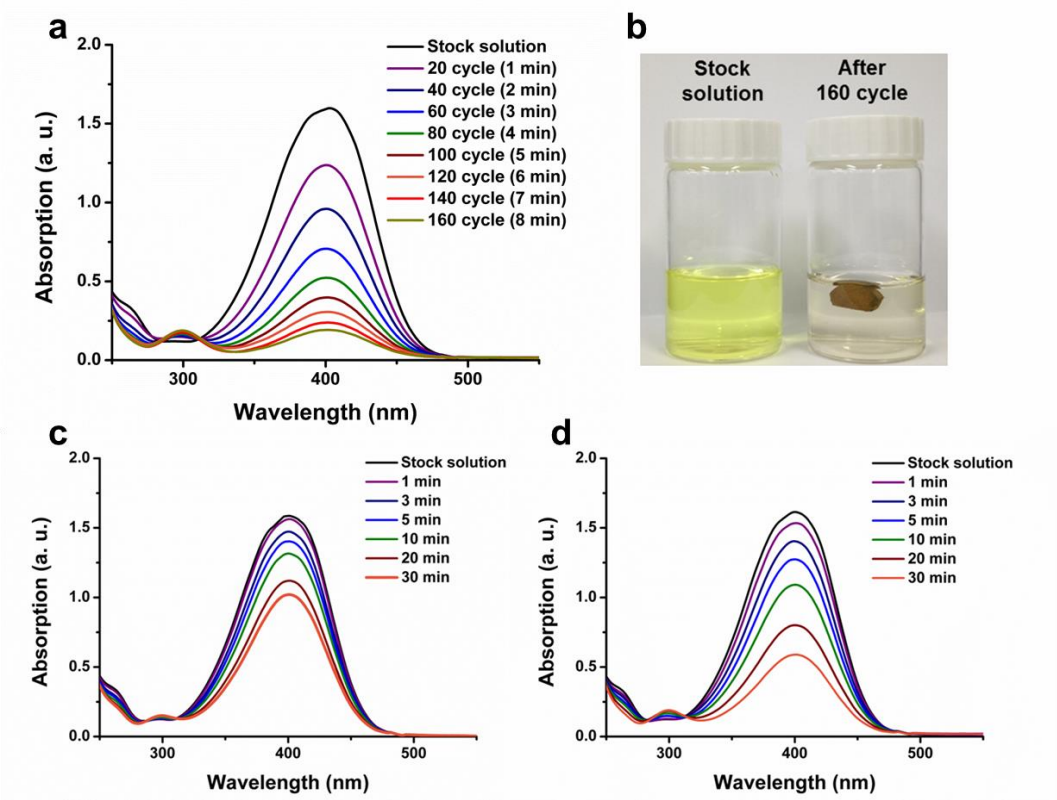

Figure IV-11. (a) UV-Vis spectra of the aqueous 4-NP solution (initial concentration = 1 x 10^{-4} M) measured during the reaction with the compression and release process. (b) Photographs of the 4-NP solution taken before and after 160 cycles of compression and release. UV-Vis spectra of the aqueous 4-NP solution (initial concentration = 1 x 10^{-4} M) measured without the compression

and release process; (c) the reaction solution was not stirred and (d) the reaction solution was stirred.

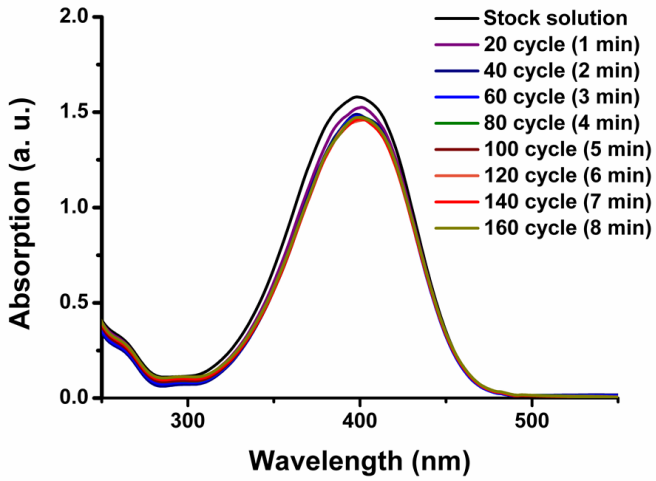

Figure IV-12. UV-Vis spectra of the aqueous 4-NP solution (initial concentration = 1 x 10^{-4} M) measured during the reaction with the repeated compression and release of S-MOPS.

Since a large excess of $NaBH_4$ was used compared with 4-NP, the pseudo first-order kinetic equation could be used to describe the overall reaction as follows:

$$\ln(C_t / C_0) = - kt \qquad (1)$$

where C_t is the concentration of 4-NP at reaction time = t and C_0 is the initial concentration.[41] All the reactions showed linear correlations between $\ln(C_t / C_0)$ and time (Figure IV-13). The apparent rate constant of the reaction with the compression-release process was 7.61×10^{-3} s^{-1}, which was much higher than those for the reactions without the compression-release process. The increase in the reaction rate came from enhanced efficiency in fluid exchange.[35,42] Through the compression-release, the reactants had more chances to contact with silver catalysts inside the MOP sponge. When S-MOPS-Ag was simply immersed in the reaction solution, the reaction rate would be governed by the slow diffusion of the reactants into the MOP sponge. S-MOPS-Ag was easily removed from the reaction mixture owing to its monolithic character and was reused after washing and drying. The 4-NP reduction efficiency of S-MOPS-Ag was maintained around 95 % after 5 cycles of the reactions (Figure IV-14).

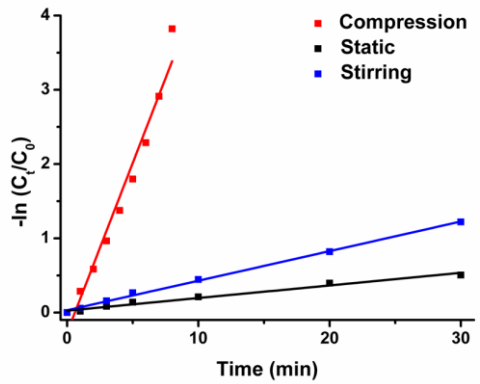

Figure IV-13. Plots of - $\ln(C_t / C_0)$ versus time during the catalytic reduction of 4-NP by S-MOPS-Ag under different reaction conditions. With the compression-release process, the apparent rates constant (k) for the reaction = 7.61 x 10^{-3} s^{-1}. Without the compression and release process, k = 2.84 x 10^{-4} s^{-1} when the reaction solution was not stirred and k = 6.64 x 10^{-4} s^{-1} when the reaction solution was stirred.

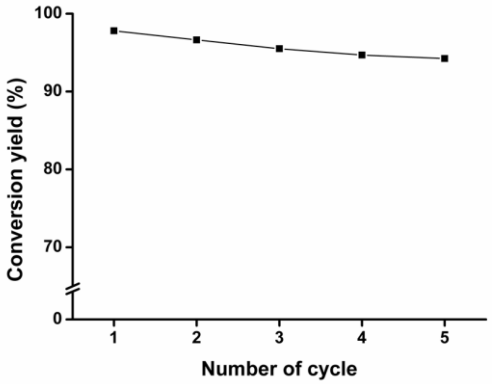

Figure IV-14. Change in the catalytic activity of S-MOPS-Ag during recycling.

IV-4. Conclusions

In conclusion, we fabricated a compressible and monolithic heterogeneous catalyst based on the MOP sponge. The MOP sponge consisting of entangled tubular MOP fibers was synthesized via a one-pot Sonogashira-Hagihara coupling reaction. Sulfur groups were introduced to the MOP fibers by the thiol-yne reaction with a dithiol. Ag nanoparticles were immobilized in the MOP sponge by the in situ reduction of Ag^{+} ions. The MOP sponge-Ag heterogeneous catalyst showed good catalytic ability and recyclability in the reduction reaction of 4-NP. The MOP sponge with hierarchical porosity and the ease of functionalization is a promising supporting material for noble metal catalysts. In particular, the compressible and monolithic properties of the MOP sponge make it an excellent candidate for use in a flow reactor and future research will be focused in this direction.

IV-5. References

1. Gao, F.; Goodman, D. W. *Annu. Rev. Phys. Chem.* **2012**, *63*, 265–286.

2. Lu, J.; Toy, P. H. *Chem. Rev.* **2009**, *109*, 815–838.
3. Dawson, R.; Cooper, A. I.; Adams, D. J. *Prog. Polym. Sci.* **2012**, *37*, 530–563.
4. Xu, Y.; Jin, S.; Xu, H.; Nagai A.; Jiang, D. *Chem. Soc. Rev.*, **2013**, *42*, 8012–8031.
5. Li, G.; Zhang, B.; Yan, J.; Wang, Z. *J. Mater. Chem. A* **2014**, *2*, 18881–18888.
6. Li, G.; Zhang, B.; Wang, Z. *Macromolecules* **2016**, *49*, 2575–2581.
7. Chen, L.; Honsho, Y.; Seki, S.; Jiang, D. *J. Am. Chem. Soc.* **2010**, *132*, 6742–6748.
8. Jiang, J. X.; Su, F.; Trewin, A.; Wood, C. D.; Campbell, N. L.; Niu, H.; Dickinson, C.; Ganin, A. Y.; Rosseinsky, M. J.; Khimyak, Y. Z.; Cooper, A. I. *Angew. Chemie. Int. Ed.* **2007**, *46*, 8574–8578.
9. Schmidt, J.; Werner, M.; Thomas, A. *Macromolecules* **2009**, *42*, 4426–4429.
10. Lim, H.; Chang, J. Y. *Macromolecules*, **2010**, *43*, 6943–6945.
11. Lim, H.; Cha, M. C.; Chang, J. Y. *Polym. Chem.* **2012**, *3*, 868–870.
12. Yang, Z.; Zhang, H.; Yu, B.; Zhao, Y.; Ma, Z.; Ji, G.; Han, B.; Liu, Z. *Chem. Commun.* **2015**, *51*, 11576–11579.
13. Liu, J.; Tobin, J. M.; Xu, Z.; Vilela, F. *Polym. Chem.* **2015**, *6*, 7251-

7255.

14. Zhuang, X.; Gehrig, D.; Forler, N.; Liang, H.; Wagner, M.; Hansen, M. R.; Laquai, F.; Zhang, F.; Feng, X. *Adv. Mater.* **2015**, *27*, 3789–3796.
15. Cha, M. C.; Lim, Y.; Chang, J. Y. *J. Polym. Sci. Part A Polym. Chem.* **2015**, *59*, 2336–2342.
16. Zhang, L.; Wang, K.; Qian, X.; Liu, H.; Shi, Z. *ACS Appl. Mater. Interfaces* **2013**, *5*, 2761–2766.
17. Lim, Y.; Cha, M. C.; Chang, J. Y. *Sci. Rep.* **2015**, *5*, 15957.
18. Ruan, C.; Ai, K.; Li, X.; Lu, L. *Angew. Chemie. Int. Ed.* **2014**, *53*, 5556–5560.
19. Chen, X.; Weibel, J. A.; Garimella, S. V. *Ind. Eng. Chem. Res.* **2016**, *55*, 3596−3602.
20. Ye, K.; Zhang, D.; Zhang, H.; Cheng, K.; Wang, G.; Cao, D. *Electrochim. Acta* **2015**, *178*, 270–279.
21. García-Moreno, F. *Materials* **2016**, *9*, 20–24.
22. Chun, J.; Park, J. H.; Kim, J.; Lee, S. M.; Kim, H. J.; Son, S. U. *Chem. Mater.* **2012**, *24*, 3458-3463.
23. Kang, N.; Park, J. H.; Choi, J.; Jin, J.; Chun, J.; Jung, I. G.; Jeong, J.; Park, J. G.; Lee, S. M.; Kim, H. J.; Son, S. U. *Angew. Chem. Int. Ed.* **2012**, *51*, 6626-6630.

24. Chen, Y.; Sun, H.; Yang, R.; Wang, T.; Pei, C.; Xiang, Z.; Zhu, Z.; Liang, W.; Li, A.; Deng, W. *J. Mater. Chem. A* **2015**, *3*, 87-91.

25. Urakami, H.; Zhang, K.; Vilela, F. *Chem. Commun.* **2013**, *49*, 2353–2355.

26. Islamoglu, T.; Kim, T.; Kahveci, Z.; El-Kadri, O. M.; El-Kaderi, H. M. *J. Phys. Chem. C* **2016**, *120*, 2592–2599.

27. Ghasimi, S.; Landfester, K.; Zhang, K. A. I. *ChemCatChem* **2016**, *8*, 694–698.

28. Kiskan, B.; Weber, J. *ACS Macro Lett.* **2012**, *1*, 37–40.

29. Cliffel, D. E.; Zamborini, F. P.; Gross, S. M.; Murray, R. W. *Langmuir* **2000**, *16*, 9699–9702.

30. Cargnello, M.; Wieder, N. L.; Canton, P.; Montini, T.; Giambastiani, G.; Benedetti, A.; Gorte, R. J.; Fornasiero, P. A. *Chem. Mater.* **2011**, *23*, 3961–3969.

31. Pötzsch, R.; Komber, H.; Stahl, B. C.; Hawker, C. J.; Voit, B. I. *Macromol. Rapid Commun.* **2013**, *34*, 1772–1778.

32. Wei, Q.; Pötzsch, R.; Komber, H.; Pospiech, D.; Voit, B. *Polymer* **2014**, *55*, 5600–5607.

33. Lee, H.; Kim, H.; Choi, T. J.; Park, H. W.; Chang, J. Y. *Chem. Commun.* **2015**, *51*, 9805-9808.

34. Pan, Y.; Liu, Z.; Wang, W.; Peng, C.; Shi, K.; Ji, X. *J. Mater. Chem. A* **2016**, *4*, 2537-2549.

35. Zhao, J.; Ren, W.; Cheng, H. M. *J. Mater. Chem.* **2012**, *22*, 20197–20202.

36. Lin, K. Y. A.; Chang, H. A. *J. Mater. Chem. A* **2015**, *3*, 20060-20064.

37. Chi, Y.; Tu, J.; Wang, M.; Li, X.; Zhao, Z. J. *Colloid Interface Sci.* **2014**, *423*, 54–59.

38. Liang, K.; Li, X.; Kang, S. Z.; Qin, L.; Li, G.; Mu, J. *Carbon* **2014**, *80*, 716–724.

39. Mnasri, N.; Charnay, C.; De Ménorval, L. C.; Moussaoui, Y.; Elaloui, E.; Zajac, J. *Microporous Mesoporous Mater.* **2014**, *196*, 305–313.

40. Xiao, W.; Zhang, Y.; Liu, B. *ACS Appl. Mater. Interfaces* **2015**, *7*, 6041–6046.

41. Qian, H.; He, Q.; Zheng, J.; Li, S.; Zhang, S. *Polymer* **2014**, *55*, 550–555.

42. Wu, K.; Guo, J.; Wang, C. *Angew. Chemie. Int. Ed.* **2016**, *55*, 1–6.

Chapter V.

A Hierarchically Porous Polyimide Composite Prepared by One-Step Condensation Reaction inside a Sponge for Heterogeneous Catalysis

V-1. Introduction

Heterogeneous catalysts are widely used in the chemical industry owing to their advantages of easy separation from products, recyclability, and applicability to continuous flow processes.[1,2] Supported catalysts are an important class of heterogeneous catalysts, where catalytically active species are immobilized in porous supporting materials such as activated carbons, mesoporous silica, and metal oxides.[3-6] A large surface area and high porosity of the supporting materials can improve the dispersion of active species and the accessibility of reactants to the active sites.[3,4] In recent years, a number of heterogeneous catalysts based on microporous organic polymers (MOPs) have been reported.[7-11] MOPs have an advantage as a supporting material compared with inorganic supports such that specific functionality can be easily introduced to them for favorable interactions with active species.

Sponges are a class of materials which have highly interconnected open cellular structures. They have good mechanical stability, compressibility, and processability. However, because sponges have large pores and low surface areas, they are mainly used for removing liquids by absorption. Recently functional sponge composites have attracted considerable interest, which are prepared by the incorporation of functional constituents into the sponges. Functional sponge composites have various applications such as absorption,[12]

filtration,[13] fuel cells,[14] flow reactors,[15,16] pollutant removal,[17-20] and catalysis.[21] In this study, we prepared a hierarchically porous polyimide composite by in situ polymerization inside a synthetic sponge. Aromatic polyimides are an important class of high performance polymers due to their rigid structures and thermal stability.[22-25] We synthesized a microporous aromatic polyimide with metal coordination sites using an aminophenanthroline as a functional comonomer. When the reaction was carried out inside a melamine sponge, a hierarchically porous and compressible composite was obtained. A heterogeneous catalyst was prepared by coordination with Pd(II) ions, and its catalytic activity was evaluated in a Suzuki coupling reaction.

V-2. Experimental

Materials. Isoquinoline (97 %), palladium chloride ($PdCl_2$) (59 wt% Pd), phenylboronic acid (98%, containing anhydride), and 4'-bromoacetophenone (98 %) were purchased from ACROS Organics. 1,3,5-Tris(4-aminophenyl) benzene (> 93 %), pyromellitic dianhydride (98 %), and 4-bromoanisole (97 %) were obtained from Tokyo Chemical Industry. 5-Amino-1,10-phenanthroline (97 %) was purchased from Sigma-Aldrich. Potassium carbonate (K_2CO_3) was obtained from Daejung Chemicals & Metals Co. The melamine sponge was obtained from BASF Co. Other solvents were purchased from Junsei Chemical. All materials were used without further purification.

Preparation of the Melamine Sponge/Microporous Polyimide Composite (MS/MPI-Phen) and the Microporous Polyimide (MPI-Phen). 1,3,5-Tris(4-aminophenyl)benzene (84.3 mg, 0.24 mmol) and 5-amino-1,10-phenanthroline (35.1 mg, 0.18 mmol) were dissolved in a mixture of N-methyl-2-pyrrolidone (4 mL), mesitylene (4 mL), and isoquinoline (0.4 mL) in a 20 mL vial. After dissolving pyromellitic dianhydride (98.2 mg, 0.45 mmol) in the solution, a piece of melamine sponge (25.0 mg) was immersed and then heated at 100 ^{o}C for 1 h and 160 ^{o}C for 24 h without stirring. The resulting composite (MS/MPI-Phen) was washed with acetone and THF and dried under vacuum at

room temperature.

The microporous polyimide containing phenanthroline groups (MPI-Phen) was prepared in the same manner except that a piece of melamine sponge was absent in the polymerization solution.

Immobilization of Pd(II) Ions onto MS/MPI-Phen (MS/MPI-Phen-Pd). $PdCl_2$ (100 mg) was dissolved in acetonitrile (30 mL) at 90 ^oC. MS/MPI-Phen (150 mg) was immersed in the solution and heated at 90 ^oC for 24 h with stirring. The resultant composite was washed with acetonitrile and dried under vacuum at 70 ^oC.

Suzuki Coupling Reaction Catalyzed by MS/MPI-Phen-Pd. A small piece of MS/MPI-Phen-Pd (20.0 mg) and K_2CO_3 (276 mg, 2 mmol) were added to a solution of a bromophenyl derivative (1 mmol) and phenylboronic acid (146 mg, 1.2 mmol) in 8 mL of an aprotic solvent. The mixture was stirred at 95 ^oC for 24 h. After the removal of the catalyst, the reaction mixture was concentrated by evaporation. The product yield was determined by analyzing the reaction mixture with ^1H NMR spectroscopy. The catalyst was reused after washing with H_2O, ethanol, and THF and drying.

Instrumental Characterization. FT-IR spectra were measured by a Nicolet 6700 FT-IR Spectrometer. ^{1}H NMR spectra were recorded on a Bruker Avance-300 spectrometer (300 MHz). Solid-state ^{13}C NMR spectrum was recorded on a Bruker Avance II spectrometer (125 MHz). Powder X-ray diffraction (PXRD) patterns were observed using a New D8 Advance (Cu K_{α} radiation, $\lambda = 1.54$ Å). X-ray photoelectron spectroscopy (XPS) was measured by a KRATOA AXIS-His spectrometer equipped with a Mg K_a X-ray source. Scanning electron microscopy (SEM) images were obtained by a Carl Zeiss SUPRA 55VP. Energy-dispersive X-ray spectroscopy (EDS) elemental map was obtained using an Oxford instrument X-MaxN detector and analyzed with an Aztec Energy EDS analyzer. Thermogravimetric analyses (TGA) were performed on a TA modulated TGA2050 with a heating rate of 10 °C/min under nitrogen. N_2 adsorption-desorption isotherms were investigated by a Belsorp-Max (BEL Japan, Inc.) apparatus. The compression tests were performed by an Instron 5543 universal testing machine. A cylindrical sponge having a diameter of 16 mm and height of 15 mm was used for the measurement. The strain-stress curves were measured at a strain rate of 3 mm min-1. Inductively coupled plasma mass spectrometry (ICP-MS) was measured using a Varian 820-MS to calculate a weight percentage of Pd(II) in the sponge. Pd ions were dissolved in strong nitric acid before measurement.

V-3. Results and Discussion

V-3-1. Synthesis and Characterizations of MPI-Phen

A microporous polyimide containing phenanthroline groups as metal binding sites (MPI-Phen) was synthesized as insoluble powders by the condensation reaction of 1,3,5-tris(4-aminophenyl)benzene, pyromellitic dianhydride, and 5-amino-1,10-phenanthroline (Scheme V-1). The molar ratio of the triamine, dianhydride, and phenanthroline was controlled to be 8:15:6, where the number of amine groups was equivalent to the number of anhydride groups. When the ratio of the phenanthroline increased, the BET surface area of the polymer sharply decreased.

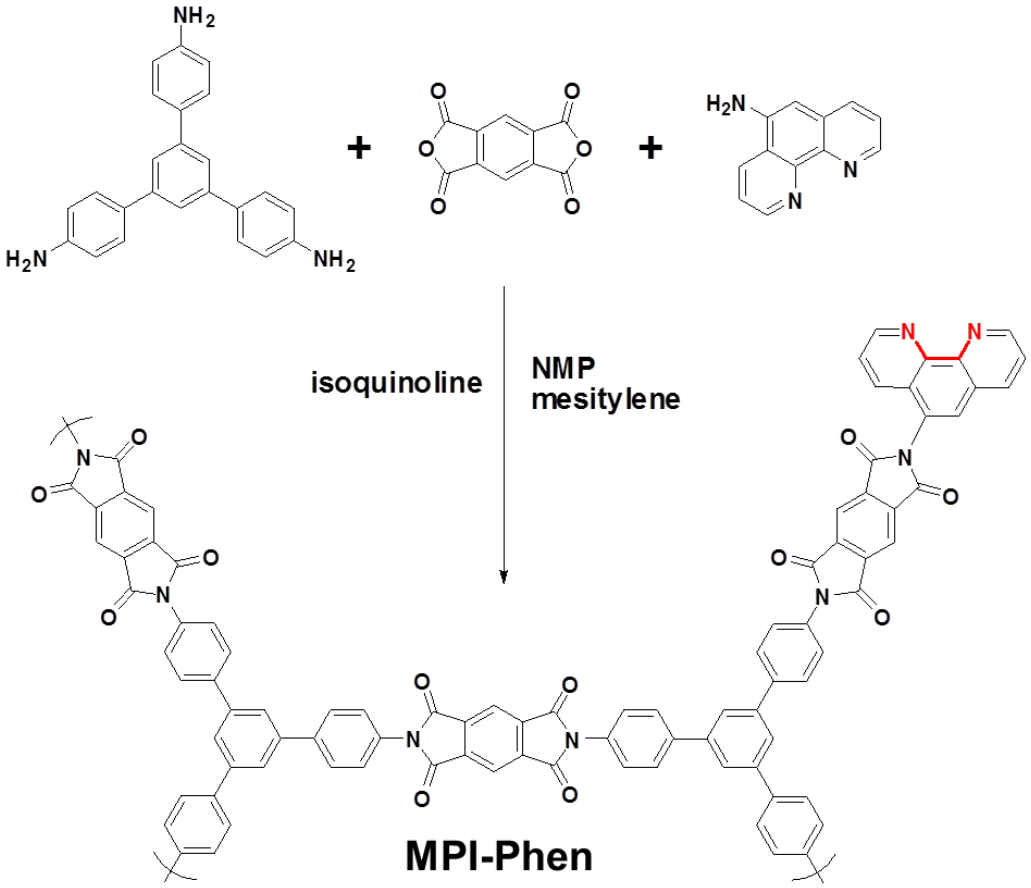

Scheme V-1. Synthesis of a microporous polyimide containing phenanthroline groups (MPI-Phen).

The molecular structure of MPI-Phen was characterized by FT-IR and solid ^{13}C NMR spectroscopy. The FT-IR spectrum of MPI-Phen showed the symmetric and asymmetric vibration peaks of the imide carbonyl groups at 1721 and 1780 cm^{-1}, respectively (Figure V-1a). The C-N-C stretching peak of

the heterocyclic imide rings appeared at 1356 cm^{-1}.[24,26] In the ^{13}C NMR spectrum, the aromatic carbon peaks were observed between 110 and 145 ppm (Figure V-1b) and the peak at 164 ppm was assigned to the imide carbonyl groups. The small peak at 174 ppm was assigned to the amide carbonyl groups of uncyclized amic acid moieties.[26] The PXRD pattern of MPI-Phen did not show any discernible peaks, implying the amorphous nature of the polymer (Figure V-1c). The presence of the phenanthroline group in MPI-Phen was confirmed by XPS analysis. Two deconvoluted peaks centered at 400.5 eV and 398.7 eV were observed in the XPS spectrum for the N1s region (Figure V-1d), which corresponded to the nitrogens of imide[27] and phenanthroline groups, respectively.[28,29] From these results, we concluded that the microporous polyimide containing phenanthroline groups were successfully prepared.

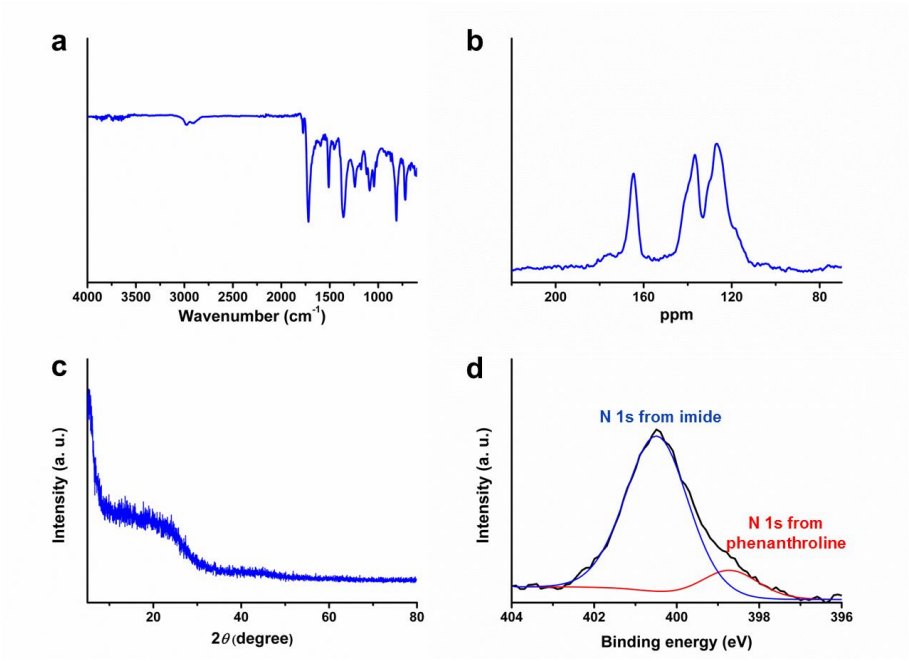

Figure V-1. (a) FT-IR spectra, (b) Solid state ^{13}C CP/MAS NMR spectra and (c) PXRD pattern of MPI-Phen. (d) High-resolution XPS spectra of N 1s from MPI-Phen.

The nitrogen adsorption-desorption analysis of MPI-Phen showed both type I and type IV physisorption isotherms, indicating the presence of micro- and mesopores (Figure V-2).[30] The BET surface area of MPI-Phen was 723 m^2g^{-1}, which was comparable with those of previously reported microporous polyimides.[31,32]

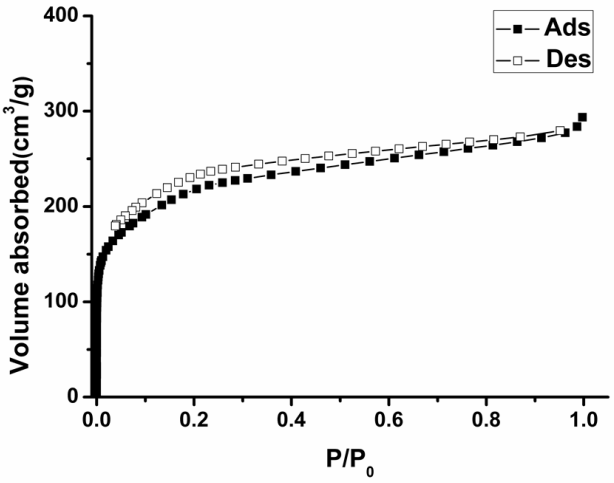

Figure V-2. N_2 adsorption-desorption isotherms of MPI-Phen.

V-3-2. Fabrication and Characterizations of MS/MPI-phen

A polyimide composite with hierarchical porosity (MS/MPI-Phen) was prepared by in situ polymerization inside a melamine sponge. The polymerization was carried out in the same manner as described for MPI-Phen except that a cylindrical melamine sponge was immersed in the polymerization solution. The color of the melamine sponge turned from white to yellowish brown, indicating the incorporation of MPI-Phen (Figure V-3). MS/MPI-Phen could be cut into any shape with a knife.

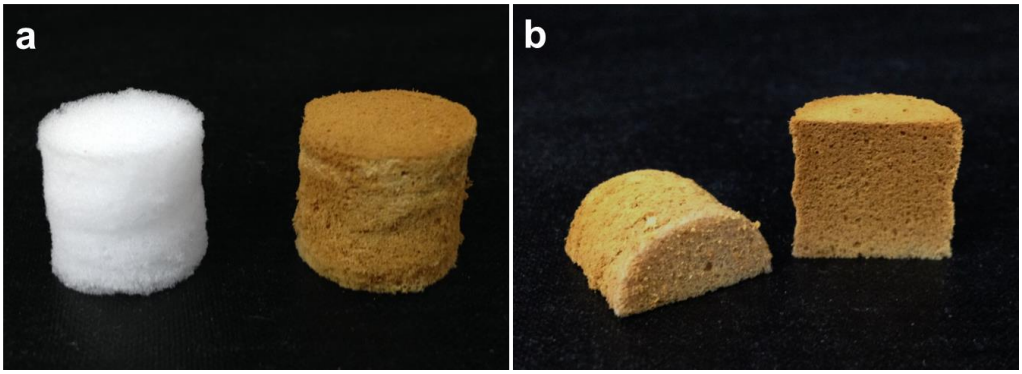

Figure V-3. (a) Images of the melamine sponge (left) and MS/MPI-Phen (right). (b) Cross-sections of MS/MPI-Phen.

Figure V-4 shows the SEM images of the melamine sponge, MPI-Phen, and MS/MPI-Phen. The melamine sponge had smooth skeletons. MPI-Phen showed a particulate morphology. When the polymerization was carried out in the melamine sponge, MPI-Phen heavily coated the sponge skeletons. The coating was stable under sonication for 1 h in THF. The high coating stability was attributed to the strong interactions between the melamine sponge and the MPI-Phen. The melamine sponge contained many secondary amine groups,[12] which could form hydrogen bonds with imide or amic acid moieties of MPI-Phen.[20,33-35] MS/MPI-Phen had a hierarchically porous structure composed of macropores between the skeletons and meso- and micropores of the MPI-Phen coating.[18,21]

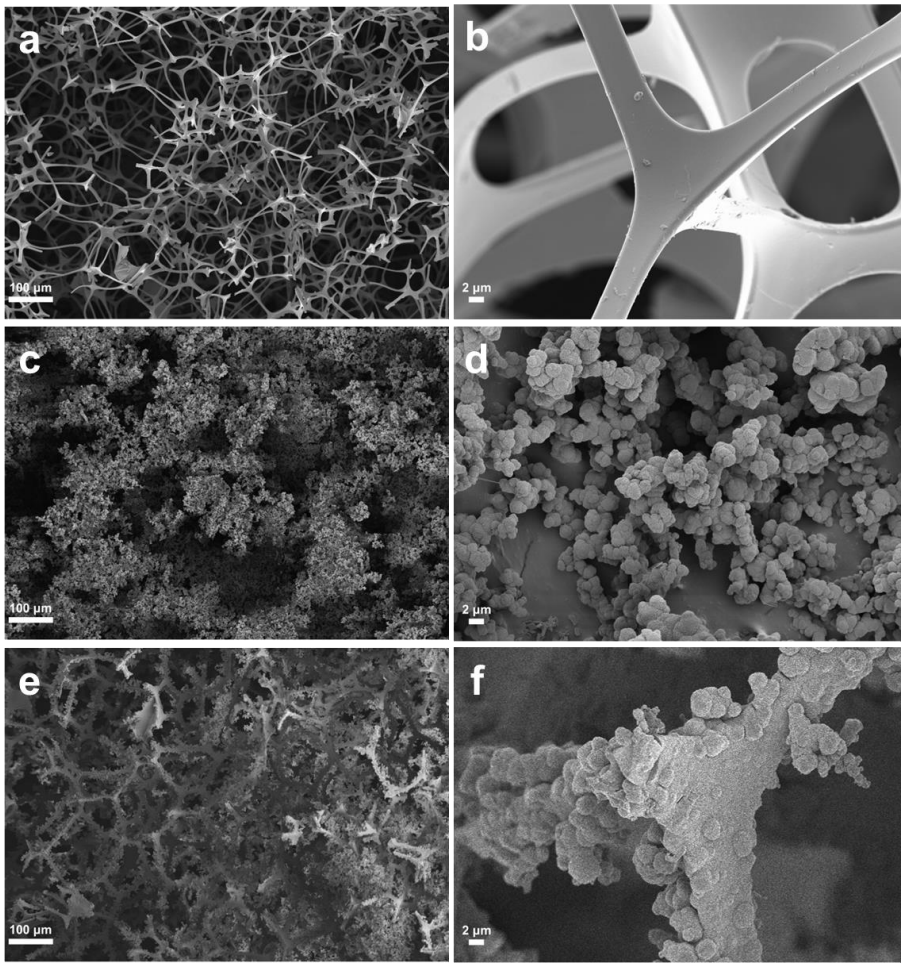

Figure V-4. SEM images of (a), (b) the melamine sponge, (c), (d) MPI-Phen and (e), (f) MS/MPI-Phen.

The TGA measurement showed that MPI-Phen had high thermal stability up to 500 ^{o}C, while the melamine sponge started to degrade at 300 oC (Figure V-5). The char yields of the melamine sponge, MPI-Phen, and MS/MPI-Phen at 800 ^{o}C were 5.9, 63.1 and 45.9 wt%, respectively. The amount of MPI-Phen (M)

incorporated into MS/MPI-Phen was estimated to be 69.9 wt% using the following equation[20]:

$$C_1 \times (M / 100) + C_2 \times (100 - M) / 100 = C_3 \quad (1)$$

where C_1, C_2 and C_3 are the char yields of MPI-Phen, the melamine sponge, and MS/MPI-Phen, respectively.

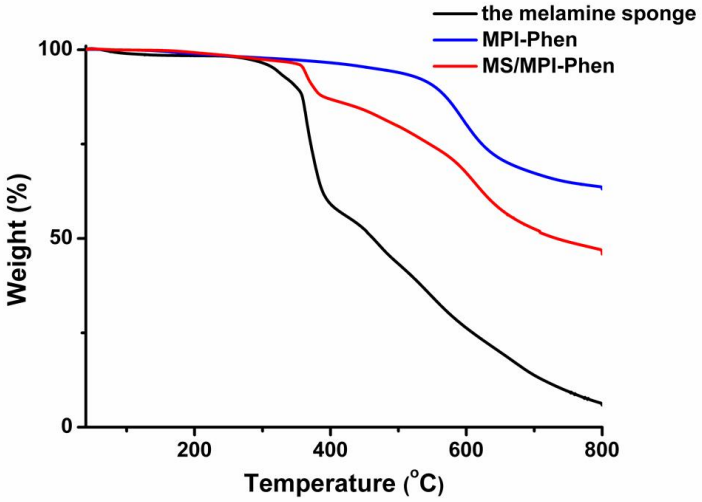

Figure V-5. TGA thermograms of the melamine sponge, MPI-Phen and MS/MPI-Phen.

Figure V-6a shows nitrogen adsorption-desorption isotherms of the melamine sponge, MPI-Phen, MS/MPI-Phen measured at 77 K. The BET

surface area of MS/MPI-Phen was 524 m^2g^{-1}, which was slightly smaller than that of MPI-Phen (723 m^2g^{-1}) due to the presence of the melamine sponge containing no micro- and mesopores. The non-local density functional theory (NLDFT) pore size distribution curve of MS/MPI-Phen was similar to that of MPI-Phen (Figure V-6b), suggesting that the growth of MPI-Phen on the sponge skeleton did not significantly affect its pore structure.[20]

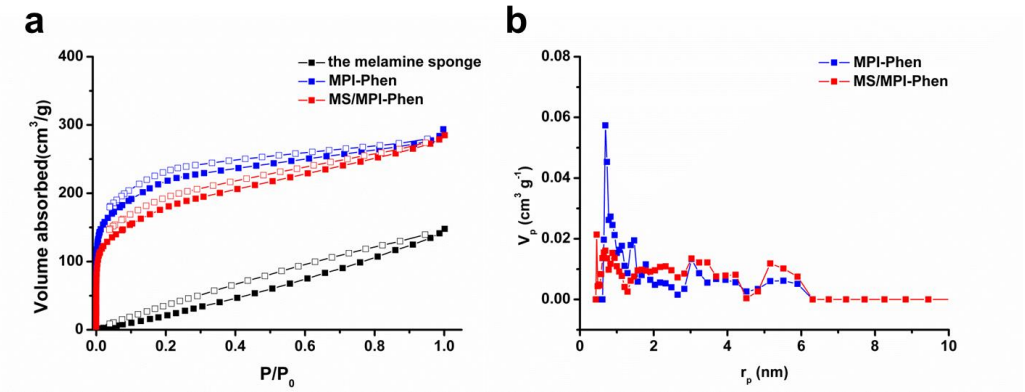

Figure V-6. (a) N_2 adsorption-desorption isotherms of the melamine sponge, MPI-Phen, and MS/MPI-Phen. (b) NLDFT pore size distributions of MPI-Phen and MS/MPI-Phen.

MS/MPI-Phen was reversibly compressible (Figure V-7a). It showed the higher compressive strength than the melamine sponge (Figure V-7b, c), indicating the reinforcement by the microporous polymer.[17]

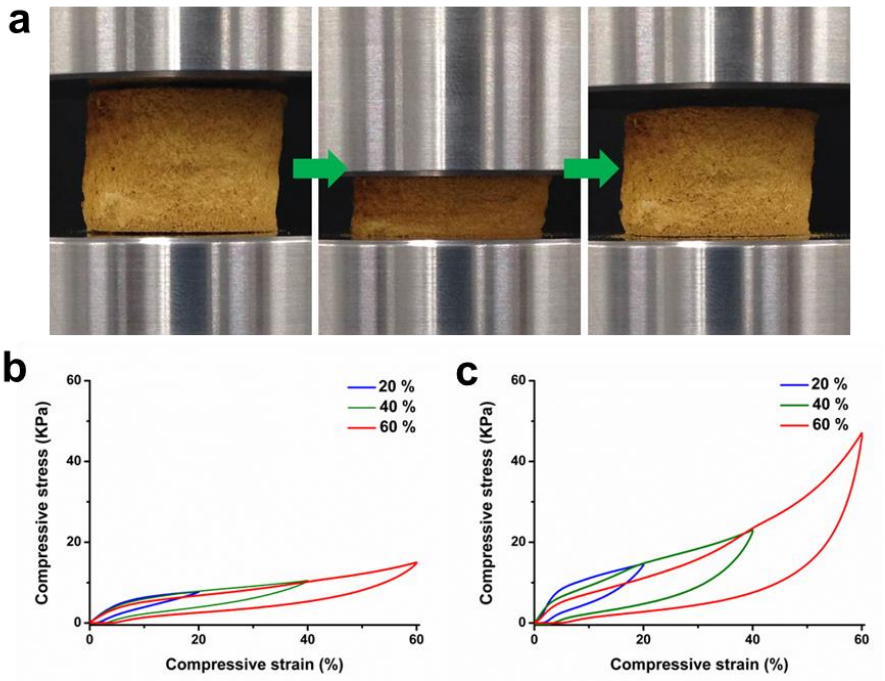

Figure V-7. (a) Images of MS/MPI-Phen under compressed and released conditions (strain = 60 %). Compressive stress-strain curves (maximum strain = 20, 40 and 60 %) of (b) the melamine sponge and (c) MS/MPI-Phen.

V-3-3. Pd^{2+} Chelating into MS/MPI-Phen for Suzuki Coupling Reaction

1,10-Phenanthroline is widely used to coordinate various metal ions like copper, iron, platinum, palladium and lanthanides.[36-40] In this study, Pd(II) ions were coordinated with the phenanthroline groups of MS/MPI-Phen for

heterogeneous catalysis.[41] Figure V-8 shows the SEM, EDS, and XPS analysis results. The microstructural morphology of the sponge was not changed after the coordination (Figure V-8a). The EDS analysis revealed that Pd species were uniformly distributed over the MPI-Phen coating (Figure V-8b, c). The concentration of Pd(II) ions in MS/MPI-Phen-Pd was 0.53 wt% when measured by ICP-MS. In the XPS analysis (Figure V-8d), MS/MPI-Phen-Pd exhibited two peaks centered at 343.4 eV and 338.1 eV, which came from Pd $3d_{3/2}$ and Pd $3d_{5/2}$ of $PdCl_2$, respectively.[42]

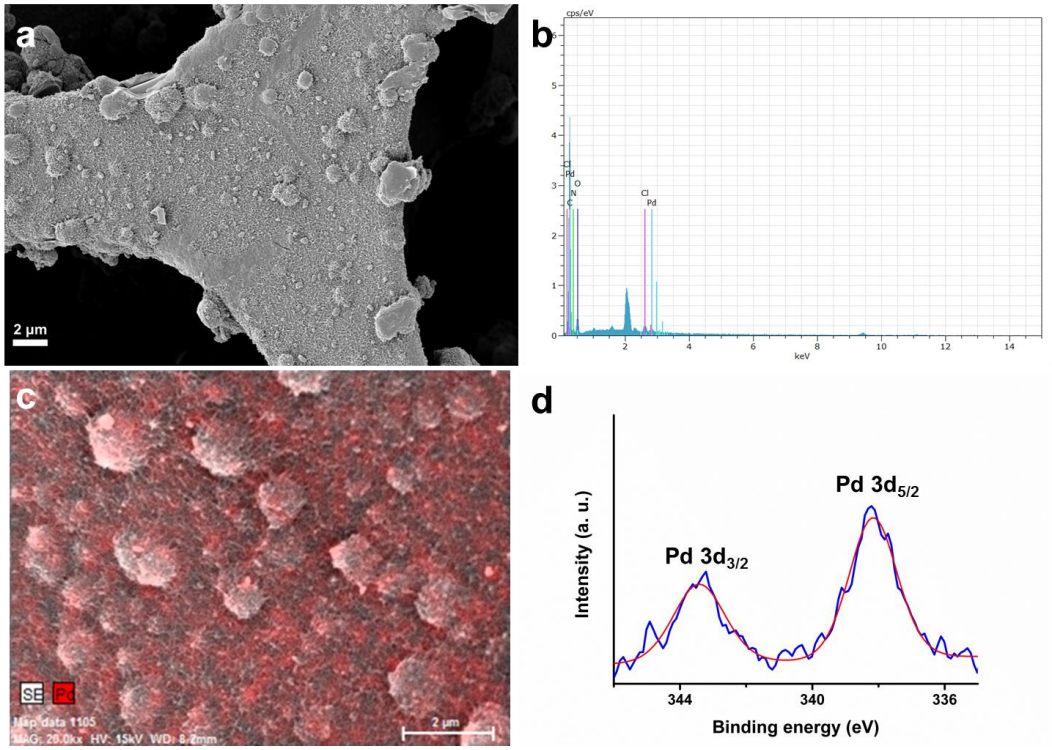

Figure V-8. (a) SEM image and (b) EDS spectrum of MS/MPI-Phen-Pd. (c) EDS mapping of Pd atom for MS/MPI-Phen-Pd. (d) High-resolution XPS spectrum of Pd 3d region of MS/MPI-Phen-Pd.

The catalytic activity of MS/MPI-Phen-Pd was evaluated for Suzuki coupling reactions between bromobenzene and phenylboronic acid (Scheme V-2). The reaction was carried out in an aprotic solvent such as toluene, 4-dioxane, THF, and DMF using K_2CO_3 as a base. As shown in Table V-1, the product yield was the highest in toluene. When the reaction was performed in an aqueous base, the degradation of the imide structure was found.[43-45] Suzuki

coupling reactions with bromobenzene derivatives such as using 4-bromoanisole and 4-bromoacetophene were also catalyzed by MS/MPI-Phen-Pd. After the 24 h reaction, the conversion yields of 4-bromoanisole and 4-bromoacetophene were 79.0 % and 70.1 %, respectively.

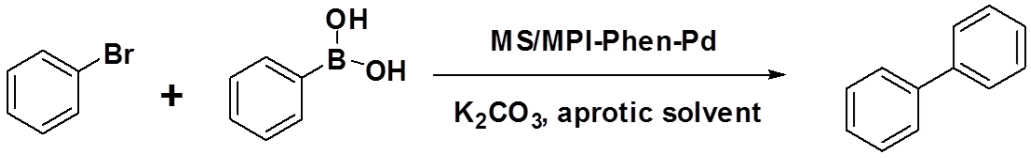

Scheme V-2. Suzuki coupling reaction between bromobenzene and phenylboronic acid in the presence of MS/MPI-Phen-Pd

Table V-1. Suzuki coupling reaction results in different reaction solvents.

Entry	Solvent	Yield (%)[a]
1[b]	Toluene	83.3
2[b]	1,4-Dioxane	54.1
3[c]	THF	27.6
4[b]	DMF	No reaction

Reaction conditions: 1.0 mmol of bromobenzene, 1.2 mmol of phenylboronic acid, 2.0 mmol of K_2CO_3, 20 mg of MS/MPI-Phen-Pd, 8 mL of a solvent, 24 h.

[a]The yield was determined by the ^{1}H NMR analysis of the reaction mixture.

[b]Reaction under 95 ^{o}C.

[c]Reaction under reflux.

After the reaction, MS/MPI-Phen-Pd was easily removed from the reaction mixture because of its monolithic character. The recycling test showed that the yields of the coupling reaction between bromobenzene and phenylboronic acid decreased to 75.9 % and 56.6 % in the 2nd and 3rd cycles, respectively. This result could be due to the leaching of Pd(II) ions during recycling.

V-4. Conclusions

In conclusion, we demonstrated the fabrication of a microporous polyimide composite by the one-step condensation reaction of an aromatic triamine and an aromatic dianhydride in a melamine sponge. Metal binding groups could be incorporated into the composite using a functional aromatic amine as a comonomer. The composite had a core-shell structure, where the sponge skeleton was coated with the microporous polyimide due to strong interactions between the melamine and the polyimide units. As a result, the composite possessed a hierarchically porous structure, composed of micro- and mesopores in the polyimide coating and macropores formed by the sponge skeletons. The composite could be prepared in any size and shape. These characteristics together with the metal binding functionality made the composite a promising support material for heterogeneous catalysis. The approach presented here would be expanded to prepare compressible and hierarchically porous monoliths having various functionalities.

V-5. References

1. Copéret, C.; Comas-Vives, A.; Conley, M. P.; Estes, D. P.; Fedorov, A.;

Mougel, V.; Nagae, H.; Núñez-Zarur, F.; Zhizhko, P. A. *Chem. Rev.* **2016**, *116*, 323-421.

2. Cole-Hamilton, D. J. *Science*, **2003**, *299*, 1702-1706.
3. Puthiaraj, P.; Lee, Y. R.; Zhang, S.; Ahn, W. S. *J. Mater. Chem. A* **2016**, *4*, 16288-16311.
4. Price, P. M.; Clark, J. H.; Macquarrie, D. J. *J. Chem. Soc., Dalton Trans.*, **2000**, 101-110.
5. Zheng, H.; Gao, F.; Valtchev, V. *J. Mater. Chem. A*, **2016**, *4*, 16756-16770.
6. Dhakshinamoorthy, A.; Garcia, H. *Chem. Soc. Rev.* **2012**, *41*, 5262-5284.
7. Shultz, A. M.; Farha, O. K.; Hupp, J. T.; Nguyen, S. T. *Chem. Sci.* **2011**, *2*, 686-689.
8. Jiang, J. X.; Wang, C.; Laybourn, A.; Hasell, T.; Clowes, R.; Khimyak, Y. Z; Xiao, J.; Higgins, S. J.; Adams, D. J.; Cooper, A. I. *Angew. Chem. Int. Ed.* **2011**, *50*, 1072-1075.
9. Liang, Q.; Liu, J.; Wei, Y.; Zhao, Z.; MacLachlan, M. J. *Chem. Commun.* **2013**, *49*, 8928-8930.
10. Zhao, X.; Yan, N. *RSC Adv.* **2015**, *5*, 69955-69961.
11. Liras, M.; Iglesias, M.; Sánchez, F. *Macromolecules*, **2016**, *49*, 1666-

1673.

12. Pham, V. H.; Dickerson, J. H. *ACS Appl. Mater. Interfaces* **2014**, *6*, 14181-14188.
13. Li, H.; Gui, X.; Zhang, L.; Wang, S.; Ji, C.; Wei, J.; Wang, K.; Zhu, H.; Wu, D.; Cao, A. *Chem. Commun.* **2010**, *46*, 7966-7968.
14. Zhao, L.; Sui, X.-L.; Li, J.-L.; Zhang, J.-J.; Zhang, L.-M.; Wang, Z.-B. *ACS Appl. Mater. Interfaces* **2016**, *8*, 16026-16034.
15. Uemura, S.; Suzuki, S.; Abe, K.; Kubota, K.; Yamaguchi, T.; Ohashi, A.; Takemura, Y.; Harada, H. *Bioresor. Technol.* **2010**, *101*, 5180-5185.
16. Yu, X. -F.; Mao, L. -B.; Ge, J.; Yu, Z. -L.; Liu, J. -W.; Yu, S. -H. *Sci. Bull.* **2016**, *61*, 700-705.
17. Yang, Y.; Shi, E.; Li, P.; Wu, D.; Wu, S.; Shang, Y.; Xu, W.; Cao, A.; Yuan, Q. *Nanoscale* **2014**, *6*, 3585-3592.
18. Andrew Lin, K. -Y. ; Chang, H. A *J. Mater. Chem. A* **2015**, *3*, 20060-20064.
19. Lim, Y.; Cha, M. C.; Chang, J. Y. *Sci. Rep.* **2015**, *5*, 15957.
20. Kim, J. G.; Choi, T. J.; Chang, J. Y. *Chem. Eng. J.* **2016**, *306*, 242-250.
21. Wu, K.; Guo, J.; Wang, C. *Angew. Chem. Int. Ed.* **2016**, *55*, 1-6.
22. Li, G.; Wang, Z. *Macromolecules* **2013**, *46*, 3058-3066.
23. Yang, Y.; Zhang, Q.; Zhanga, Z.; Zhang, S. *J. Mater. Chem. A* **2013**, *1*,

10368-10374.

24. Kim, Y. J.; Jeong, Y. G. *Macromol. Res.* **2015**, *23*, 1144-1151.
25. Tundidor-Camba, A.; Terraza, C. A.; Tagle, L. H.; Coll, D.; Ortiz, P.; Pérez, G.; Jessop, I. A. *Macromol. Res.* **2017**, doi: 10.1007/s13233-017-5029-5.
26. Wang, Z.; Zhang, B.; Yu, H.; Li, G.; Bao, Y. *Soft Matter* **2011**, *7*, 5723-5730.
27. Ektessabi, A. M.; Hakamata, S. *Thin Solid Films* **2000**, *377-378*, 621-625.
28. Stańczyk, K.; Dziembaj, R.; Piwowarska, Z.; Witkowski, S. *Carbon* **1995**, *33*, 1383-1392.
29. Ren, C.; Li, H.; Li, R.; Xu, S.; Wei, D.; Kang, W.; Wang, L.; Jia, L.; Yanga, B.; Liu, J. *RSC Adv.* **2016**, *6*, 33302-33307.
30. Sing, K. S. W.; Everett, D. H.; Haul, R. A. W.; Moscou, L,; Pierotti, R. A.; Rouquérol, J.; Siemieniewska, T. *Pure Appl. Chem.* **1985**, *57*, 603-619.
31. Wang, Z.; Zhang, B.; Yu, H.; Li, G.; Bao, Y. *Soft Matter* **2011**, *7*, 5723-5730.
32. Liebl, M. R.; Senker, *J. Chem. Mater.* **2013**, *25*, 970-980
33. Liu, Z.; Miao, Y. E.; Liu, M.; Ding, Q.; Tjiu, W. W.; Cui, X.; Liu, T. *J.*

Colloid Interf. Sci. **2014**, *424*, 49-55.

34. Benson, R. S.; Lee, M. W.; Grummitt, D. W. *Nanostruct. Mater.* **1995**, *6*, 83-91.
35. Liu, X.; Gao, G.; Dong, L.; Gu, G. Y, Y. *Polym. Adv. Technol.* **2009**, *20*, 362-366.
36. Accorsi, G.; Listorti, A.; Yoosaf, K.; Armaroli, N. *Chem. Soc. Rev.* **2009**, *38*, 1690-1700.
37. Pallenberg, A. J.; Koenig, K. S.; Barnhart, D. M. *Inorg. Chem.* **1995**, *34*, 2833-2840.
38. Dai, Z.; Chen, F.; Sun, Q.; Ji, Y.; Wang, L.; Meng, X.; Xiao, F. S. *Chinese J. Chem.* **2016**, *37*, 54-60.
39. Chen, Z.; Li, X.; Jin, X.; Shi, L.; Liu, M.; Sun, Z.; Lu, J. *Macromol. Res.* **2015**, *23*, 830-837.
40. Ren, J.; Gu, J.; Tao, L.; Zhang, G.; Yang, W. *Macromol. Res.* **2016**, *24*, 502-507.
41. Magano, J.; Dunetz, J. R. *Chem. Rev.* **2011**, *111*, 2177-2250.
42. Kumar, G.; Blackburn, J. R.; Albridge, R. G.; Moddeman, W. E.; Jones, M. M. *Inorg. Chem.* **1972**, *11*, 296-300.
43. Stoffel, N. C.; Hsieh, M.; Chandra, S.; Kramer, E. J. *Chem. Mater.* **1996**, *8*, 1035-1041.

44. Stephans, L. E.; Myles, A.; Thomas, R. R. *Langmuir* **2000**, *16*, 4706-4710.

45. Lee, J.; Chang, J. Y. *Chem. Comm.* **2016**, *52*, 10419-10422.

국문요약

마이크로기공성 고분자는 넓은 표면적, 저밀도, 마이크로기공성, 물리화학적 안정성 등 우수한 특성을 갖고 있다. 또한 반응물질의 선택이나 후처리를 통해 마이크로기공성 고분자 내부에 다양한 기능성을 부여할 수 있어 여러 분야에서의 활용이 가능하다. 하지만 대부분의 마이크로기공성 고분자는 가교결합 구조를 갖는 불용성의 가루형태로 얻어져 나쁜 가공성을 갖는다. 본 연구에서는 물리적 형태의 조절이 가능한 기능성 마이크로기공성 고분자들을 제조하고 이들을 불균질 촉매의 제조와 염료의 흡착에 활용하였다.

첫 번째로 고분자의 합성과정에 전기방사 나노섬유를 분산시키어 나노섬유로 강화된 마이크로기공성 고분자 스펀지를 제조했다. 2,5-Dibromoaniline과 1,3,5-triethynylbenzene의 소노가시라-하기하라 반응을 나노섬유 (PVASi)의 존재 하에 진행하여 코어셸 나노섬유 구조를 갖는 압축성 스펀지 (PVASi@TEDB-NH_2) 를 얻었다. 고분자는 나노섬유의 표면에서 균일하게 자랐으며 이는 고분자가 갖고 있는 아민기가 PVASi 표면의 하이드록실기와 수소결합을 형성하기 때문이다. PVASi@TEDB-NH_2는 30.4 mg cm^{-3}의 평균 밀도와 447 m^2g^{-1}의

BET 표면적을 보였다. 복합체 스펀지는 물 속의 유기 염료를 제거하는데 사용하였으며 반복적인 압축을 통하여 염료의 빠른 제거가 가능하였다.

두 번째로, hypercrosslinked 고분자 (HCP)를 기반으로 한 마이크로기공성 촉매막을 제조하였다. 아민 작용기가 도입된 폴리아크릴로나이트릴 (APAN) 나노섬유 막을 기질로 이용하고 1,1'-bi-2-naphthol의 프리델-크래프츠 반응을 수행하여 HCP를 기반으로 한 나노섬유 막을 합성하였다. HCP는 APAN 나노섬유의 표면에서 균일하게 자라나 막에 위계적 기공성을 부여하였다. HCP를 기반으로 한 마이크로기공성 막은 우수한 기계적 강도와 마이크로기공성을 가졌고 BET 표면적은 375 m^2g^{-1}이었다. 막 내부에서 팔라듐 나노입자를 성장시키어 HCP를 기반으로 한 마이크로기공성 촉매막 (APAN-HCP-Pd) 을 제조한 후 촉매특성을 4-nitrophenol의 환원반응을 통해 평가하였다.

세 번째로, 마이크로기공성 나노튜브 스펀지를 이용한 압축성 단일체 촉매를 제조하였다. 1,4-Diiodotetrafluorobenzene과 1,3,5-triethynylbenzene의 소노가시라-하기하라 반응을 톨루엔과 트리에틸아민(2:1, 부피비율)의 혼합용액에서 교반하지 않고 진행하여

마이크로기공성 단일체 스펀지를 합성하였다. 이 스펀지는 수백 나노미터의 직경을 가진 튜브구조의 고분자 섬유들이 서로 엉키어 있는 흥미로운 마이크로구조를 보였으며 512 m^2g^{-1}의 BET 표면적과 위계적 기공성을 가졌다. 싸이올-인 반응을 통하여 마이크로기공성 스펀지에 황 작용기를 도입하였다. 개질된 마이크로기공성 스펀지의 BET 표면적은 반응 전보다 13% 높아졌는데 이는 싸이올-인 반응에 의한 마이크로기공의 증가 때문이다. 황으로 개질된 마이크로기공성 스펀지 내부에 은 나노입자를 성장시키어 마이크로기공성 스펀지-은 불균질 촉매 (S-MOP-Ag) 를 제조한 후 4-nitrophenol 수용액의 환원 반응에 이용하여 촉매 특성을 조사하였다. S-MOP-Ag의 반복적인 압축을 수행하면 촉매 반응 속도가 크게 증가하였다. S-MOP-Ag는 단일체적 성질 때문에 반응 용액으로부터 회수가 용이하였고 세척과 건조 후에 재사용이 가능하였다.

마지막으로, 금속이온을 고정할 수 있는 작용기를 가진 압축성 폴리이미드 스펀지를 멜라민 스펀지 내부에서의 중합 반응을 통해 제조하였다. 1,3,5-Tris(4-aminophenyl)benzene과 pyromellitic dianhydride를 마이크로기공성 고분자의 주 단량체로 사용하고, 5-amino-1,10-phenanthroline을 기능성 단량체로 사용하였다. Phenanthroline 작용기를

지닌 폴리이미드 (MPI-Phen) 은 불용성의 가루형태로 얻어졌으나 멜라민 스펀지의 존재 하에서 중합할 경우, 스펀지의 골격 위에서 코팅 층을 형성하였다. 멜라민 스펀지-마이크로기공성 폴리이미드 복합체 (MS/MPI-Phen) 는 스펀지 내부의 매크로기공과 폴리이미드의 메조, 마이크로기공들이 공존하는 위계적 기공성을 보였다. 복합체 스펀지는 멜라민 스펀지에 비해 높은 압축 강도를 보였는데 이는 마이크로기공성 고분자의 보강효과 때문이다. MPI-Phen과 MS/MPI-Phen의 BET 표면적은 각각 723 m^2g^{-1}와 524 m^2g^{-1}이었다. 불균질 촉매로의 활용을 위해 MS/MPI-Phen 내부에 존재하는 phenanthroline 작용기에 팔라듐 이온을 고정화 시킨 후 bromobenzene과 phenylboronic acid를 이용한 스즈키 커플링 반응에 이용하여 촉매활성을 측정하였다.

주요어: 마이크로기공성 고분자, 전기방사, 스펀지, 막, 불균질 촉매, 염료 흡착.

학번: 2011-20631

List of Publications and Patents

(1) **Jong Gil Kim**, Tae Jin Choi and Ji Young Chang. "Homogenized electrospun nanofiber reinforced microporous polymer sponge", *Chem. Eng. J.* **2016**, *306*, 242-250.

(2) **Jong Gil Kim**, Jeongmin Lee, Jieun Lee, Seong In Jo and Ji Young Chang. "A hierarchically porous polyimide composite prepared by one-step condensation reaction inside a sponge for heterogeneous catalysis", *Macromol. Res.* **2017**, *25*, 629-634.

(3) **Jong Gil Kim**, Min Chul Cha, Tae Jin Choi and Ji Young Chang. "Preparation of a sulfur-functionalized microporous polymer sponge and *in situ* growth of silver nanoparticles: a compressible monolithic catalyst", *Submitted.*

(4) Jieun Lee, **Jong Gil Kim** and Ji Young Chang. "Fabrication of a microporous organic polymer membrane and its application for membrane catalysis", *Submitted.*

List of Presentations

(1) 2012년 4월, 춘계 한국고분자학회, “Preparation of Phosphazene-Based Porous Nanofibers by Electrospinning”

(2) 2012년 10월, 추계 한국고분자학회, “Preparation of Microporous Electrospun Nanofibers from Multifunctional Cyclotriphosphazene”

(3) 2013년 10월, 추계 한국고분자학회, “Preparation and Characterization of Microporous Polycyanurates”

(4) 2014년 4월, 춘계 한국고분자학회, “Synthesis of Cyclotriphosphazene-Based Microporous Polymer via Imine Condensation”

(5) 2016년 4월, 춘계 한국고분자학회, “Fabrication of a Conjugated Microporous Polymer-Nanofiber Composite Membrane”

(6) 2017년 4월, 춘계 한국고분자학회, “Preparation of a Microporous Organic Polymer-Nanofiber Composite Membrane for Oil-Water Separation”